Hydroforming of lightweight alloys using MagnetoRheological Fluids (MRF)

Politecnico di Bari

Department of Mechanics, Mathematics and Management

MECHANICAL AND MANAGEMENT ENGINEERING
Ph.D. Program

SSD: ING-IND/16– MANUFACTURING TECHNOLOGY AND SYSTEMS

Final Dissertation

Hydroforming of lightweight alloys using MagnetoRheological Fluids (MRF)

---

by

Angela Cusanno

Supervisors:

Prof. Gianfranco Palumbo

Eng. Alessandro Montalto

Eng. Evgenia Yakushina

Coordinator of Ph.D. Program:

Prof. Giuseppe Pompeo Demelio

Course n°34, 21/11/2018-20/01/2022

Politecnico di Bari

Department of Mechanics, Mathematics and Management

MECHANICAL AND MANAGEMENT ENGINEERING

Ph.D. Program

SSD: ING-IND/16– MANUFACTURING TECHNOLOGY AND SYSTEMS

Final Dissertation

Hydroforming of lightweight alloys using MagnetoRheological Fluids (MRF)

---

by

Angela Cusanno

Referees:

Prof. M.B. Silva

Prof. M.L. Garcia-Romeu

Supervisors:

Prof. Gianfranco Palumbo

Eng. Alessandro Montalto

Eng. Evgenia Yakushina.

Coordinator of Ph.D Program

Prof. Giuseppe Pompeo Demelio

Course n°34, 21/11/2018-20/01/2022

Contents

Introduction

Nowadays the development of lightweight components is a great challenge in several sectors: in the automotive and aerospace fields, the possibility of replacing conventional metallic materials with lighter alloys helps to reduce energy consumptions. Moreover, in the biomedical field, the use of prostheses made of materials characterized by density, fracture toughness, elastic modulus and compressive yield strength similar to those of the human bone helps to minimize the risk of stress shielding effects. In this scenario, aluminum and magnesium alloys are good candidates for the transport and biomedical sectors, respectively. In fact, aluminum (Al) alloys can provide good mechanical properties combined with a low density, exhibit a good resistance to corrosion, some grades have good resistance to UV light (thus ensuring optimal performance over a long period of time), are suitable for recycling and the combination of their different properties allows these alloys to be shaped through any process of industrial transformation providing complete freedom of design. As for magnesium (Mg) alloys as biodegradable metals in the biomedical sector, interest for these alloys has strongly grown over the last decades mainly because of their biocompatibility, biodegradability, good machinability, high weight-to-strength ratio and mechanical properties similar to those of the human bones. However, the attractiveness of those alloys is partially counterbalanced by the poor formability at room temperature. Furthermore, Mg alloys exhibit a very fast corrosion rate in body fluids due to the release of Hydrogen, which must be taken into account when considering the material for the prostheses manufacturing. Thus, innovative and flexible technological solutions are needed to manufacture complex-shaped components made of the aforementioned materials. Local heat treatments, for example, are used to overcome poor formability, allowing to tailor the distribution of material properties according to the requirements of the forming process. On the other hand, when the degradation rate becomes a key aspect, several studies report that coating Mg alloys with specific materials, such as polymers, can be considered a promising solution to control the corrosion behaviour of the substrate. Those technological solutions must be combined with suitable forming process. Current innovative and flexible forming processes such as Superplastic Forming (SPF), Incremental Forming (IF) and Hydroforming (HF) enable obtaining complex parts with high accuracy. In the recent years, MagnetoRheological Pressure Forming (MRPF) has gained interest because the thickness and the strain distribution on the formed part can be affected by properly changing the properties of the forming medium. In the case of MRPF, the forming medium is a Magnetorheological Fluid (MRF). This kind of fluids is included in the so called “smart materials”: they are based on a suspension of magnetically

responsive particles in a liquid carrier, whose rheological behaviour (e.g., its viscosity) can be changed quickly and reversibly if subjected to a magnetic field. Currently, MRFs are widely used in the automotive field for brakes and clutches, in the biomedical field for prostheses and for these applications there are already available constitutive models which are able to describe the field-dependent MRF characteristics (shear stress vs. shear rate). On the contrary, when used for sheet metal forming applications, there are still few studies in the literature about the most effective way to characterise their rheological behavior, which is fundamental for the Finite Element (FE) based design and simulation of the process.

In this scenario, the aims of the present thesis are (i) expanding the manufacturing of lightweight complex-shaped components to alternative processes, such as the hydroforming process using MRF; (ii) to put the basis for an effective methodology to characterize the rheological behavior of an MRF for sheet metal forming applications, (iii) to design an experimental MRF-based equipment to characterize MRFs and (iv) to study possible applications of MRFs to manufacturing processes.

Figure 1 summarizes the organization of the thesis.

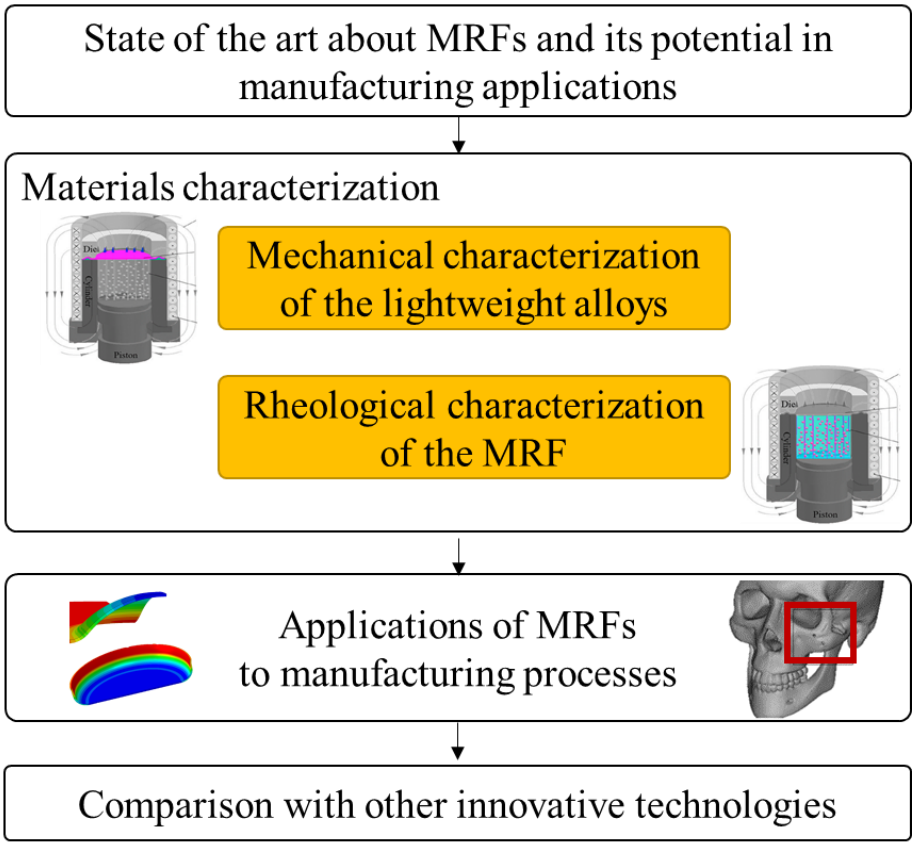

Figure 1 Organization of the thesis

The thesis starts with an overview of the MRFs. In particular, rheological and magnetic properties of the commercial MRFs, their operational modes, the commonly used models describing the MRFs behavior and their current applications are given. An overview of the current lightweight materials used in the transportation and biomedical sector is provided, as well as the present and possible future strategies adopted to manufacture complex-shaped parts starting from them. Then, materials and methodologies adopted are presented. As for the lightweight materials investigated, a Mg alloy (AZ31B) and an Al alloy (AA5754, both in the H32 and in the H111 temper) were chosen for their attractiveness in the biomedical and transport sector, respectively. Their mechanical properties were investigated by means of conventional methods (tensile and bulge tests) and non-conventional ones (Single Point Incremental Forming tests). Additionally, a new methodology for the mechanical characterization of lightweight alloys based on the combination of laser heat treatments and bulge tests was proposed. As for the rheological characterization of the MRF, two different approaches were evaluated: the first one based on the combination of extrusion tests and FE simulation, the second one on an inverse analysis approach using data from bulge tests performed on the Al alloy adopting the MRF as forming medium. Then, possible applications of MRFs to manufacturing processes are proposed. In particular, the feasibility of manufacturing a magnesium AZ31B biomedical component by means of MRF Hydroforming and a deep drawn part using MRF is evaluated. As for the biomedical component, bulge tests on Mg alloy at room temperature using MRF as forming medium were conducted, in order to obtain the maximum strains that can be reached with the MRF Hydroforming technology at room temperature. Those strains were then compared with the ones reached by two magnesium cheeckbone prostheses formed by means of other innovative manufacturing processes (SPF and SPIF). As for the deep drawn part using MRF, Hydromechanical Deep Drawing (HMDD) process using MRF on the magnesium alloy were conducted to evaluate the advantages of adopting MRFs in the HMDD process. Finally, the main outcomes of the thesis are resumed, and a list of in progress and published scientific works written during the PhD is provided.

1. Magnetorheological Fluids (MRF)

Materials whose properties vary considerably in the presence of an external stimulus are known as smart materials. Various smart materials have been identified so far. The most important of them are magnetic suspensions (magnetorheological fluids and ferrofluids), electrorheological fluids, piezoelectric materials and shape-memory alloys [1]. Magnetic suspensions are complex fluids whose rheological characteristics change significantly in the presence of a magnetic field. These materials are divided into two groups: ferrofluids which are a stable colloidal mixture of ferromagnetic nano-particles and magnetorheological fluids (MRFs) which are suspensions of magnetizable microparticles dispersed in a carrier fluid.

In the following subsections, an overview of the rheological and magnetic properties of the commercial MRFs, their operational modes, the commonly used models describing the MRFs behavior and their current applications are given.

1.1 Basic principles of the MRFs

Magnetorheological Fluids (MRFs) are a suspension consisting of fine polarizable particles of ferromagnetic material dispersed in a base liquid that can be mineral oil, synthetic oil, silicone oil, water, or glycolysis [1]. The particles are between 0.5 and 10 μm in diameter [2]. Additives are generally added to the solutions to promote particle dispersion and anti-sedimentation stability, as well as improve lubrication and prevent thermal decomposition. Commonly used additives for MRFs include oleic acid, polyethylene glycol, polysorbate, silica gel, coupling agent, magnesium and lithium silicate, and other non-ionic additives [2], [3].

MRFs belong to the family of smart fluids, since they are able to vary their rheological behavior as the intensity of an applied external magnetic field changes. This property allows such fluids to change from a liquid state, when no magnetic field is applied, to a semi-solid state (when a magnetic field is applied) and to vary their viscosity rapidly and in a reversible way [4]. In fact, in absence of a magnetic field (B=0), particles are dispersed randomly (Figure 1.1a), while when an external magnetic field is applied (B>0), the magnetizable particles are subjected to a dipole moment which, as shown in Figure 1.1b, tends to align them to form chains parallel to the magnetic flux lines, i.e. from the south (S) to north (N) pole of the magnet [5].

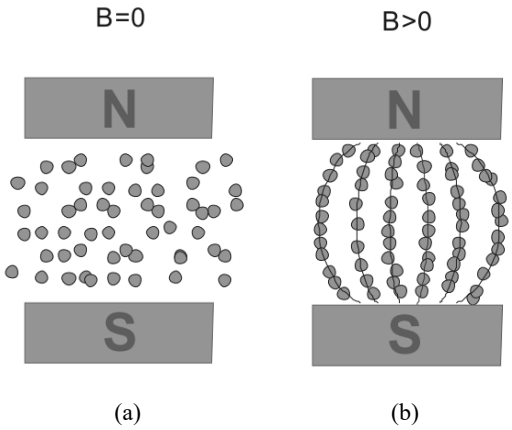

Figure 1.1 MRF's particles behaviour (a) in absence of magnetic field and (b) when a magnetic field is applied [5]

As the magnetic flux increases, these chains aggregate together to form real columns which are responsible for the macroscopic increase in viscous characteristics because they reduce the mobility of the fluid [6]. The result of this behavior is the possibility, using an electromagnet, to adjust the forces transmitted by the fluids. Although initially it seemed that this controlled material would remain a laboratory curiosity, interest in these fluids has grown due to the evolution of control electronics [7]. In fact, MRFs have achieved commercial success and several types are now available on the market that differ in both the type of base fluid and the percentage of solid particles dispersed.

1.1.1 Rheological properties of the MRFs

The rheological properties of MRFs strongly depend on the properties of the base fluid, the concentration and density of the particles suspended in it, their size and shape, the additives added, but also on the applied magnetic field, temperature and secondary factors such as the operating conditions [8], [7]. Some major properties and their typical value of MRF are summarized in Table 1.1.

Property	Typical value
Initial viscosity	0.2–0.3 [Pa s] (at 25 °C)
Density	3–4 [g/cm^3]
Magnetic field strength	150–250 [kA/m]
Maximum yield stress	50–100 [kPa]
Reaction time	Few milliseconds
Typical supply voltage and current intensity	2–25 [V], 1–2 [A]
Work temperature	−50 to 150 [°C]

Table 1.1 Major characteristics of MRFs [7]

Studying the interdependence between all these factors is complex, thus it is essential to establish the methodologies necessary to optimise the performance of these fluids while still considering the different and specific applications in which they will be used.

The field-dependent MRF characteristics are described by rheological models or so-called constitutive models, which relate the shear stress to the shear rate of MRFs. In a first approximation, the behavior of fluids can be described with the Bingham model (Eq. 1) which is the simplest model typical of viscoplastic materials, which assumes that the fluid does not move until the shear stress has exceeded the controlled yield shear stress [9]:

$$\begin{aligned} \dot{\gamma} &= 0 && |\tau| < |\tau_y(H)| \\ \tau &= \tau_0(H) sign(\dot{\gamma}) + \eta\dot{\gamma} && |\tau| \geq |\tau_y(H)| \end{aligned} \tag{1}$$

In which $\dot{\gamma}$ is the shear rate, τ is the shear stress, τ_0 is the yield shear stress, which is a function of the magnetic field applied to the fluid, below which the material behaves as a solid and above which viscous creep begins, H is the magnetic field strength and η is the boundary or plastic viscosity, which is independent of the applied magnetic field. Figure 1.2 shows the typical relationship between shear stress and shear rate for a Bingham fluid and compares this with a Newtonian fluid.

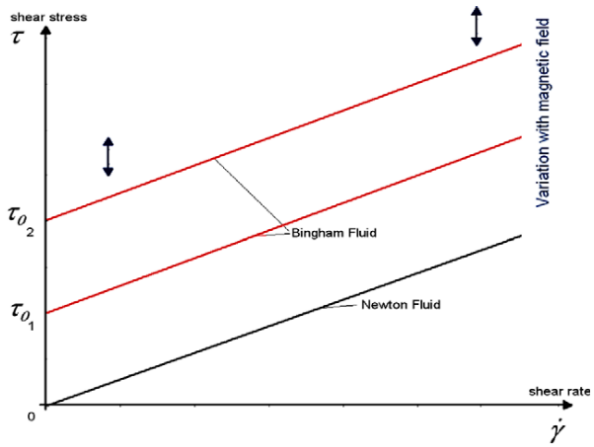

Figure 1.2 Shear stress vs. Shear rate of Bingham and Newtonian model of an MRF [10]

According to Bingham's model, at zero shear rate there is some resistance to flow. In this condition, the maximum stress, which can be applied without causing continuous movement, is the yield shear stress τ_0 and it is a function of the magnetic field strength. In absence of a magnetic field, τ_0 is almost zero, and the MRF can be considered as a common Newtonian fluid (Eq. 2):

$$\tau = \eta\dot{\gamma} \tag{2}$$

1.1.2 Magnetic properties of the MRFs

Knowing the magnetic properties of a MRF is essential for the design of devices operating with such fluids because they are part of the magnetic circuit. Usually they are described by the magnetic induction curve, which represents the magnetic flux density as a function of the magnetic field strength. In particular, the magnetic flux density, B [T], is given by Eq. 3:

$$B = \mu_r * \mu_0 * H \quad (3)$$

$$\mu_0 = 4\pi * 10^{-7} \left[\frac{Wb}{A}\right] \quad (4)$$

In which μ_r is the specific relative magnetic permeability of the medium excited by the magnetic field, μ_0 is the vacuum magnetic permeability (given by Eq. 4 and measured in Wb/A, where 1 [Wb]= 1 [kg·m^2·s^{-2}·A^{-1}]) and H [A/m] is the magnetic field strenght, which is independent of the medium properties. As an example, the magnetic induction curves of two MRFs are shown in Figure 1.3.

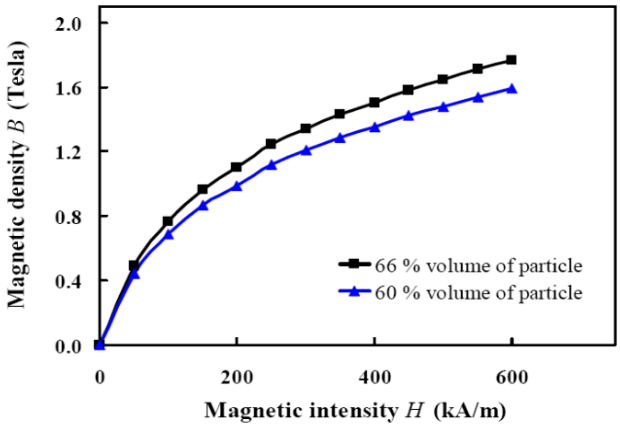

Figure 1.3 Magnetic induction curves of MRF for two different values of iron volume per cent [11]

It can be noticed that for the same value of magnetic field strength H, the magnetic flux density B is higher when increasing the percentage of solid particles. In addition, it can be seen that the relative permeability of the MRFs is not a constant value and varies nonlinearly with the magnetic field strength, H.

1.2 Operational modes

The MRFs have three basic operational modes: flow mode (Figure 1.4a), direct shear mode (Figure 1.4b), and squeeze mode (Figure 1.4c). The difference among these modes depends on the level of stress induced in the fluid as well as on how the fluid flows; also mixed operations are possible.

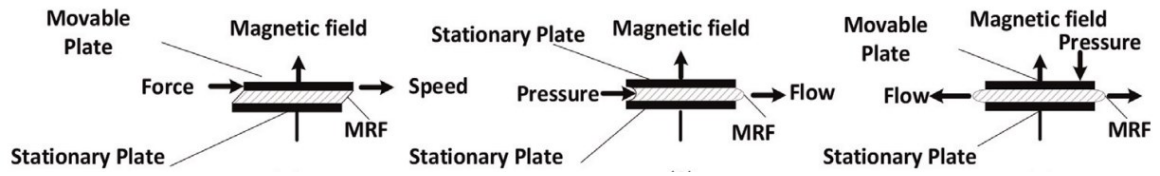

(a) (b) (c)

Figure 1.4 Basic operational modes of MRFs [12]: (a) direct shear mode, (b) flow mode and (c) squeeze mode

1.2.1 Flow mode

The flow mode (Figure 1.4a) is applied to the MRF placed between two fixed surfaces and in the presence of a pressure drop ΔP perpendicular to magnetic field lines that forces fluid movement in the meatus. The pressure drop ΔP developed in a flow mode based device is obtained from the sum of a viscous component, ΔPμ and a yield shear stress related component, ΔPτ. This pressure drop can be approximated by the Eq. 5 [1]:

$$\Delta P = \Delta P\mu + \Delta P\tau(H) = \frac{12\,\mu\,Q\,L}{g^3\,w} + \frac{c\,\tau_y(H)\,L}{g} \tag{5}$$

In which L, g and w are the length, distance, and width of the flow channel between fixed poles, Q is the volumetric flow rate,η is the viscosity without an applied magnetic field, τ_y is the yield shear stress developed in response to an applied field H. The parameter c depends on the flow velocity profile and has a value between 2 and 3 depending on the ratio ΔPτ/ΔPμ. This solution is used to construct dampers, vibration absorbers, and shock absorbers.

1.2.2 Shear mode

The shear mode (Figure 1.4b) is applied when the fluid is located between two walls that have a relative motion generated by a tangential force F applied to one of the two surfaces; also in this case the magnetic field is orthogonal to the direction of motion. It is possible to obtain the tangential force for the shear mode, which consists of a viscous term and one related to the tangential stress (Eq. 6) [13]:

$$F = F_\mu + F_\tau(H) = \frac{\mu\,v\,A}{g} + \tau y(H)A \tag{6}$$

where v is the relative velocity of the two surfaces and A the area given by the product of L and w, i.e., length and width of the flow channel. This configuration is typically chosen for the realization of brakes and clutches.

1.2.3 Squeeze mode

The squeeze mode (Figure 1.4c) is applied when the two surfaces have a relative motion which is orthogonal to the fluid, and the magnetic field is parallel to the relative displacement of the surfaces. The total amount of force in the squeeze mode is estimated by Eq. 7 [12]:

$$F_s = \frac{-\pi R^4}{4}\left(\frac{6\mu\dot{h}}{h^3} + \frac{3\rho\ddot{h}}{5h} - \frac{15\rho\dot{h}^2}{14h^2}\right) \tag{7}$$

where R, h, μ, $\dot{h}$, $\ddot{h}$ and ρ are the plate radius, the distance between the two parallel plates, the viscosity of the MRF, the gap acceleration, the gap speed and the density of the MRF, respectively. The configuration is often used in vibration dampers for which very small displacements and high forces are required.

1.3 MRF applications

Since the 1990s, MRFs have gained a growing interest due to the possibility of exploit their advantages in the operation of various devices. Nowadays, there are many applications of these materials in various engineering fields. The following subsections give an overview of the different MR devices that have been manufactured in flow and shear mode for several fields (automotive, biomedical, civil).

1.3.1 MRF applications in the automotive field

In the automotive field, the MRFs applications are essentially of two types: brakes, seat suspensions and vehicle suspension system.

A braking system consists of a rotor, which is the moving element, and a stator, which is the fixed element. The stator in the technology that adopts MRFs acts both as a frame for the brake and as a housing for the MRF. The uniqueness of these devices is that they can be considered as brakes because they consist of two mechanical parts such as the stator, for the input of the movement, and the rotor, for the output, but they also allow to modulate the braking torque similarly to the action carried out by a clutch, because between them is the MRF that allows the coupling with various degrees of intensity [14].

Figure 1.5a shows an example of a MR brake while Figure 1.5b shows its geometry.

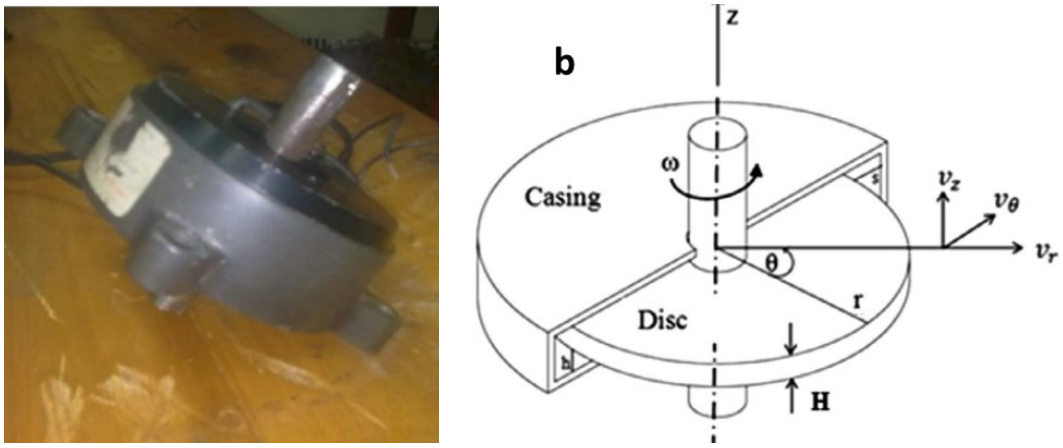

(a) (b)

Figure 1.5 (a) Brake Lord RD-2087 [14] (b) Scheme of the brake [14]

Another application in the automotive field is represented by cars' primary suspensions, which are of great importance because they must support the weight of the car, isolate the vehicle from road bumps and maintain traction between the tire and the road surface. Unlike traditional hydraulic systems, Magnetorheological Controlled Suspension (SCM) provides instantaneous damping control with respect to road conditions and driver demands (Figure 1.6). This is due to the ability of the shock absorber fluid to vary its dynamic characteristics by reacting to an electronically controlled magnetic field.

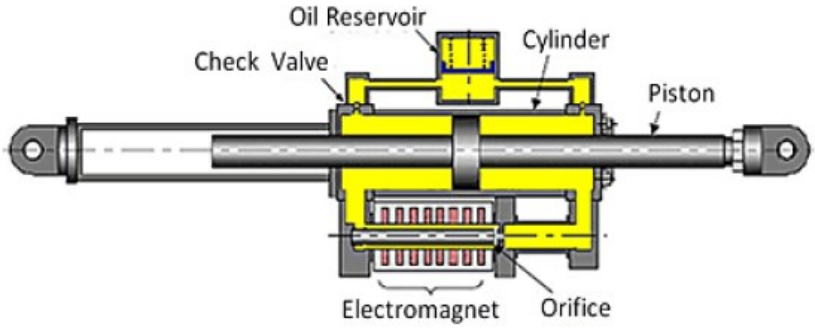

Figure 1.6 MR Car suspensions[15]

The first car equipped with MR suspension was marketed in 2002, since then many manufacturers have used this technology (Cadillac, Chevrolet, Audi, Ferrari and other U.S. companies) [15]. The semi-active vibration control system, instead, was first used in truck seats in 1998. A semi-active vibration control system, shown in Figure 1.7, includes the MRF damper, microprocessor, sensor, current driver, and auxiliary cables. Currently, more than 5000 semi-active MRF-based vibration control systems are used in heavy trucks in America. Such systems are also satisfactory from the point of view of recorded failures, which are almost zero [15][16].

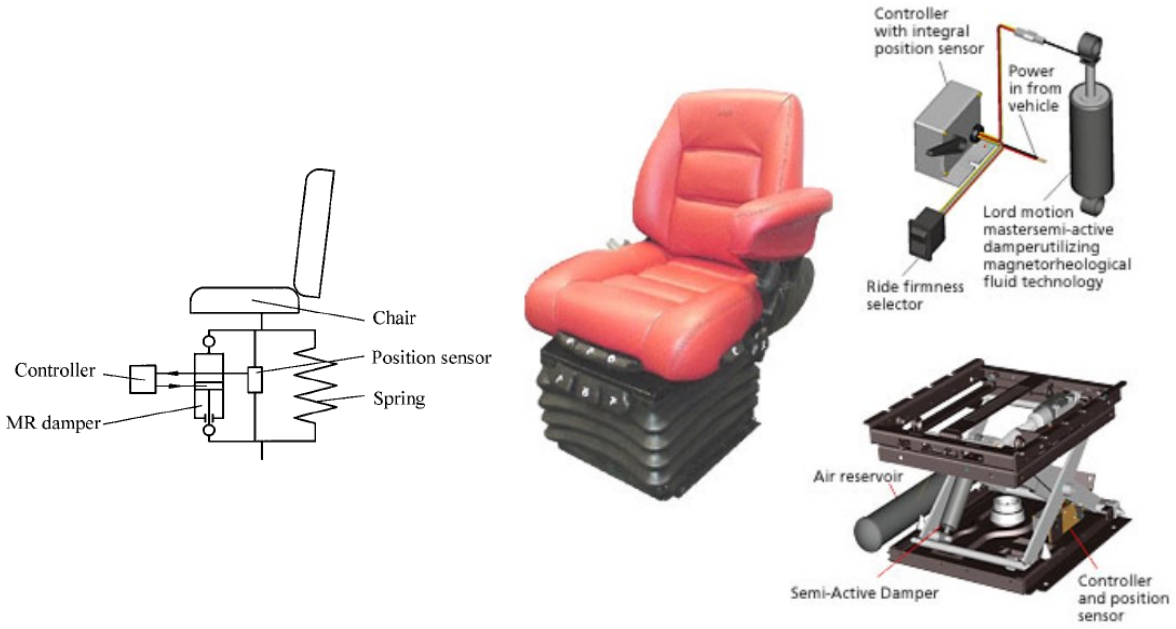

(a) (b)

Figure 1.7 (a) Scheme of a seat equipped with a semi-active suspension with MRF damper [15]; (b) Suspended seats MR dampers system

1.3.2 MRF applications in the civil structures

For civil engineering, MRFs are used in buildings and devices designed for damping seismic vibrations. This kind of device is mainly oriented to reduce the impact of induced vibrations on structures, such as seismic actions. One example concerns the absorption of wind-induced vibrations in cable-stayed bridges, such as the flyover bridge over Dong Ting Lake in China's Hunan Province (Figure 1.8) [17].

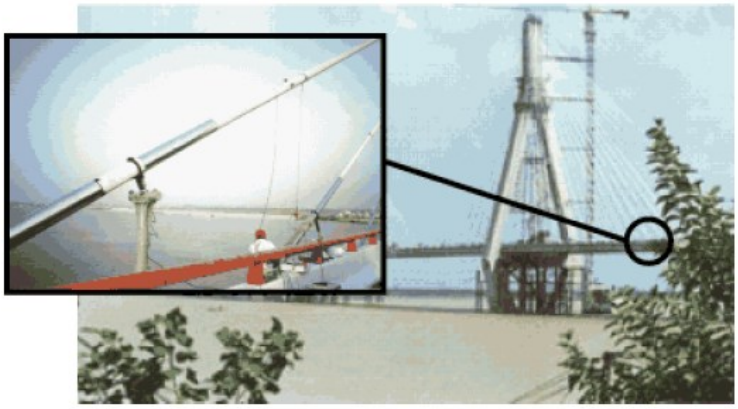

Figure 1.8 MR damper for the Dong Ting Lake [17]

The MR dampers were placed at the lower end of the cables. In this position, typical passive dampers would have limited efficiency. By using MR dampers, instead, positive results such as a significant reduction of vibrations in the bridge structure are achieved.

1.3.3 MRF applications in the biomedical field

Prostheses that are lightweight and consume minimum energy during their operation are always desirable. Thorarinsson et al. [18] developed a MRF based transfemoral prosthesis, depicted in Figure 1.9a, which consists of a small MR absorber placed at the knee which, depending on the various signals received from the sensors placed on the prosthesis, adapts with very fast reaction times to make the arthritic movement smooth and quite spontaneous.

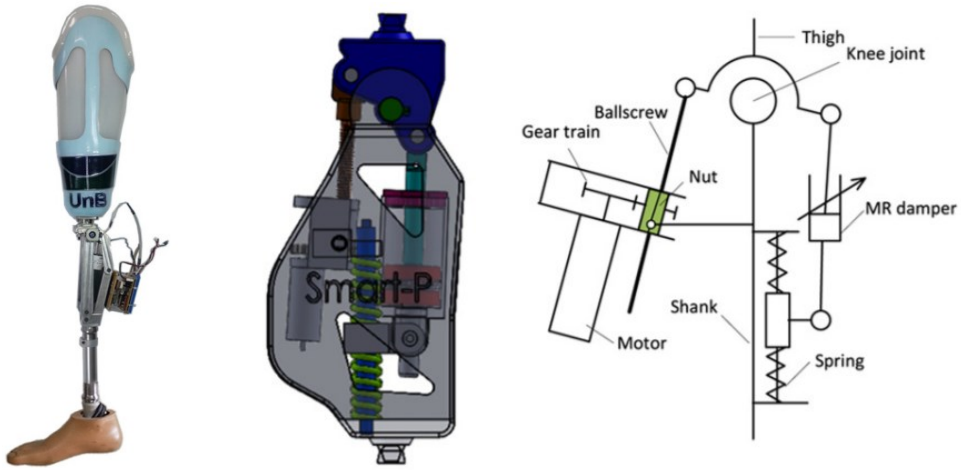

(a) (b)

Figure 1.9 (a) MR transfemoral prosthesis [18] (b) Schematic diagram of MR damper-based knee prosthesis [19]

Gao et al. [19] also worked on magnetorheological damper (MRD) based prostheses. They investigated the optimal weight of the MR damper. The knee model consisting of mechanical components such as gear transmission, a ball-screw nut transmission, optimized MR damper, springs, and a DC motor is shown in Figure 1.9b.

1.3.4 MRF in manufacturing applications

Despite the interesting properties of the MRFs, still few applications in the manufacturing sector can be found on the available literature. MRFs are used in magnetorheological finishing processes that consist of removing and finishing materials by exploiting the abrasive properties of the fluids themselves[20] [21]. An example of the use of MRFs is shown in Figure 1.10.

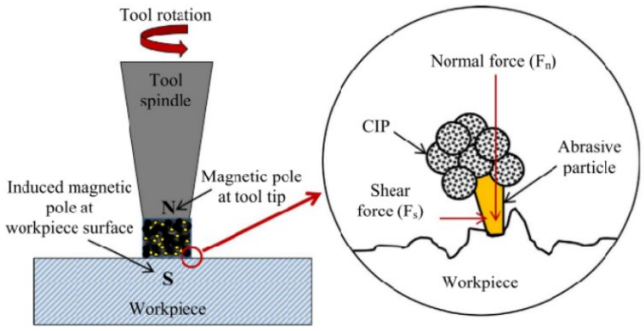

Figure 1.10 Schematic of the magnetorheological finishing process [21]

During finishing two types of forces act on the abrasive: normal force due to the magnetic field and shear force due to the shear strength of the MRF. So, when the tool rotates, the gripped abrasives in contact with the workpiece surface provides the finishing action by shearing off the roughness peaks.

Puma-Araujo et al. [22] proposed a new device based on MRFs to mitigate chatter for milling operations of thin-floor components. The device is shown in Figure 1.11.

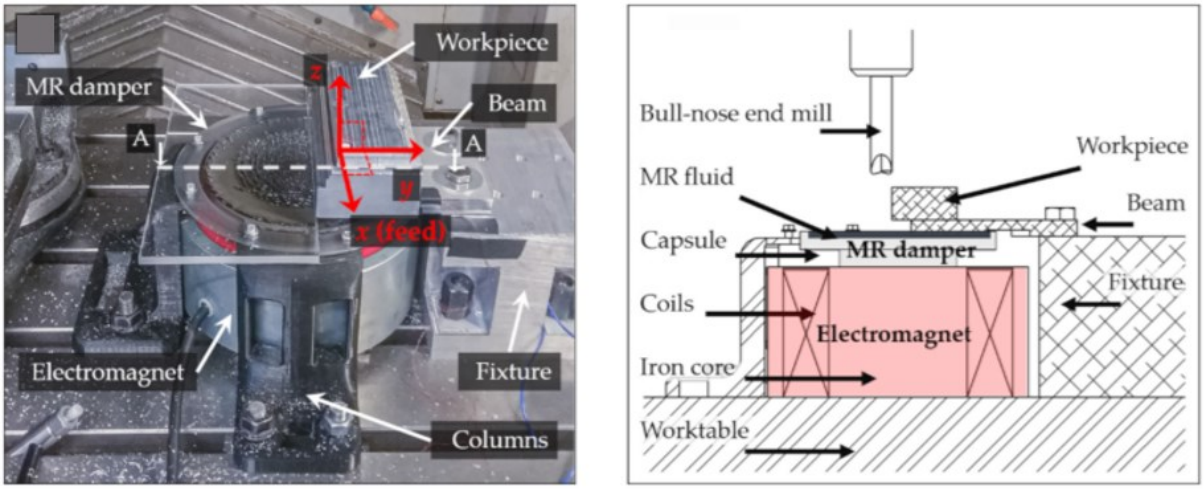

Figure 1.11 (a) Experimental setup and MR damper installation; (b) Schematic of cross-section A–A, the assembling of capsule–MRF is placed above the electromagnet. [22]

The MR damper device is a pool-like chamber fabricated in a non-magnetic acrylic material; an electromagnet is placed between the worktable and the MR damper. Once the electromagnet is energized independently of the machining, it generates a magnetic flux with which it is possible to control MRF yield shear stress and then reaction torque. The results showed that using MR damper device, machining is way more stable than in absence of MR damper in such a way that stable cutting conditions are enhanced, increasing the critical depth of cut with an increase in the material removal rate and productivity.

The use of MRFs have been studied also for applications in sheet metal forming processes [23], [24], [25]. The innovation of this proposed technology in the field of sheet metal forming

applications is represented by the possibility of managing the formability of the sheet during the entire forming process with very reduced times thanks to the control of an easily adjustable electrical parameter. During this process, as it can be seen in Figure 1.12, the fluid is placed on the surface of the sheet metal, previously clamped between the die and the cylinder, while the punch moves at a certain speed. As the magnetic field strength changes, the MRF is able to rapidly and reversibly alter its rheological characteristics.

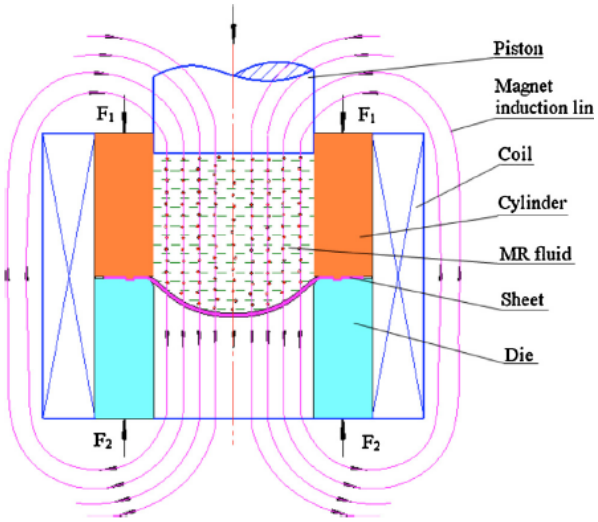

Figure 1.12 MRF application in a sheet metal forming process [23]

The parameter to modify is the viscosity of the forming medium, which directly affects the formability of the sheet. Wang et [26] studied the effect of the magnetic field density on the formability of aluminium sheets by means of bulge tests using MRF as forming medium.

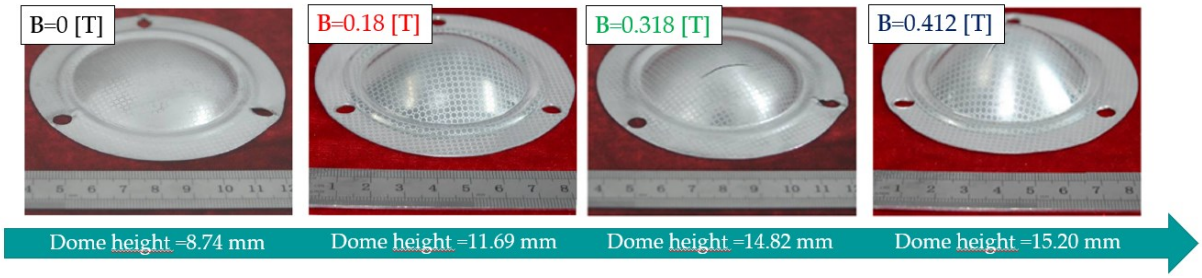

Figure 1.13 Dome height of the samples obtained by means of bulge tests using MRF (adapted from [26])

They found that when the magnetic flux density increases, the average height of the bulged sample dome increases, as shown in Figure 1.13. Thus, the possibility to modify the rheological properties of the forming medium (in particular the viscosity) in a continuous and reversible way through the regulation of the magnetic field, would allow the production of components of complex shapes at low costs: the intensity of the magnetic field, in fact, is easily manageable by acting on the current intensity.

1.4 MRF characterization for sheet metal forming applications

In sheet metal forming processes, accurate determination of the flow stress of pressure-carrying medium is significant. The property of the pressure-carrying medium (i.e. flow stress or stress-strain curve) has an impact on the loading and transmission of the force, which directly affects material flow and product quality [23]. Moreover, the adoption of a robust numerical modelling with reliable constitutive models of the material (resulting from the material characterization) allows to predict the materials' performances under certain conditions. The characterization tests should reproduce the operational conditions of the material. Thus, for the MRF, they should take into account the operational modes described in section 1.2.

The Bingham model described in section 1.1.1 is able to describe rheological properties in shear mode devices such as brakes, clutches, spindles and dampers [27].

For the squeeze mode, Mazlan et al [11] proposed a procedure to study the stress–strain characteristics in compression of MRFs under different applied currents and starting with different gap sizes. The adopted set up is shown in Figure 1.14a: the bottom of the upper cylinder and the bottom of the vessel containing the MRF are two parallel surfaces. A measured amount of fluid was sandwiched between these two parallel surfaces, so that the fluid was compressed in a direction normal to these surfaces when the upper cylinder moved towards the bottom of the vessel containing the fluid.

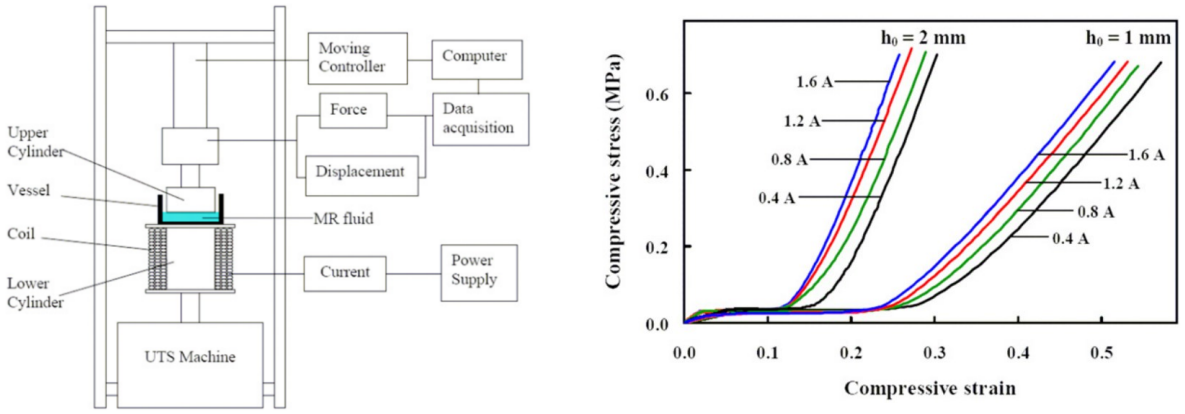

(a) (b)

Figure 1.14 (a) Set-up for the MRF compression tests (b) Comparison between two different initial gap sizes under various applied currents during the process of compression. [11]

Results (Figure 1.14b) showed that the compressive stress of MRF is strongly affected by the initial gap size and applied current; in fact, higher values of compressive stresses are required when both the initial gap size and the applied current increase.

However, none of the above-mentioned operational modes can be adopted for describing the MRF behavior when used in a sheet metal forming process. In fact, in this case, the MRF is

subjected to a three-dimensional stress state. To study the rheological behavior of the fluid in a sheet metal forming process, it is therefore necessary to use experimental data obtained by subjecting the MRF to a triaxial stress state. To this aim, Wang et al. [23] proposed a methodology that combined experimental data obtained from extrusion tests with numerical simulation to characterize the MRF. Figure 1.15a shows the schematic of the adopted experimental set-up: the cavity consists of a cylindrical part and a truncated cone part.

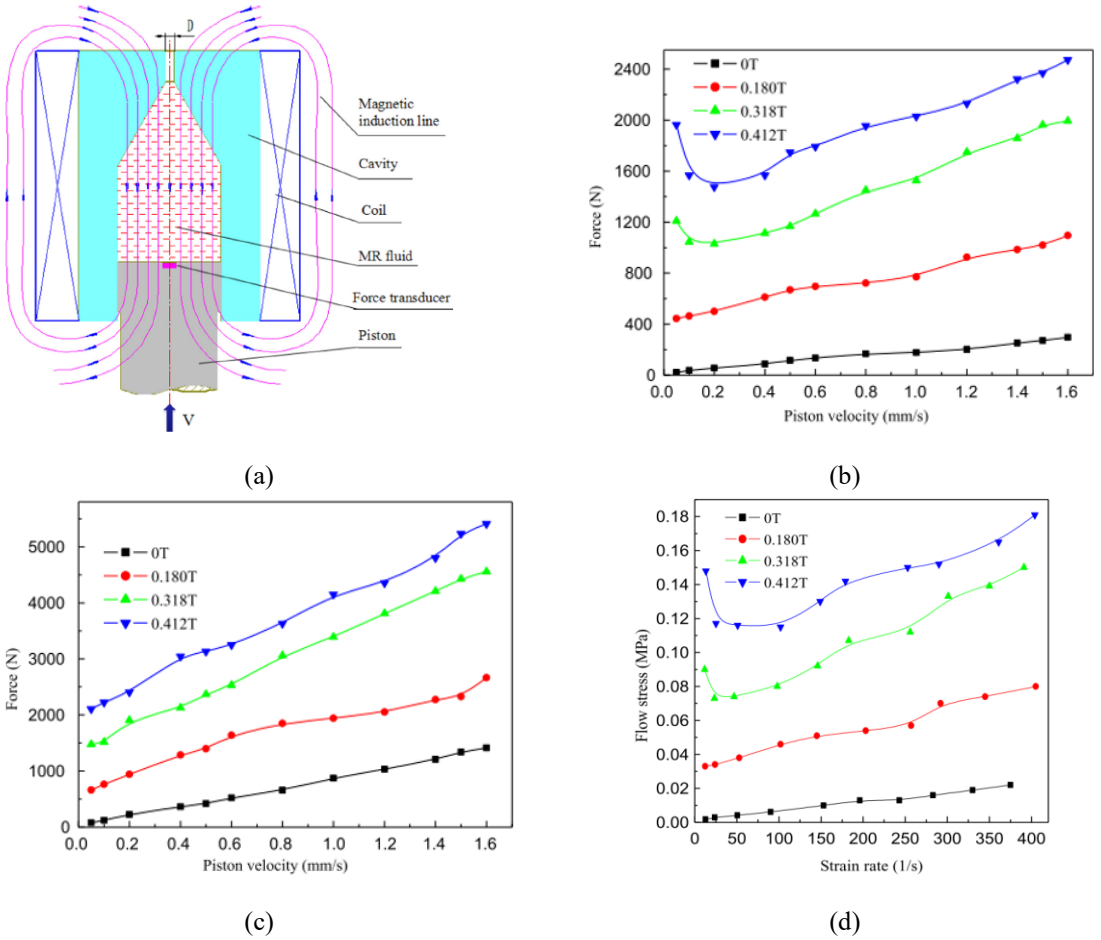

Figure 1.15 (a) Schematic of the experimental set-up for the MRF extrusion tests (b) Force vs. piston velocity curves for different magnetic fields for a hole diameter of 1.2 mm (c) Flow stress vs. strain rate curves of MRF under four different magnetic fields (d) Force vs. piston velocity curves for different magnetic fields for a hole diameter of 0.5 mm [23]

The piston moves in the cylindrical part and the upper hole is used to extrude the fluid. In their experimental campaign, they varied the hole diameter, the piston velocity and the applied magnetic field and they recorded the extrusion force during the tests. Then, they conducted FE simulations modelling the MRF as a rigid-perfectly plastic body and varying a constant flow stress until the calculated force matched the experimental one. Finally, they obtained a flow stress for a certain piston velocity and magnetic field and they acquired a strain rate value from the corresponding simulation. After acquiring enough stress and strain rate couples, they established flow stress curves under different magnetic fields. Figure 1.15b,c show the force

vs. piston velocity curves for different magnetic fields for a hole diameter of 1.2 mm and 0.5 mm, respectively. Comparing the two figures, it can be seen that the force increased when increasing both the piston velocity and the applied magnetic field. In addition, comparing the two figures it can be noticed that, as expected, also the hole diameter affects the force results. The resulting flow stress curves under different magnetic fields for the hole diameter of 1.2 mm are shown in Figure 1.15d.

Although this method would allow to model the rheological behaviour of the MRF and to obtain a flow stress-strain rate curve to implement in the FE simulations, it has some limitations. In fact, the results are affected by the geometrical characteristics of the experimental set-up (i.e. the hole diameter). Moreover, modelling the MRF as a rigid-perfectly plastic body does not take into account the elastic properties of the MRF, which were founded by Liu et al. [28] to be not constants when varying the magnetic field, as shown in Figure 1.16.

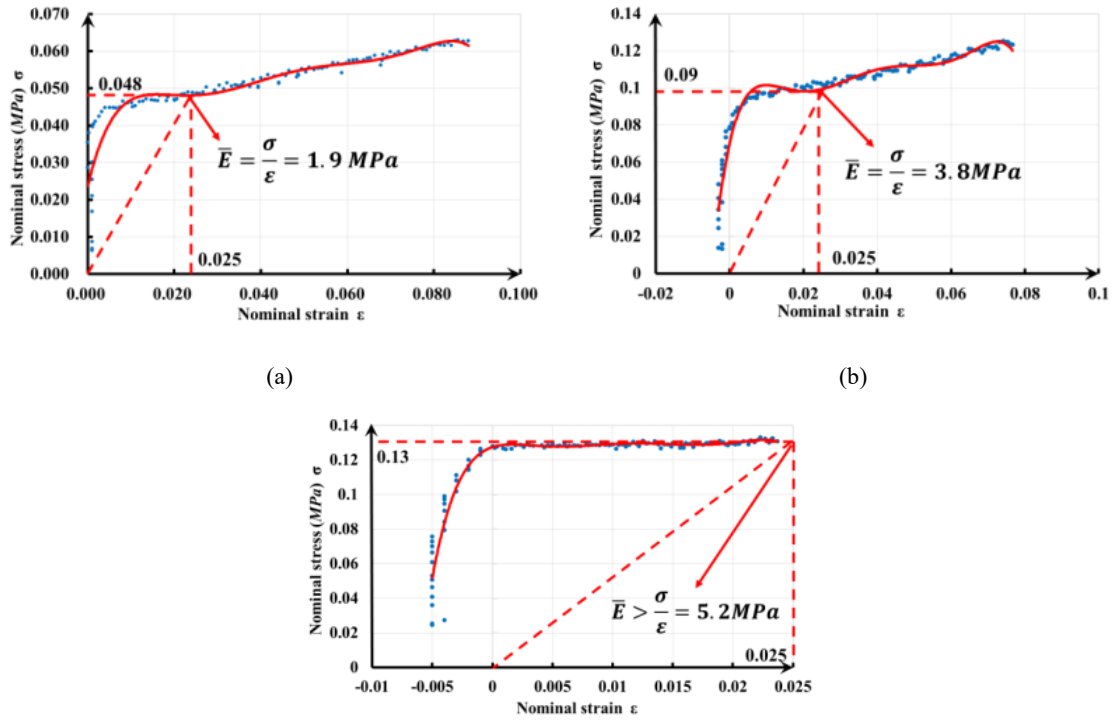

Figure 1.16 Nominal stress-nominal strain curves and young's modulus under different magnetic field density. (a) under 200mT; (b) under 340mT; (c) under 440mT

In particular they found that Young's Modulus, E, varied from 1.9 MPa when a magnetic field density of 200 mT was applied (Figure 1.16a) to values higher than 5.2 MPa when applying a magnetic field density of 440 mT (Figure 1.16c).

2. MRFs as forming medium for sheet metal forming processes

The following subsections provide an overview of the current lightweight materials used in the transportation and biomedical sector as well as the present and possible future strategies adopted to manufacture complex-shaped parts starting from them, to provide the technologic scenario in which the MRF-based sheet metal forming processes are placed.

2.1 Lightweight alloys selection for different sectors

Lightweighting is becoming a challenge in many industrial sectors associated with all forms of transportation, civil infrastructure, manufacturing and clean energy technologies since it allows to consume fewer resources for its manufacturing as well as it requires less energy for its transportation, thus preserving natural resources and reducing the harmful pollution [29].The aim of lightweight design is to build structures with a minimal use of materials and an optimized utilization of the material strength. To this aim, numerical methods are continuously developed to design the processes to obtain the complex geometries of lightweight parts.

2.1.1 Lightweight alloys for the transportation sector

In transportation industries, lightweight design is a key driver to reduce CO_2 emissions [30,31]: the increasing demand for electric and hybrid powered cars requires the adoption of light components for maximal weight reduction [32] and thus, the fuel consumption and associated emissions [33]. Also in the aerospace industry, there are on-going efforts for the reduction of aviation emissions due to the high contribution of aviation to global warming phenomena and environmental pollution. In fact, the international civil aviation organization target is to reduce aviation emissions by 50% by 2050 [34].

In aerospace and automotive industry, steel is one of the most commonly used structural material due to good manufacturability and availability, extremely high strength and stiffness in the form of high strength steels, good dimensional properties at high temperatures, as well as the lowest cost among commercial materials. According to the strength criterium, steels are classified as traditional mild steel, conventional high-strength low alloy (HSLA) steel and advanced high-strength steel (AHSS) [35]. The AHSS steels have complex multi-phase microstructures containing bainite, martensite, and residual austenite, which allow them to achieve unique mechanical properties as can be seen in Figure 2.1, thus being good candidates for the purpose of light weighting.

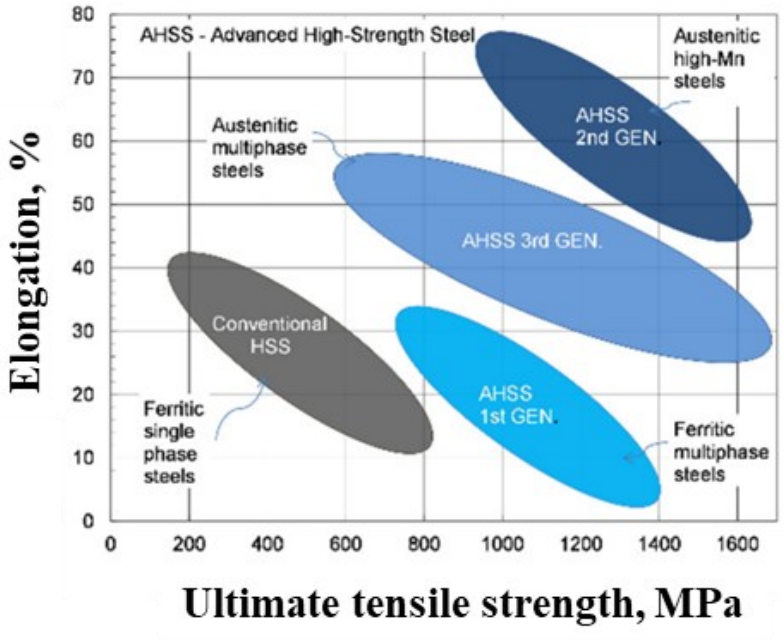

Figure 2.1 (a) Schematics of formability–strength relationships in AHSS [36]

However, high density and other disadvantages, such as relatively high susceptibility to corrosion and embrittlement, restrict the application of high strength steels in automotive and aerospace components and systems.

Titanium alloys have many advantages over other metals, such as high specific strength, high stiffness, good fracture toughness and fatigue resistance, as well as very good corrosion resistance, heat resistance, cryogenic embrittlement resistance, and low thermal expansion. Hence, the titanium alloys are used where high strength is required but limited space is available, as well as where high corrosion resistance is required. The current applications of titanium alloys in the aerospace industry are mainly in air frame and engine components whereas in the automotive industry they are used for highly loaded components in engine parts. Figure 2.2 shows the development of typical practical titanium parts in the automotive sector, the kinds of titanium and alloys used and the applied automotive names. However, the poor formability at room temperature and high cost (usually about 8 times higher than commercial Al alloys) result in the restriction of titanium alloys being extensively used.

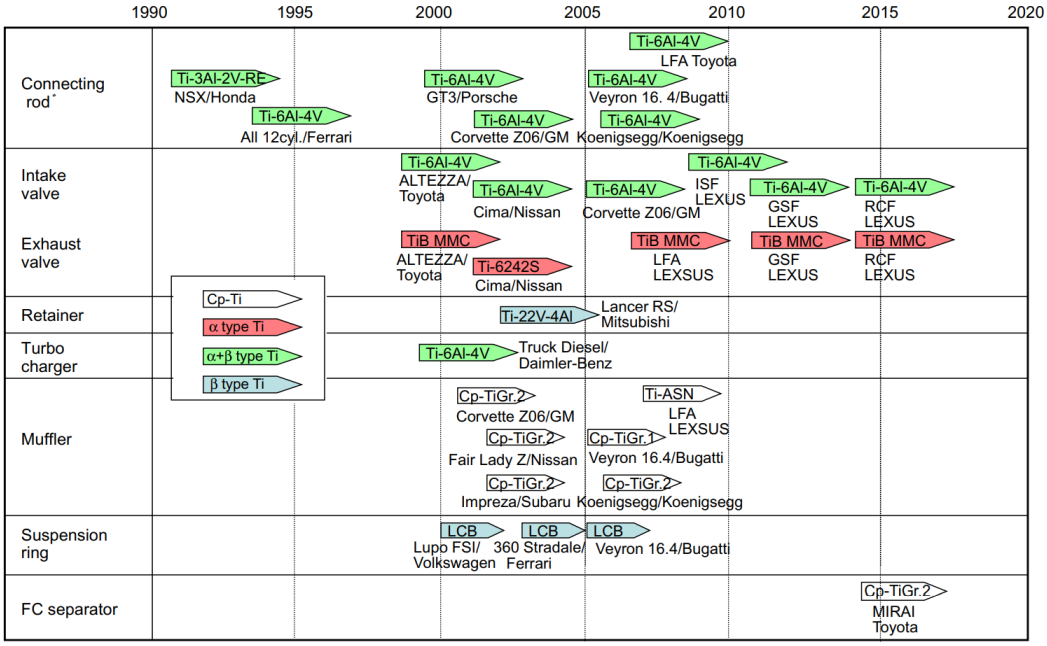

Figure 2.2 Development chronologically of typical practical titanium parts [37]

Aluminium alloys are a significant proportion of aerospace structural weight as demonstrated in the examples of materials distribution for some typical Boeing aircrafts in Figure 2.3, even if high performance composites such as carbon fibre are receiving increasing interest. The relatively high specific strength and stiffness, good ductility and corrosion resistance, low price and excellent manufacturability and reliability make advanced aluminium alloys a popular choice of lightweight materials in many aerospace structural applications, e.g. fuselage skin, upper and lower wing skins and wing stringers.

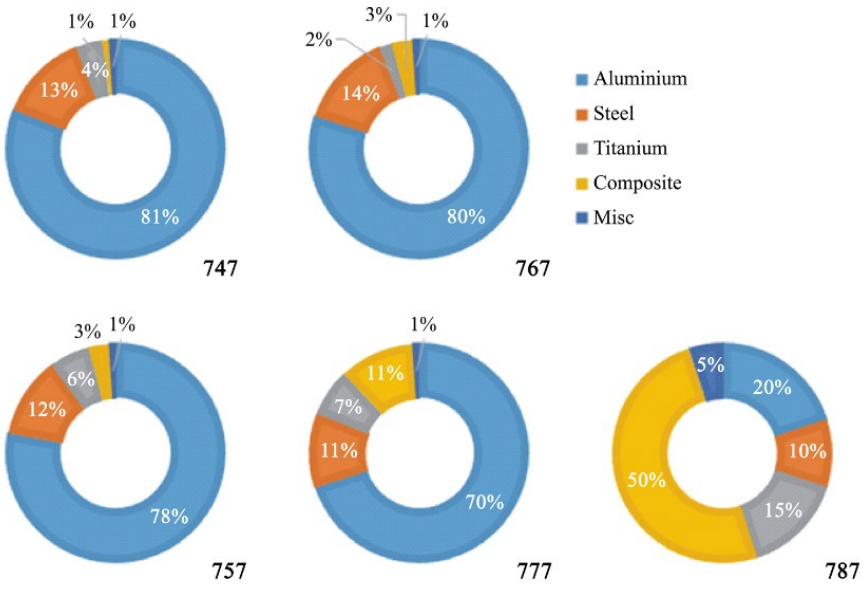

Figure 2.3 Material distributions for a selection of Boeing products[38]

The most extensively used aluminium alloys in the aerospace industry are the Al-Cu alloys (2xxx series), Al-Zn alloys (7xxxseries) and Al-Li alloys, whereas in the automotive industry Al–Mg, Al–Cu, and Al–Mg–Si within 2000, 5000, and 6000 series are mostly used [39]. Figure 2.4 summarizes the main properties and the typical applications of different alloys in the automobile and aircraft industry.

Industry	Alloy grade	Main chemical composition	Density (kg/m^3)	Strength/Density (Pa/(kg.m^{-3}))	Applications
Automotive	AA5052	Al-Mg	2680	72,000	Interior panels and components, truck bumpers and body panels
	AA5754		2670	86,000	Inner body panels, splash guards, heat shields, air cleaner trays and covers, structural and weldable parts, load floor
	AA6016-T4	Al-Mg-Si	2700	81,500	Outer panels and structural sheets (Europe)
	AA6111-T4		2710	103,000	Outer and inner panels (North America)
	AA7020-T6	Al-Zn-Mg	2780	127,000	Potential applications for A pillar and B pillar
Aircraft	AA7055-T7751	Al-Zn-Mg	2860	222,000	Case of fuselage
	AA7075-T73		2810	180,000	Upper wing skins, stringers and horizontal/vertical stabilizers
	AA2024-T3	Al-Cu-Mg	2780	1,740,000	Upper wing structure
	AA2199-T8	Al-Cu-Li	2640	152,000	Fuselage and lower wing structure

Figure 2.4 Lightweight properties and applications of typical aluminium alloys in automotive and aircraft industries [41]

Among the above-mentioned materials, the most used materials in the transport sector are steel and aluminium [41]. Comparing the two materials, the cost of an aluminium body normally exceeds the cost of steels considering only the cost of the structure itself; however, the difference in terms of the overall vehicle manufacturing cost is less [42]. Moreover, aluminum alloys allow the reduction of vehicle weight. In fact, one of the most important benefits of using aluminum alloys in automotive industry is that every kg of aluminum, which replaces 2 kg of steel, can lead to a net reduction of 10 kg of CO_2 equivalents over the average lifetime of a vehicle [39]. Aluminium alloys are expanding their applications. In fact, the European Aluminium Association has foreseen in its Executive Summary [44] that until 2027 aluminium use in all main sectors will increase steadily, as shown in Figure 2.5.

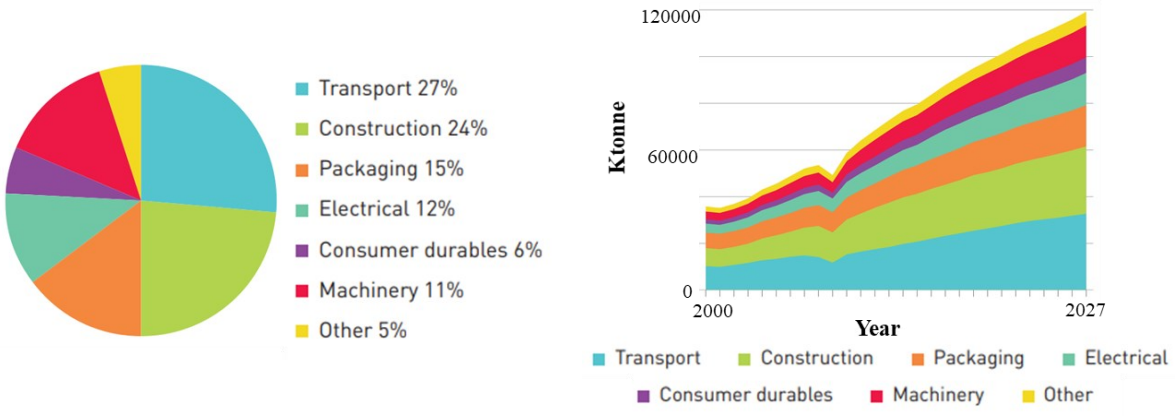

(a) (b)

Figure 2.5 (a) Worldwide end use application for aluminium; (b) Global aluminium end use sectors. [44]

In particular, from Figure 2.5a it can be seen that among the end use application of aluminium the transport sector has the higher percentage (27%), whereas from Figure 2.5b it can be noticed that until 2027 an annual growth of 3-4 percent is expected worldwide. The differences of mechanical properties of different Al alloys arises from the addition of alloying elements. As each element has a different solute ability within the aluminium matrix, the type, quantity and combination of alloying elements results in variations in microstructure and mechanical properties [41].

Among the Aluminum alloys, the 5XXX series alloys are preferred in the ground transport industry, due to their high strength/weight ratio, excellent formability (if formed in warm conditions) and corrosion resistance in harsh environmental conditions [42]. In recent years, the use of 5754 alloys has significantly increased in fuel oil tank, heat shield, engine cover and interior panel applications, which require high strength and good formability [43]. AA5754 is a non-heat treatable aluminium alloys and its strengthening mechanism is strain hardening, normally by coldworking during fabrication, in association with solution hardening. Therefore, AA5754 sheet components are normally cold stamped in the annealed (O), as fabricated (F) or strain hardened (H) conditions with greater ductility [41].

Although the aluminum alloys have high-strength to weight ratio and good corrosion resistance, the low formability of aluminum sheets limits their use in some products with complex shapes, such as body parts for the transport sector [43]. The formability is usually evaluated through a diagram containing a collection of major and minor strain points determined by different strain conditions (it is called Forming Limit Diagram, FLD). A FLD can distinguish between safe points and necked or failed points.

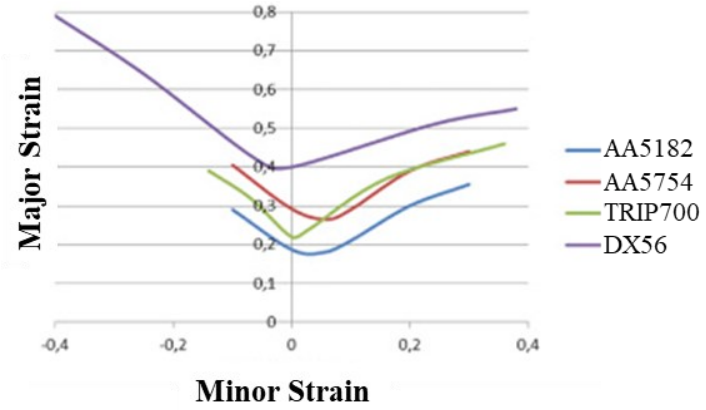

Figure 2.6 Comparison of the FLC at RT of aluminium alloys (AA5182, AA5754) and steels (TRIP700, DX56) [42]

The transition from safe to failed points is defined by the forming-limit curve (FLC). Figure 2.6 shows the Forming Limit Curve (FLC) at Room Temperature (RT) of two aluminium alloys

(AA5182 and AA5754) widely used in the transport sector and two steels (DX56 and TRIP700): it can be seen that the formability of these aluminium alloys is slightly lower about 10%.
However, solutions for increasing the working temperature to overcome the drawback of the poor formability of aluminium alloys has been largely investigated in literature [47] and will be discussed in the following sections.

2.1.2 Lightweight alloys for the biomedical sector

In the last 60 years, a great deal of research works and advancements in the biomaterials field have been made. At the moment, the most commonly used metallic biomaterials are Stainless steels, Cobalt-based alloys, Titanium alloys, Magnesium alloys, NiTi shape-memory alloys, Zirconium alloys and silver [56].
Among them, Magnesium is a widely available metal: it is the sixth most abundant element in the earth's crust, representing 2.7% of it and it is the third most abundant mineral dissolved in the sea water, after sodium and chlorine. It is the lightest of all structural metals, as it has a density of 1.74 g/cm^3, which is about one quarter if compared to steel (7.2 g/cm^3), one-third if compared to Titanium (4.51 g/cm^3) and two-thirds if compared to Aluminium (2.71 g/cm^3). These characteristics, as well as its good damping properties, make Mg alloys attractive for engineering applications when weight is a critical design element. As a biodegradable material, Magnesium and its alloys fall into the second generation of implant biomaterials, which contains bioactive materials, that could interact with the biological environment to enhance the biological response and the tissue or surface bonding, as well as resorbable biomaterials (such as Magnesium), which have a progressive degradation while new tissue regenerates and heals [57]. It is worth mentioning that corrosion is normally an undesirable phenomenon in engineering applications. In the field of biomedical applications, on the contrary, implants that 'biocorrode' might be very useful. Deploying them not only abrogates the need for implant-removal surgery, but also circumvents the long-term negative effects of permanent implants. For example, although pure titanium is a relatively inert metal and thus it is ideal candidate for fabricating an implant, studies have indicated that a long-term implantation may lead to electrochemical corrosion and therefore the production of wear particles which may result in inflammatory reactions [58].
Moreover, Mg-based materials also do not significantly interfere with Magnetic Resonance Imaging (MRI) compared to other metallic materials. Thus they allow accurate assessment of the device function during the post-operative periods [59].

The interest in Mg alloys for medical applications is also because they show mechanical properties that are closer in value to those of the human bones. Table 2.1 shows some physical and mechanical properties of metallic implant materials and bones [60].

It can be noticed that Mg has a much lighter density than other implant materials and moreover its fracture toughness, elastic modulus and compressive yield strength values are more similar to those of the human bone than the other commonly used metallic materials. It should be also considered that the greater elastic modulus of titanium and other orthopaedic metals might determine a stress shielding effect on the bone that it is stabilizing, which can ultimately lead to conditions such as osteopenia [58].

Materials	Density (g/cm^3)	Fracture Toughness ($MPa\ m^{1/2}$)	Elastic Modulus (GPa)	Compressive Yield Strength (MPa)
Natural bone	1.8–2.1	3–6	3–20	130–180
Ti alloy	4.4–4.5	55–115	110–117	758–1117
Co–Cr alloy	8.3–9.2	—	230	450–1000
Stainless steel	7.9–8.1	50–200	189–205	170–310
Magnesium	1.74–2.0	15–40	41–45	65–100
Hydroxyapatite	3.1	0.7	73–117	600

Table 2.1 Physical and mechanical properties of metallic implant materials and cortical bones [60].

Moreover, Mg is also present as a natural ion in the human body, whereby approximately 1 mol of Mg is stored in a 70 kg adult human body and an estimated amount of half of the total physical magnesium is present in the bone tissue.

Currently, the application of Mg and its alloys in the biomedical field is restricted to screws, rods and metal plates, which, once implanted, would provide mechanical support and gradually degrade, providing the space for the growing bone tissue.

In 2007, Duygulu et al.[61] machined cortical bone screws from magnesium alloy AZ31 extruded rod and implanted them to hip-bones of sheep via surgery (Figure 2.7).

(a) (b)

Figure 2.7 (a) Mg screw (b) Screw implantation via surgery in hip-bone of a sheep [61]

Three months after the surgery, the bone segments carrying these screws were removed from the sacrificed animals and there was a significant amount of corrosion on the magnesium screw

and a new bone was created at the interface: degraded magnesium alloy screw was replaced by this newly formed phase of Ca and P.

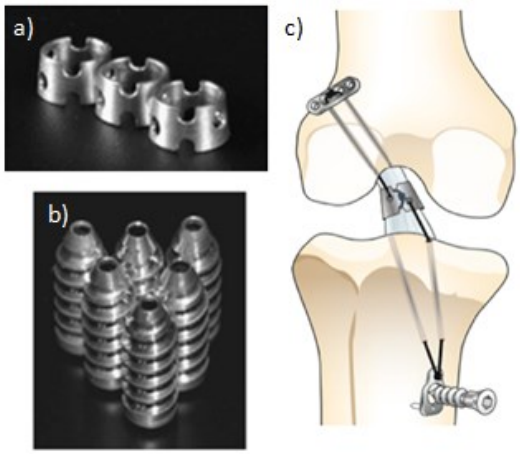

Figure 2.8 Photograph of the a) Mg-based ring, b) Mg-based interference screws and c) a schematic diagram of Mg-based ring repair of the ACL [62]

In 2014, Farraro et al. [62] presented two examples of Mg-based orthopaedic devices: an interference screw to accelerate Anterior Cruciate Ligament (ACL) graft healing and a ring to aid in the healing of an injured ACL (Figure 2.8). In vitro tests showed that both devices could restore function of the goat stifle joint and in-situ forces in the replacement graft and Mg-based ring-repaired ACL were also similar to those of the intact ACL. Further, early in vivo data using the Mg-based interference screw showed that after 12 weeks, it was non-toxic and the joint stability and graft function reached similar levels as published data.

The most important obstacle in forming Mg is that it is difficult to plastically deform it at room temperature because it has a hexagonal close-packed (HCP) crystalline structure (Figure 2.9), which restricts slips to the basal plane.

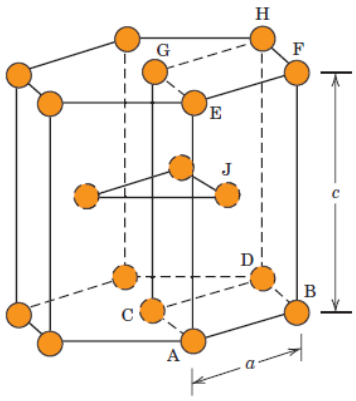

Figure 2.9 Hexagonal close-packed crystal structure [55]

However, several studies on Mg alloys (especially AZ31) have been done and they all showed that at higher temperatures (200÷300°C) additional sliding planes are activated increasing the ductility and lowering the yield stress, which improves the forming behaviour [63]. Therefore, if an appropriate forming temperature is adopted, it is possible to form complex shapes and get higher levels of strain. This will be discussed in the following sections. Another drawback of Mg in many engineering applications and especially in biomedical field is its low corrosion resistance, especially in electrolytic, aqueous environments, loosing mechanical integrity before the tissue has sufficiently healed. Unprotected magnesium exposed to a typical atmosphere will develop a gray oxide film of magnesium hydroxide ($Mg(OH)_2$) which slows corrosion. These films of $Mg(OH)_2$ are slightly soluble in water, however severe corrosion occurs in aqueous physiological environments where chloride ions are present at levels on the order of 150mmol/L, as $Mg(OH)_2$reacts with Cl^- to form highly soluble magnesium chloride and hydrogen gas. The following equations summarize the corrosion reactions of magnesium:

$$Mg(s) + 2H_2O \rightarrow Mg(OH)_2(\mathrm{s}) + \mathrm{H}_2(g) \quad (8)$$

$$Mg(s) + 2Cl^-(aq) \rightarrow MgCl_2 \quad (9)$$

$$Mg(OH)_2(\mathrm{s}) + 2Cl^- \rightarrow MgCl_2 \quad (10)$$

The release of hydrogen gas may lead to the formation of gas pockets around the implant [64]. Eq. 8-10 also indicates that it is possible to evaluate the corrosion rate from the volume of hydrogen evolved. Several studies were made to overcome this relevant drawback and to demonstrate that the degradation rate could be controlled by coating the Mg substrate with various materials, such as Calcium phosphates (CaP) and polymeric coatings.

2.2 Technological solutions to obtain lightweight complex-shaped parts

Several technological solutions have been developed to manufacture complex-shaped parts starting from lightweight alloys. Among them, conducting heat treatments on the material, the adoption of suitable forming processes such as Superplastic forming (SPF), Incremental Sheet Forming (ISF) and Sheet HydroForming (SHF) seem to be viable alternatives to standard processes (like machining, casting and stamping) and to innovative ones (like Additive Manufacturing techniques). The following subsections give an overview of the above-mentioned solutions.

2.1.2 Heat Treatments for changing mechanical properties before forming

To overcome the poor formability at room temperature of both magnesium and aluminum alloys, the most used strategy is forming such alloys at elevated temperature [52] [54]. Figure 2.10 shows the effect of temperature on the formability of two aluminum alloys, namely Al 5754 (Figure 2.10 a) and Al 6111-T4 (Figure 2.10) and one magnesium alloy, namely AZ31B (Figure 2.10 c). From the figure it can be seen that increasing temperature, formablity of all the materials increased and comparing the two aluminum alloys, the strain hardened alloy (Al 5754) show considerably greater improvement than the precipitation hardened alloy (Al 6111-T4) with increasing the forming temperature.

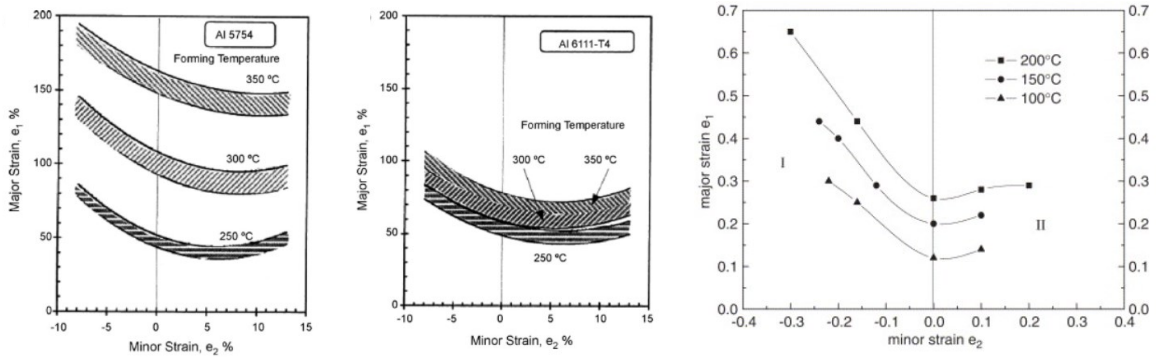

(a) (b) (c)

Figure 2.10 Effects of forming temperature on FLD for aluminum alloys [58] (a) Al 5754, and (b) Al 6111-T4 and (c) a Mg AZ31B alloy [59]

Moreover, by using localized heat treatments, it is possible to tailor the distribution of material properties according to the requirements of the forming process [60]. There are several ways to conduct local heat treatments. The most common methods are heating by induction (Figure 2.11a) [61], heat conduction (Figure 2.11b) [62] and laser irradiation (Figure 2.11b) [63].

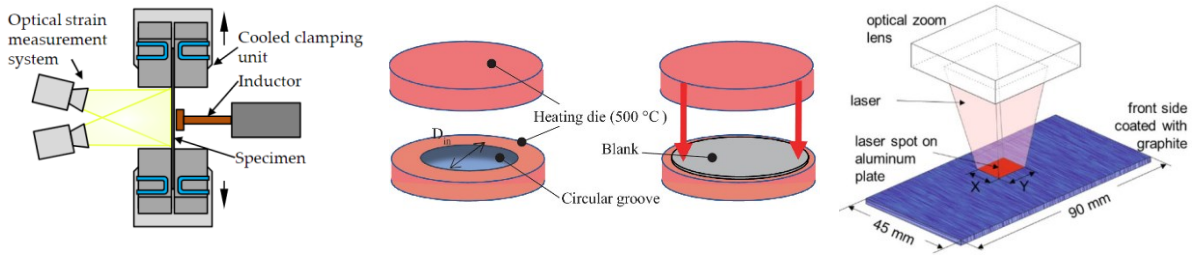

(a) (b) (c)

Figure 2.11 Local Heat Treatment by (a) induction; (b) heat conduction and (c) laser irradiation

Because of the low setup and adjustment effort as well as the localized heating, using lasers for heating has proven to be advantageous for the local treatments [64], [65]. However, when heating alloys by laser radiation, the high thermal conductivity of the alloys represents a big

challenge for an effective treatment; in fact, ensuring enough energy to soften the material must be balanced with the need to localize as possible the treated region and limiting the heat transition zone [66]. To conduct an effective Local Laser Heat Treatment, the main process parameters must be properly selected; they are shown in Figure 2.12a and they are the holding time (t_{up}), which as to be as short as possible, cooling time (t_{cool}) and the maximum temperature (T_{max}) [67]. Moreover, when a large area has to be treated, the path of the laser spot must be optimized to maximize the distance between successive paths [68], thus guaranteeing the correct heat distribution, cooling phase and minimizing distortions.

Piccininni et al. [69] conducted a local laser heat treatment on the periphery of a circular Aluminum specimen (AA 6082-T6) and used a cylindrical cooler to keep the temperature low in the central region, as shown in Figure 2.12b.

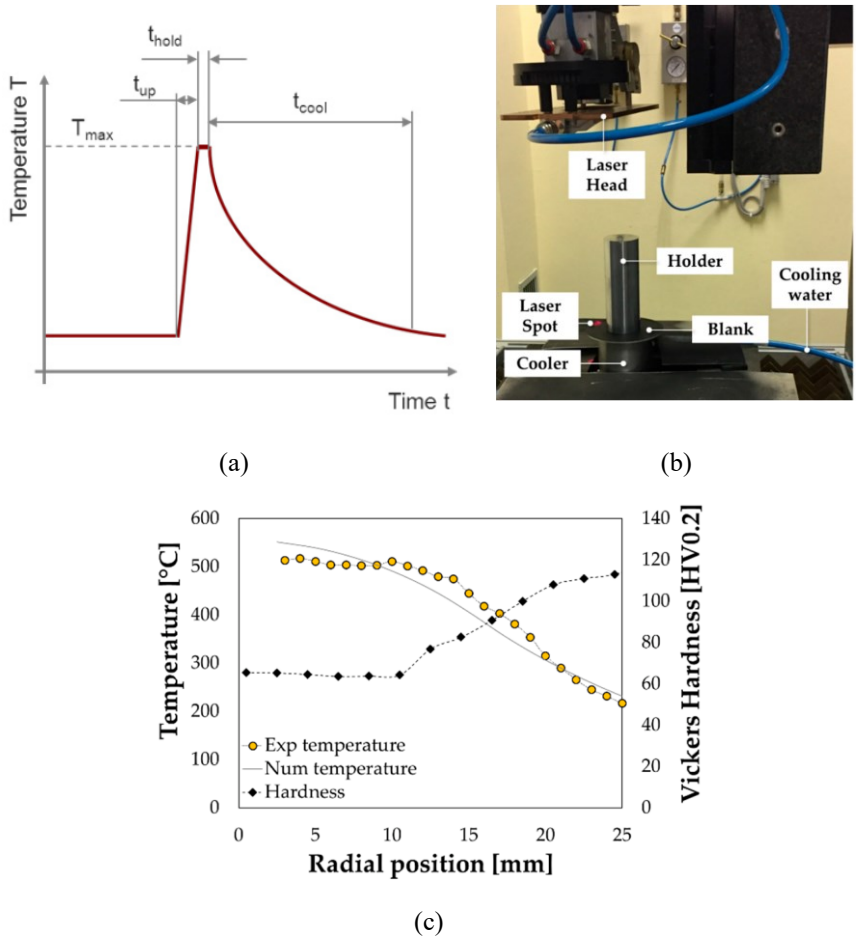

Figure 2.12 (a) Temperature vs. time profile during laser heat treatment [54]; (b) Experimental set-up adopted by Piccininni et al. [69] for the local laser heat treatments on AA6082-T6 specimens (b)Main results of the local laser heat treatment by Piccininni et al [69]

Results showed that the laser heating was effective bringing the hardness values in the treated region (the peripherical one) sensibly lower than those measured close to the blank center (Figure 2.12c).

Guglielmi et al. [70] conducted a localized Laser Heat Treatment on the center of a commercial AZ31B-H24 Mg circular alloy sheet (Figure 2.13a) to evaluate the effectiveness of the heat treatment, they analysed the microstructure evolution along a longitudinal path on after the laser heat treatment, shown in Figure 2.13b.

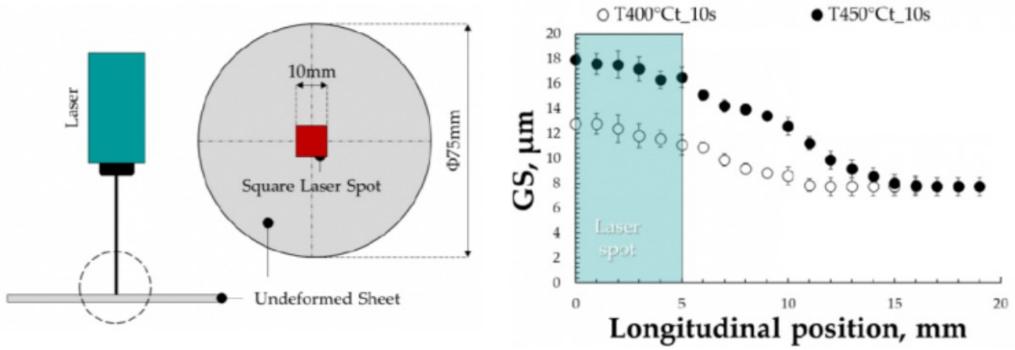

(a) (b)

Figure 2.13 (a) Scheme of the experimental setup adopted to perform localized Laser Heat Treatments (b) Grain size distribution obtained after the laser heat treatments performed at 400°C and 450°C [70]

From the Figure 2.13 it can be seen that the grain size gradually grown from a value of 9 µm in the not treated zone to 12 µm 18 µm in the heat-treated zone when the target temperature in the heat treated zones were 400°c and 450°C respectively.

2.1.3 Superplastic Forming

Superplastic Forming (SPF) is a hot forming process in which a metal sheet is sealed around its periphery between a blank holder and a die having a shaped cavity; the tools and the sheet are maintained at the superplastic temperature (greater than 0.5 T_m, where T_m is the melting temperature of the material, to allow reasonably high diffusion processes during deformation) and gas pressure is applied to make the sheet form into the die cavity; the strain rate is maintained in the superplastic range. Figure 2.14 shows a schematic representation of the process. The SPF is mainly adopted for aerospace [71] and automotive [72] applications; but it also represents a suitable technology for customized prostheses production, being able to produce parts characterized by very complicated shapes due to the very large strain level the material can experience when using optimal working conditions [73]. In addition, the accuracy of the part is excellent, where residual stresses and spring-back are negligible; however, the long cycle time and the strong surface oxidation due to the elevated forming temperature represent relevant drawbacks.

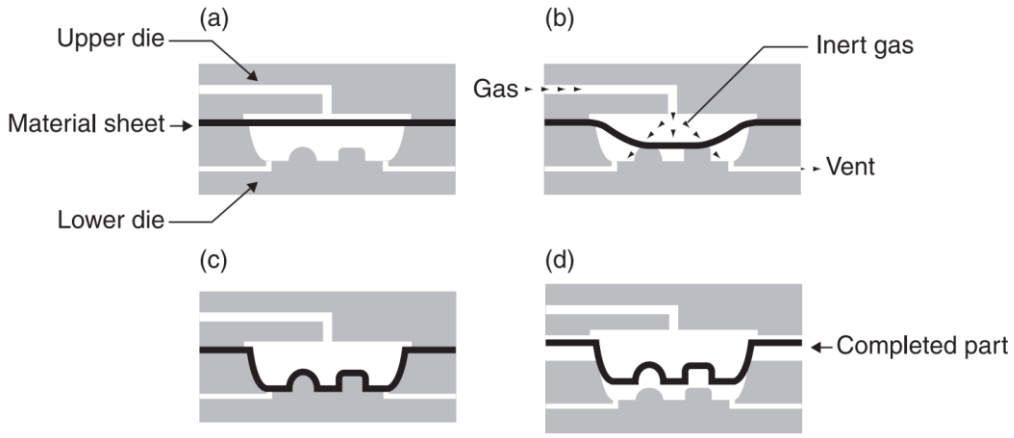

Figure 2.14 Schematic representation of the SPF process: (a) initial flat sheet inserted in between upper and lower dies; (b) progression of forming under gas pressure; (c) final shaped part in contact with lower die; and (d) removal of the part. [74]

2.1.4 Incremental Forming

Incremental Sheet Forming (ISF) is a flexible technology for producing complex and unique components, which is well suited for small scale production or prototyping in industries such as aerospace or medical. In fact, for small batches, ISF needs minimal initial costs when compared to conventional sheet forming processes such as stamping and deep drawing, due to the low level of complexity of its tools. ISF allows the forming of the sheets with minimal preparation time and manual processing, using conventional computer numerical control (CNC) machines, resulting in high flexibility and low tooling costs [84]. A schematic representation of the process is shown in Figure 2.15a. During forming, the part geometry is split into a series of two-dimensional layers and plastic deformation is obtained layer-by-layer through the progressive movement of a CNC controlled forming tool. On completion of each layer, the forming tool moves down of a small increment along the z-axis direction and continues to process the following layer, until all required layers are formed.

If compared to SPF, the strain level which can be obtained by ISF is certainly lower, but it should be considered that the process can be performed (e.g. when working Mg alloys) without any additional heat, since a large amount of heat is generated due to the friction between the forming tool and the sheet [76], which determines a great simplification.

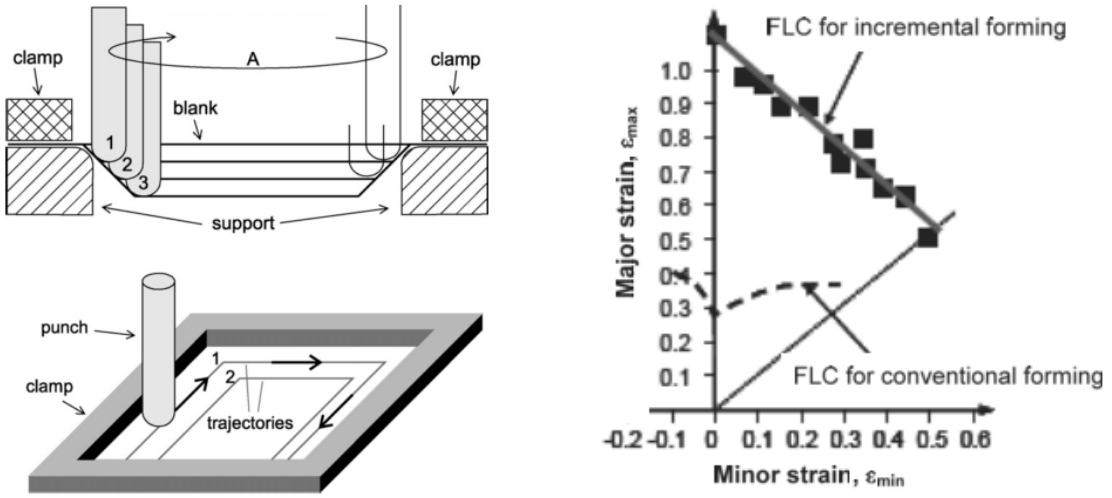

(a) (b)

Figure 2.15 (a) Schematic representation of ISF process [85].(b) FLD for conventional and incremental sheet metal forming [78]

In conventional sheet metal forming, the forming limit curves (FLC) have a V-shaped form and they are determined by the Nakajima or the Marciniak methods. Instead, in the case of ISF, as shown in Figure 2.15b, the FLCs are found to be linear, with a negative slope and all of their points fall into the $\varepsilon_2 \geq 0$ zone and they are commonly called Fracture Forming Lines (FFLs) [78]. It can be noticed that FLC for incremental forming goes much above the conventional FLC. On the other hand, the high forming time represents a limitation in the application of the ISF for mass production. Moreover, due to the lack of a die, the main drawback of the ISF process is the low accuracy, mainly because of the global springback that occurs once the final part is unclamped after it has been formed.

2.1.5 Sheet Hydroforming

Sheet Hydroforming (SHF) consists of the plastic deformation of a sheet thanks to the pressure exerted by oil or other pressurizing liquid media [88]. The fluid can act as an active tool ("Active style" in Figure 2.16b) [89] or can assist the tool ("Passive style" in Figure 2.16a)[90]. As a result of the liquid medium in the die cavity, which flows out between the upper surface of the die and the sheet metal, the friction between the sheet metal and die is reduced. This fluid flow results in a lubrication effect that reduces frictional forces [91]. By this process, the sheet metal can be drawn to a greater depth, limit drawing ratio value of sheet metal can be increased [92] and surface defects of the formed part can be reduced due to the liquid pressure medium [93]. On the other hand, the major drawbacks of Sheet Hydroforming are the low manufacturing

efficiency when compared with conventional stamping processes and the high manufacturing cost per part [94].

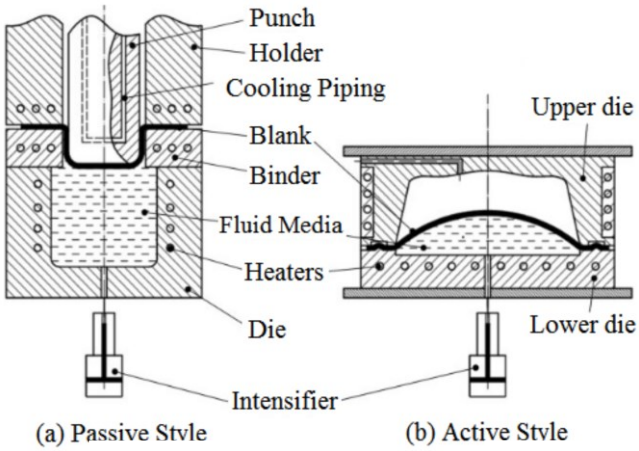

Figure 2.16 Schematic of SHF (a) Passive style (b) Active style [94]

To reach better performances in terms of formability of the component, Hydroforming is usually performed at high temperature [47], but novel contributions have been made also in terms of innovative forming media, such as viscous pressure forming (VPF), which uses a kind of semi-solid, flowable and viscous material as the pressure-carrying medium to improve the formability of sheet metal and improve the surface quality and the dimensional accuracy of the obtained parts [95]. The viscous pressure forming and in particular the VPF using a MRF as viscous forming medium has been detailed in section 1.3.4. In this way, it would be possible to overcome the limits that characterize the solutions available today for the regulation of the hydroforming process, namely the impossibility of varying the controlled parameters in an immediate way (for example the variation of temperature, which cannot be instantaneous) and the limited flexibility of the regulation is carried out by modifying the geometry of the blankholder [80], thus making the equipment difficult to set up.

2.3 Lightweight complex shaped components obtained with innovative technological solutions

After having mentioned the basic principles of the present technological solutions to manufacture complex shaped parts starting from lightweight alloys, the following subsections will give an overview of the applications of them to components for the transport and biomedical field.

2.3.1 Transport sector

The SPF process for aluminum alloys has been used in production for over two decades at various transport companies around the world [87]. Figure 2.17 shows an example of a part produced by SPF which is a light housing for a Boeing 737. By means of FEM analyses, the geometry of the initial tube was accurately predicted and the production components are now produced in a single process where preforming and final forming operations are performed in a single tool. The final product, which is shown in Figure 2.17, has approximately 70% elongation at the maximum strain location.

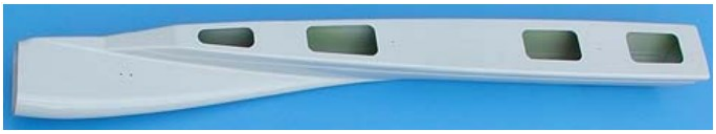

Figure 2.17 737 SPFed AA5083 light housing [87]

Yi et al [88] investigated by means of numerical-experimental approach the possibility of improving the thickness uniformity of an Al 5083 door frame by a two-stage SPF technique: this technique consists of two stages: first forming the shape of the pre-forming die for the purpose of local area thinning, and then blowing the preformed sheet in the opposite direction into the final die. They adopted Response Surface Methodology (RSM) to explore the effect of parameters (entrance fillet radius, bottom fillet radius, depth, the bottom area and draw angle) on the minimum thickness of the part and they obtained, by means of FE simulations, a suitable pressure curve, so that the minimum thickness met the requirements while reducing the production cycle.

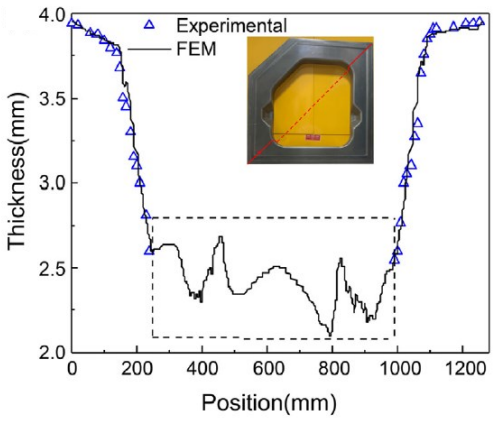

Figure 2.18 Numerical/experimental comparison of the thickness distribution for the test door frames formed by the two-stage SPF process [88]

They obtained a door frame with an acceptable minimum thickness and good contour accuracy. Figure 2.18 shows the comparison between the thickness measurement result of the test door

frames formed by the two-stage SPF process and the numerical simulation result, showing good agreement between them.

Iorio et al. investigated [89] the possibility of successfully manufacturing an Al 6060 motorbike tubular component by improving the hydroforming process with different local annealing strategies (Figure 2.19).

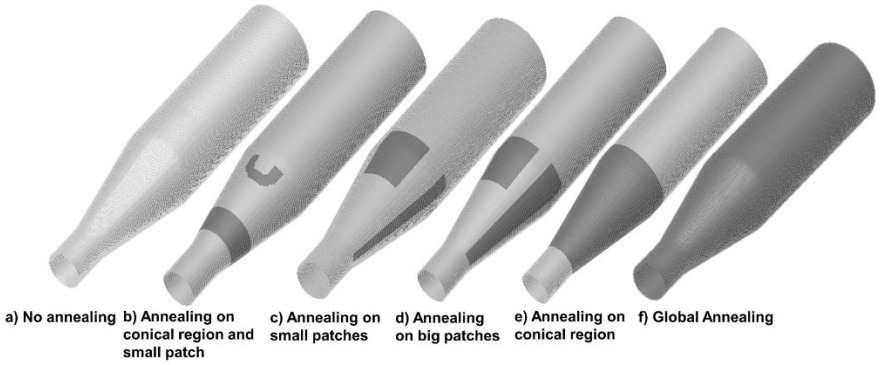

Figure 2.19 Different annealing strategies for improving HF process [89]

They performed both experiments and numerical simulations and demonstrated that a feasible solution can be found with local heat treatment of relatively small portions of the tube.

In a recent work, a combination of the SPF and SPIF technologies was studied, to obtain hemispherical component similar to fuel tanks for aerospace applications made of Mg alloy AZ31B-H24 with a uniform thickness distribution [90]. In particular, in the proposed approach, the blank is pre-formed by SPIF and subsequently processed by SPF, as shown in Figure 2.20. First, they assessed the optimal initial thickness distribution of the SPF process by means of a numerical approach. Then, they obtained such thickness distribution by means of SPIF process. Finally, they obtained the final component by means of the SPF process.

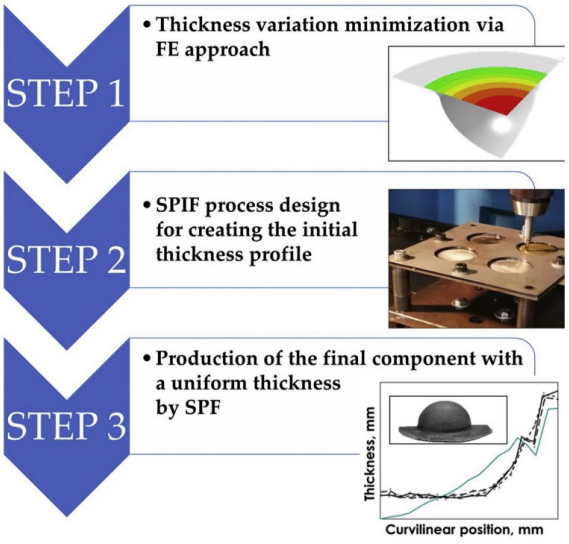

Figure 2.20 Combination of SPF and SPIF technologies proposed in [90]

In this way, the excessive thinning in some areas of the sheet (which is one of the most important SPIF limitations) is changed into a positive feature for the SPF application.

2.3.2 Biomedical field

In the biomedical field, the adopted technologies must guarantee a final component characterized by both high levels of geometrical accuracy and a uniform thickness distribution, since it affects the corrosion rate in body fluids. In spite of the transport sector, the biomedical field is usually characterised by a low volume production, thus the tooling cost is relevant for the selection of the manufacturing process. In literature several solutions to obtain medical implants involving the technologies presented in the previous chapter can be found.

Sorgente et al. [73] manufactured an Extra Low Interstitial Titanium alloy (Ti6Al4V-ELI) cranial prosthesis by means of the SPF process. They designed the implant starting from diagnostic images of an artificial and properly defected skull shown in Figure 2.21. Then, they designed the SPF process (in terms of pressure profile) using FE simulations, investigating different strain rate target levels. They found that the target strain rate had a strong influence on the final thickness distribution, as shown in Figure 2.21b.

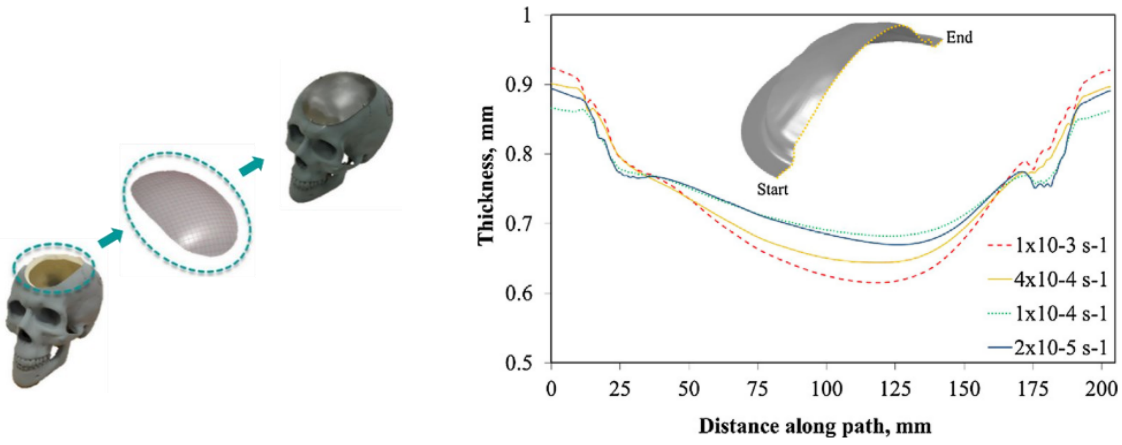

(a) (b)

Figure 2.21 (a) Titanium Cranial prosthesis produced by Sorgente et Al. (b) Thickness distributions at different target strain rate levels [73]

Araújo et al. [91] manufactured by SPIF a simplified model of the facial implant made from titanium grade 2 shown in Figure 2.22a. First, they analyzed their unsuccessful attempts, evaluating the interaction between circle grid analysis and formability tests to explain failure by cracking at critical geometric features of the facial implants. Then, taking advantages of FE simulations, they successfully obtained the facial implant shown in Figure 2.22b, by redesigning the facial implant to smooth the drawing angles of the surrounding walls, then

avoiding excessive thinning in regions B and E of the deformed blank and implant. This procedure allowed them to move the maximum strain values back to the safe region of the fracture forming limit diagram (i.e., to the region below the FFL in Figure 2.22b) to produce a safe facial implant by SPIF.

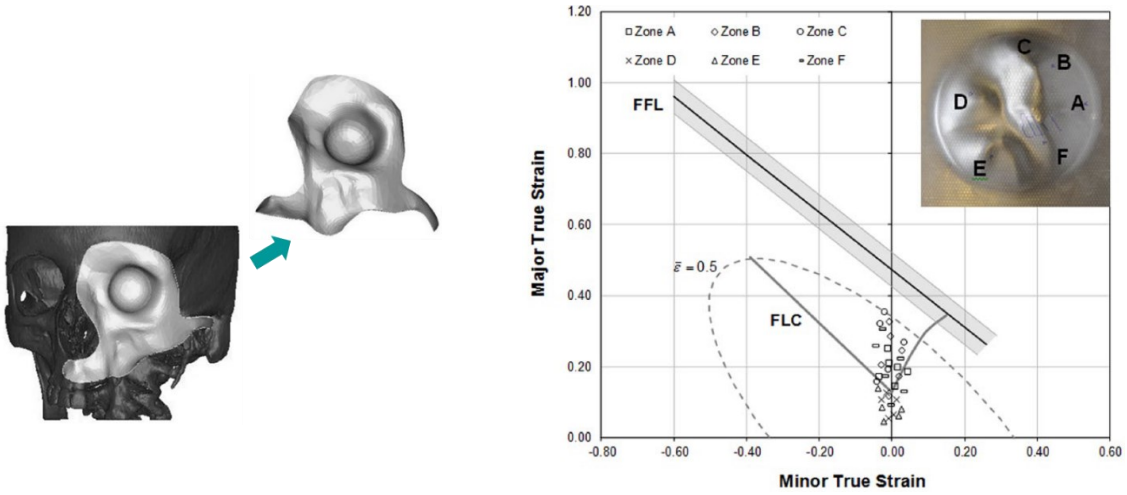

(a) (b)

Figure 2.22 (a) Facial Implant and its simplified model (b) FLC and FFL with identification of the zones A–F of simplified model of a titanium facial implant produced by SPIF [91]

3. Materials and methodologies

In this chapter, materials, methodologies and facilities adopted to achieve the research objectives are described. Experimental activities were conducted in the laboratories of Politecnico di Bari (Italy), Advanced Forming Research Centre (Glasgow, United Kingdom) and University of Girona (Spain).

3.1 Mechanical characterization of the investigated lightweight alloys

The characterization activities discussed in this dissertation were carried out on the following list of materials:

(i) MgAZ31B-H24, whose mechanical properties were investigated by means of tensile tests (both at room and higher temperatures), Single Point Incremental forming tests and deep drawing tests with MRF, to compare the possible technological solutions which allowed to better form the alloy;

(ii) AA5754-H32, whose mechanical properties were investigated by means of a new methodology based on the combination of laser heat treatments and bulge tests;

(iii) AA5754-H111, whose mechanical properties were investigated by means of tensile tests at room temperature; the obtained mechanical properties were then used for the inverse analysis approach adopted to characterize the investigated MRF; in fact, this methodology consisted of the combination of bulge tests conducted on sheets having known properties (in this case, AA5754-H111) and FE simulations which reproduced the experimental loading conditions varying the MRF's rheological properties to obtain them by means of an inverse analysis approach.

In the following subsections, information about the above-mentioned materials as well as the methodologies for their characterization is discussed.

3.1.1 The investigated lightweight alloys

The chemical composition of the AZ31B-H24 Magnesium alloy and AA5754 (both in H32 and H111 temper) Aluminum sheets used in the present thesis are shown in Table 3.1 and Table 3.2 respectively. Table 3.1 Chemical composition of the Mg AZ31B workpiece material.

	Al	**Zn**	**Mn**	**Ni**	**Fe**	**Cu**	**Si**	**Ca**	**Others**	**Mg**
% weight	2.5÷3.5	0.7÷1.3	0.2÷1.0	<0.005	<0.005	<0.06	<0.05	<0.04	0.3	Balanced

Table 3.1 Chemical composition of the Mg AZ31B workpiece material

Material	Si	Fe	Cu	Mn	Mg	Cr	Zn	Ti	Others
AA5754-H32	0.26	0.38	0.07	0.19	3.1	0.02	0.03	0.02	Balanced
AA5754-H111	0.09	0.28	0.02	0.17	2.9	0.15	0.01	0.02	Balanced

Table 3.2 Chemical composition of the AA5754 investigated alloy in the H32 and H111 temper

3.1.2 Tensile tests on AZ31B and AA5754-H111

Uniaxial tensile tests were conducted according to ISO 6892-2:2011, using the INSTRON 4485 universal testing machine, controlled by a Zwick-Roell software to set the value of the crosshead speed and acquire the test data (crosshead displacement and force measured by the load cell). For hot tensile tests, the specimens were heated by an induction heater (HEASYHEAT by AMBRELL®), that is a solid-state induction heating system able to convert three-phase line voltage to 10 kW terminal power output over a range of radio frequencies and voltages. This energy is delivered to a remote series resonant circuit, including coil, where a precisely controlled magnetic field is created closed to the sample. The induction heater is equipped by a PID controller to guarantee a constant temperature, which was continuously measured by two K-type thermocouples welded in the middle position of the specimen. Figure 3.1 shows the described experimental set-up.

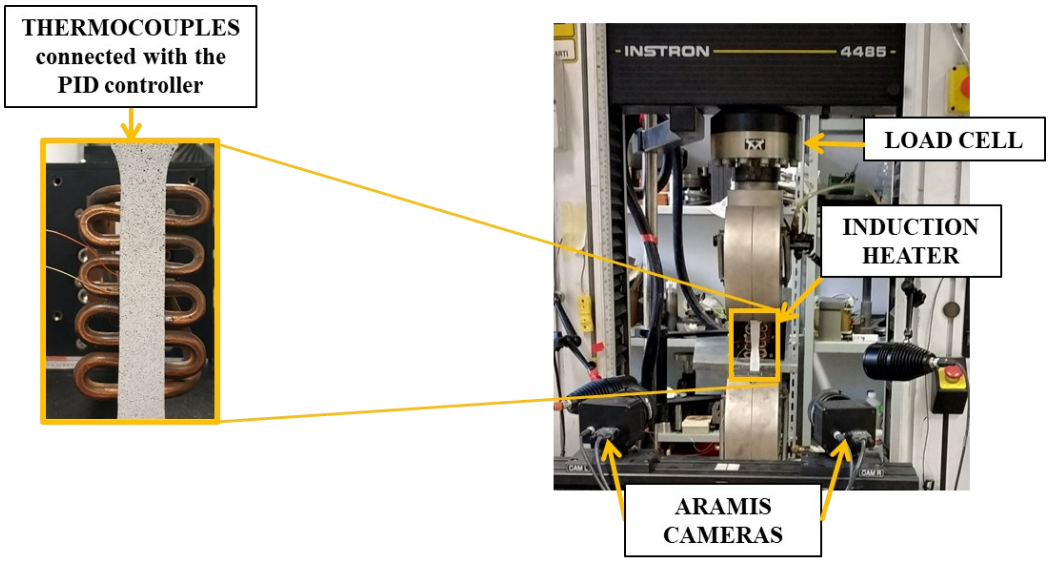

Figure 3.1 Experimental Set-up for hot tensile tests (b)Point selection and output graphs from GOM system

Before the tests, each sample was sprayed with a white matte layer to avoid reflections and then a random distribution of black dots was superimposed: the resulting pattern could thus be recognized by the two cameras as a virtual grid making possible the local evaluation of the strain at any possible specimen's location by means of a Digital Image Correlation (DIC) system (ARAMIS, GOM). Thanks to the interface between the Zwick Roell and GOM software,

it was possible to obtain the output desired values by locally analyzing a selected point (i.e., a point in the fracture area) on the strain map (Figure 3.2) and obtaining the stress vs. strain relationship. Stress-strain behaviour from tensile tests were then approximated by the Hollomon law.

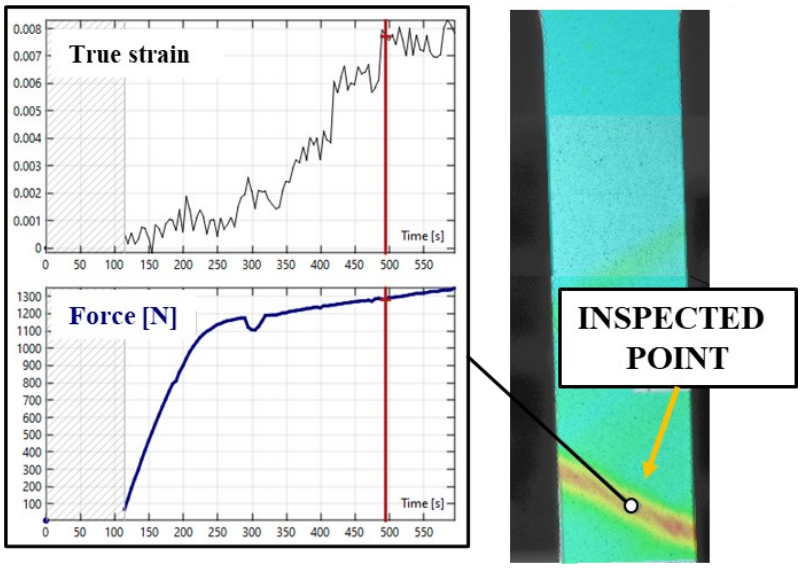

Figure 3.2 Point selection and output graphs from GOM system

For the AZ31B characterization, tensile tests were conducted on specimens extracted from a 1 mm thick blank, using three temperature levels (Room Temperature, 150 °C and 250 °C) and three levels of crosshead speed (4.2, 42, 420 mm/min), whereas tests on aluminum AA5754-H111 tests were conducted at room temperature on 0.5 mm thick specimens using a 6 mm/min crosshead speed.

3.1.2 Single Point Incremental Forming (SPIF) tests on AZ31B

The activities involving SPIF tests were performed in the workshops of University of Girona (Spain). The formability of the AZ31B alloy was evaluated by means of SPIFability tests, which were aimed at determining the ability of the material of reaching a target geometry without rupture by means of the SPIF process, thus obtaining a Forming Fracture Line (FFL). The geometry selected was a pyramidal frustum with circular generatrix (a cross section is shown in Figure 3.3a), which means that there was a variable wall angle at each depth increment. The length of the edges of the pyramid was 105 mm, the initial wall angle was 45° and the generatrix radius was set to 80 mm. The final geometry is shown in Figure 3.3b.

(a) (b)

Figure 3.3 (a) Section of the part geometry; (b) Formed part.

SPIFability tests were carried out on a Kondia® HS1000 3-axis milling machine equipped with Fidia® numerical control (Figure 3.4a). A punch having the diameter equal to 10 mm was used for all the tests. The initial sheet was cut into 150 mm × 150 mm size of blanks and 3 mm circle grid was marked on the surface. Then, it was clamped by a fixture system composed of a bottom plate, four supports, a clamping plate and a top plate (Figure 3.4b). The tool path was defined, and its direction was alternatively clockwise and anticlockwise, to avoid torsion of the part. To minimize friction effects, lubricant Houghton TD-52 for metal forming was applied over the upper surface of the blanks.

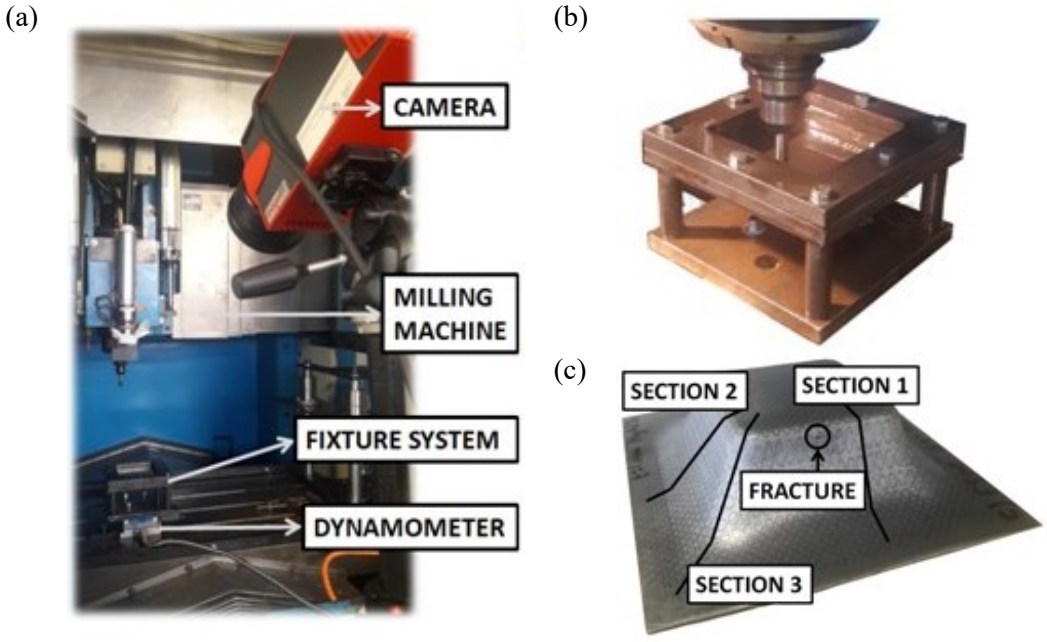

Figure 3.4 (a) SPIF Experimental Set-up; (b) Fixture system; (c) Sections for strain measurements

A large amount of heat was generated on the contact area between the forming tool and the metal sheet due to the friction, so no additional heating sources were needed. When the target geometry was reached, the tool went automatically up. If a fracture occurred during the process, the test was forced to stop. During the SPIF experiments, thermal and mechanical loads were

concurrently recorded. The material temperature variation during the process (T) was acquired with the thermographic camera IRBIS ImageIR 3300, at a frequency of 0.1 Hz. The temperature distribution on the blank during the entire experimental tests was then processed to obtain the maximum temperature for each test and its variation over time. After the experiments, the maximum depth achieved (Z_{max}) for each test was collected and used as formability indicator. Then, principal strains (ε_1, ε_2) were measured by means of circle grid analysis, using Grid Pattern Analyzer (GPA), a camera-based system that automatically measures surface strains. In this way, strains could be calculated due to the deformation of the circles determined by the forming process, as shown in Figure 3.5. The 3 mm circle grid was marked on the surface before each test, by printing the pattern on a thick paper sheet and transferring it to the Mg sheet through acetone. In particular, measuring the major and minor axes of the ellipses, major (ε_1) and minor (ε_2) strains could be determined (Eq. 11 and Eq.12):

$$\varepsilon_1 = \ln\left(\frac{a}{d}\right) \tag{11}$$

$$\varepsilon_2 = \ln\left(\frac{b}{d}\right) \tag{12}$$

being a and b the major and minor axes of the deformed ellipses after the forming process, respectively (Figure 3.5b), and d the initial diameter of the grid's circles on the undeformed blank (Figure 3.5a).

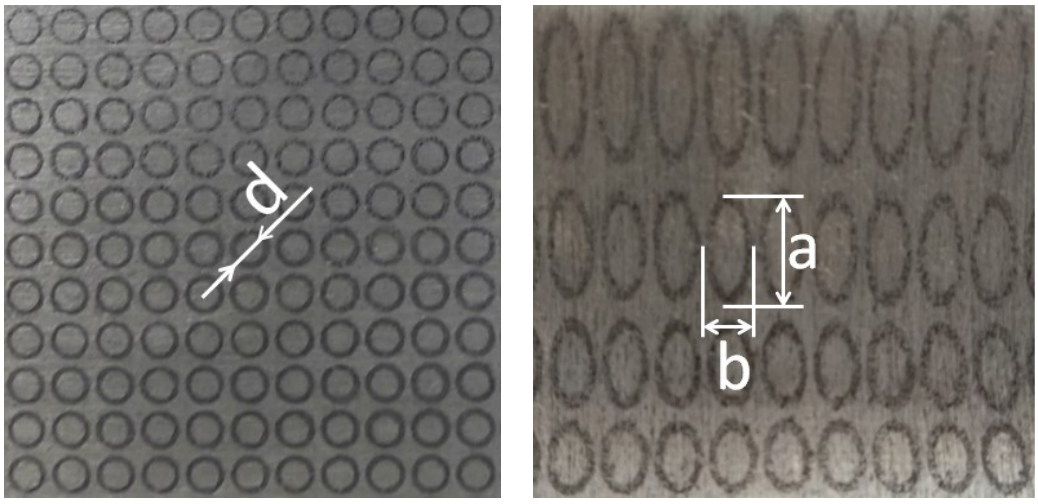

(a) (b)

Figure 3.5 Grid pattern (a) before and (b) after the deformation process

Then, the thickness along the considered section could be predicted. In fact, considering the material as incompressible, the thickness strain (ε_3) could be calculated assuming the volume constancy (Eq 13):

$$\varepsilon_3 = -(\varepsilon_1 + \varepsilon_2) \tag{13}$$

Thus, final thickness *t* could be evaluated as follows:

$$t = t_0 * e^{\varepsilon_3} \tag{14}$$

Then, the Fracture Forming Lines (FFLs) were obtained according to the procedure adopted by Bagudanch et al. [92]: the procedure started by measuring the thickness at fracture for three points along the crack to obtain the average thickness strain. The average thickness strain was evaluated at both sides of the crack for every tested specimen. The average minor strain was evaluated along the fracture line. The major strain was then calculated by volume constancy (Eq. 15):

$$\varepsilon_{1f} = -(\varepsilon_{2f} + \varepsilon_{3f}) \tag{15}$$

Where ε_{2f} is the average minor strain along the fracture line and ε_{3f} is the average thickness strain along the crack. Three different sections of each sample were analysed: the wall area containing the fracture (if it occurred), the corner area without fracture and a wall area without fracture (Figure 3.4c).

Samples were then extracted from the selected specimens to analyze hardness and microstructure according to the procedure shown in Figure 3.6.

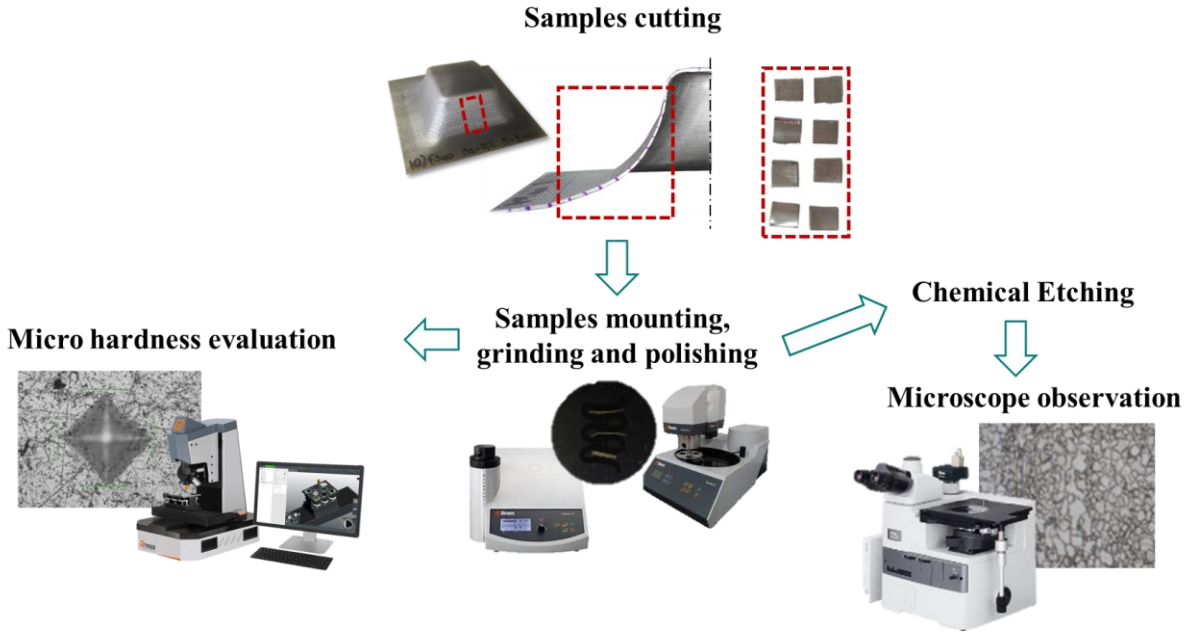

Figure 3.6 Procedure for Hardness and Microstructural analysis of the SPIFed samples

In particular, light microscope (Inverted Microscope Nikon MA200) was used to examine the microstructure of the samples extracted from the specimens processed by SPIF at two different forming depths (z), namely, z = 10 mm and z = 30 mm. The cross-sectional view was analyzed and compared with the as-received material (AZ31-H24). Before the analysis, each sample was cut, hot mounted, ground, polished, and etched by immersion for 5 s in acetic-picral solution (5 ml acetic acid, 6 g picric acid, 10 ml water, 100 ml ethanol). Then, according to the ASTM E112-13 standard, the Heyn Lineal Intercept procedure was applied to measure the average grain size [93].

Hardness tests were performed in accordance with the ISO 6507-1:2018 standard using a fully automatic Qness microhardness tester. The Vickers microhardness (load=100 gf, holding time=5 s) was measured along a five-points path located at half of the sample's thickness. The as-received sheet (AZ31-H24) and three selected blanks processed by SPIF were investigated. In particular, samples were extracted from the wall area of the formed parts and at the same forming depth (z = 30 mm).

A central composite design (CCD) was adopted: Spindle Speed (S), Step Down (Δz) and Feed Rate (F) were chosen as input variables. Low and high level for factors were 3000/5000 RPM for spindle speed, 0.2/0.5 mm for step down and 300/500 mm/min for feed rate. Center point of the CCD plan (replicated three times) was characterized by S= 4000 RPM, F=400 mm/min and Δz= 0.35 mm and star points by S= 2318/5682 RPM, F=232/568 mm/min, Δz= 0.1/0.6mm. According to the value of the step down, the target depth to achieve was not the same for each test: it was 42.6 mm for the tests performed using Δz= 0.6 mm, 42.7 mm for those carried out using Δz= 0.35 mm and 43 mm for the tests performed using Δz= 0.1/0.2/0.5 mm.

3.1.3 Hydraulic bulge tests on AA5754-H32

Hydraulic bulge tests were conducted in the Advanced Forming Research Centre's (AFRC) workshops (Glasgow, UK) on AA5754-H32 sheets, 1.5 mm thick, having an initial diameter equal to 250 mm. Figure 3.7a represents a general scheme of the bulge test, showing the experimental setup composed of a die (entry radius R_f equal to 10 mm) with a cavity diameter of 55 mm (R_d), a blank sheet (radius R_s equal to 125 mm), and the drawbeads on the blankholder located at a radial position 14.5 mm far (D_{sd}) from the die cavity. Before each test, the samples were prepared with the same speckled pattern described in section 3.1.2 . During the tests, the continuous strain acquisition and dome height (h_d) was recorded using GOM ARAMIS DIC cameras and a force (converted into a stress value) acquired from Zwick-Roell BUP1000 equipment.

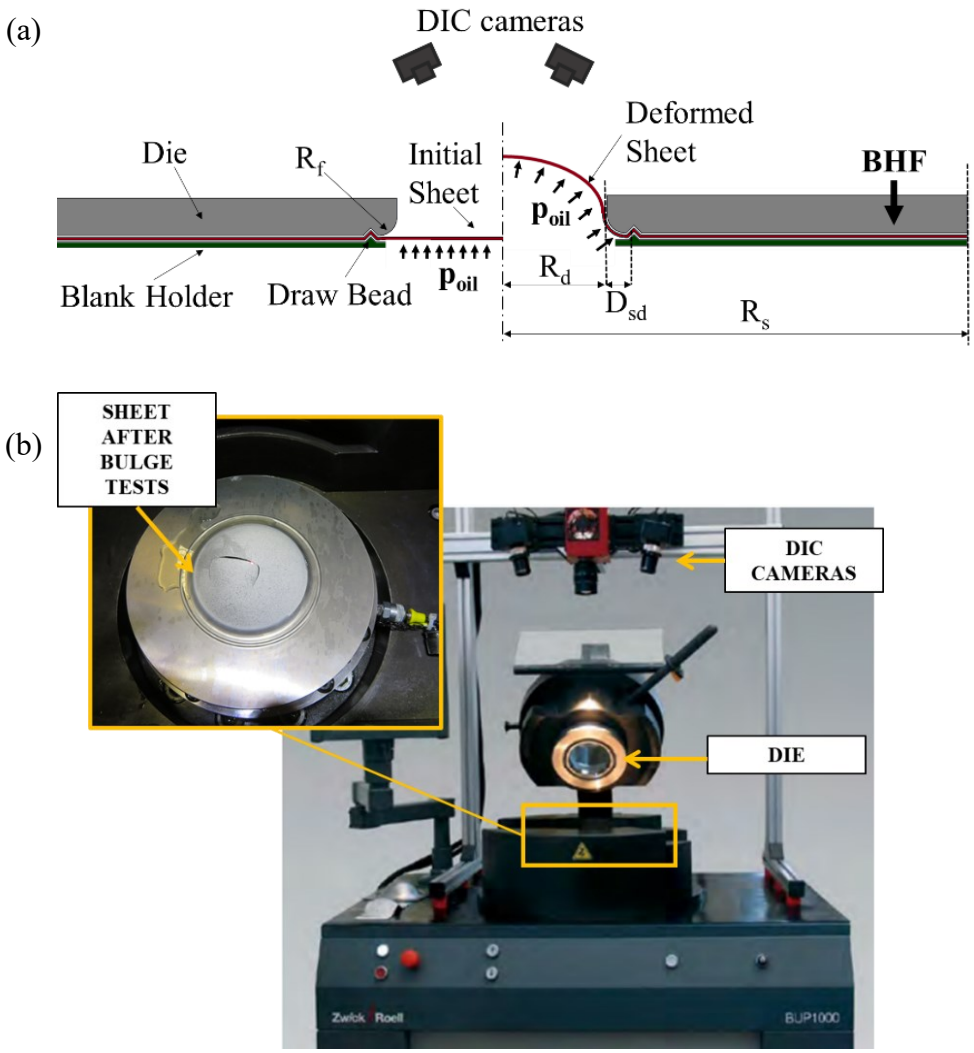

Figure 3.7 (a) Scheme of the Hydraulic bulge test (b) Zwick-Roell BUP1000 equipment (located in AFRC, Glasgow)

The following flow stress curve determination was based on the membrane theory [94]. In particular, on the pole of the specimen, the relationship between stress, bulging sheet geometry and bulge pressure could be established as (Eq. 16):

$$\sigma_b = \frac{p \cdot \rho}{2 \cdot t} \tag{16}$$

Where ρ is the curvature radius calculated from Eq. 17, t is the current sheet thickness calculated from Eq. 13 and 14, assuming that both surface strains values near the pole (ε_1 and ε_2) were equal (condition of equibiaxed strain on the sheet plane) and p was the pressure calculated from the acquired force (Eq. 18).

$$\rho = \frac{(R_f + R_d)^2 + h_d^2 - 2R_f h_d}{2h_d} \tag{17}$$

$$p = \frac{F}{\pi \cdot R_p^2} \tag{18}$$

Where R_p is the radius of the punch.

3.2 An innovative methodology to characterize AA5754-H32 sheets

The methodology described in this section aims at evaluating the feasibility of determining the right hand of the Forming Limit Curve (FLC), thus altering the strain path of circular specimen by means of local heat treatments while using the conventional circular aperture die for bulge tests. In particular, 3D Finite Element (FE) simulations were conducted setting different laser heating strategies and evaluating the resulting strain path. Then, the correlation between the laser heat strategies and the die aperture ratios for obtaining a particular slope was found.

3.2.1 Mechanical FE model

The hydraulic bulge tests were simulated using the commercial software Abaqus/Standard. To simplify the numerical model, only a quarter of the setup (shown in Figure 3.8a) was considered thanks to the geometric symmetries. Moreover, the mechanical seal was not modelled, and its action was taken into account by setting a suitable boundary condition.

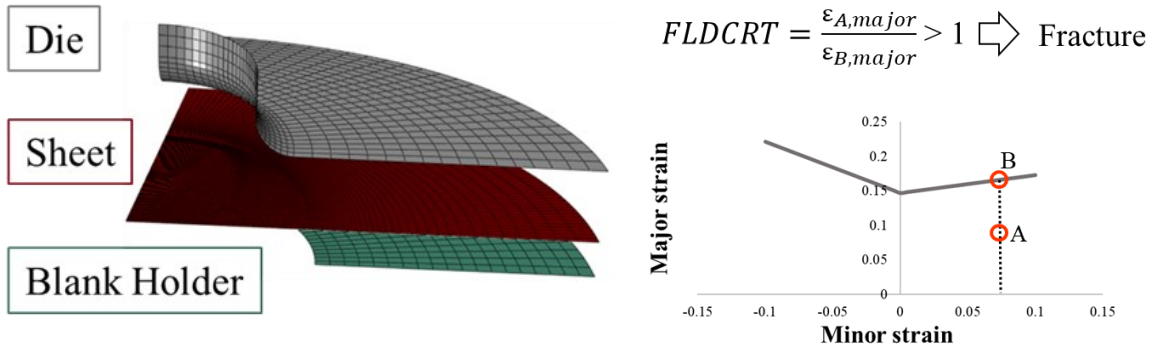

(a) (b)

Figure 3.8 (a) Schematic representation of the FE geometry (b) Representation of the FLDCRT output variable used to estimate the rupture of the sheets in FE simulations

The die cavity and the blank holder were modelled as rigid bodies whereas the blank as a deformable shell with an initial thickness of 1.5 mm, with five through-thickness integration points. The simulations were performed assuming a linear increase of the applied pressure on the inner surface of the sheet. To predict the occurrence of failure, the Forming Limit Diagram (FLD) damage initiation criterion was used. The Forming Limit Curve (FLC) for the AA5754-H32 sheets was analytically calculated from the flow curve obtained from the bulge tests described in the previous section, following the Extended Maximum Force Criterion (EMFC)

[95].The implementation of the FLC in the FE model activates an output variable, the FLDCRT, defined as the ratio between the calculated value of major strain (point A in Figure 3.8b) and the value of major strain on the FLC corresponding to the same value of the minor strain (point B in Figure 3.8b). The model predicts the occurrence of rupture when the FLDCRT variable overcomes the threshold value equal to 1.

3.2.2 Adopted approach

To obtain different strain paths, two different approaches were investigated:

- **Conventional approach** (Figure 3.9a): elliptical dies with different aperture ratios (a.r.) were used with a standard test sample.

- **LHT approach** (Figure 3.9b): a standard circular die was used with a "Laser Heat Treated" test sample, i.e. a circular specimen in which locally selected areas were laser heated to bring the material from the as-received condition (H32) to the annealed one (H111) .

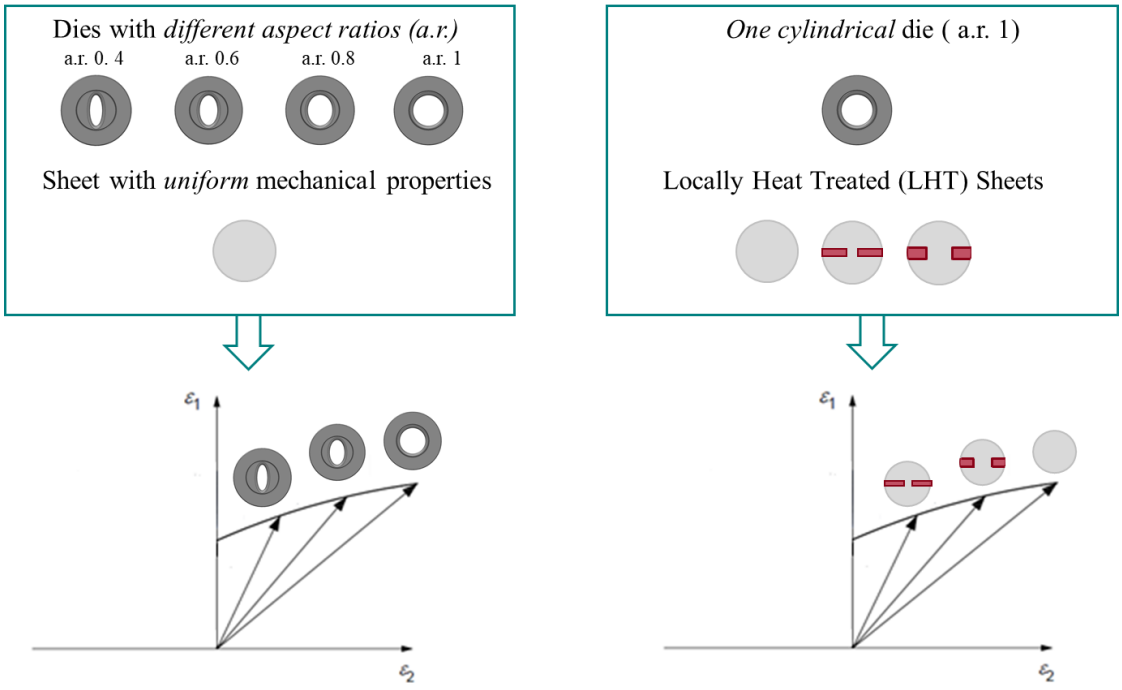

(a) (b)

Figure 3.9 (a) Conventional approach; (b) LHT approach

In the conventional approach, ratios of 0.8, 0.6 and 0.4 (corresponding to minor semi-axis values equal to 44 mm, 33 mm and 22 mm, respectively) were investigated by means of Finite Element (FE) simulations. Here the mechanical seals were positioned according to the different ratio changes. In the LHT approach, the heat treatments locally altering the material properties of the test samples were modelled partitioning the sheet (Figure 3.10a) and the material properties were assigned to each sub-region thanks to the adoption of a field variable. The

hardening behaviour of the as received (ASR) zone was taken from the bulge tests results, whereas the behaviour of the LHT annealed condition (AA5754-H111) was taken from data available in literature [96]. Figure 3.10b and Figure 3.10c show the flow curves and the Forming Limit Curves assigned to the base material (ASR) and the LHTed region. Between the as received and the annealed condition (LHT), a transition region having intermediate mechanical properties was modelled with an offset equal to 2.5 mm from the heat-treated zone to make the simulated distribution of properties close to what happens in real local laser heating. To assess the most suitable extent of the annealed zone, FE simulations were conducted to initially evaluate the effect of the three most influencing parameters, namely the length (L), the height (H) and the distance of the laser track from the center of the sheet (d) on the strain path at the dome.

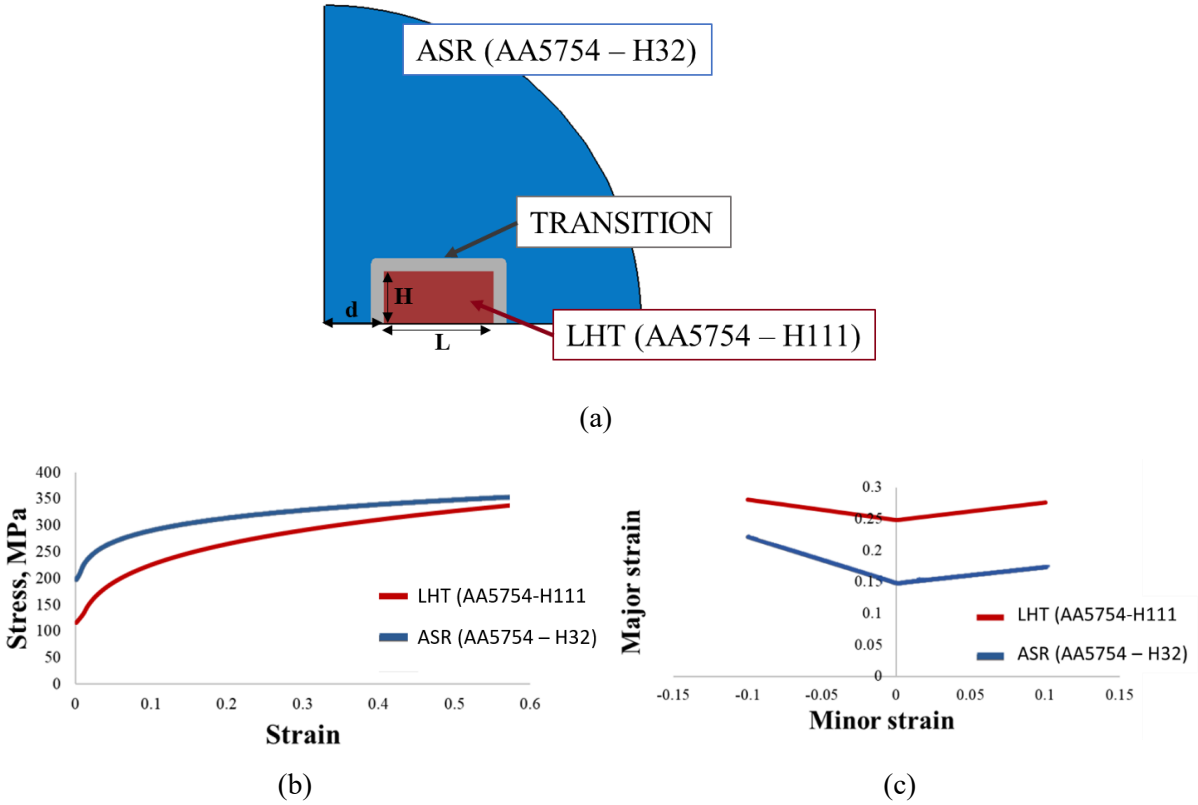

Figure 3.10 (a) Partitions of the test sample for the LHT sheets; d:distance of the laser track from the center of the sheet, L: length of the LHT region; H: height of the LHT region (b) Flow curves assigned to the ASR and LHT region (c) FLCs assigned the ASR and LHT region

The above mentioned parameters are shown in Figure 3.8 b. Thus, a Central-Composite Design (CCD) consisting of 15 runs was adopted for the FE simulations. Low and high level for parameters were 20/50 mm for L, 20/50 mm for H and 10/25 mm for d. Center points of the design were characterized by H= 15 mm, L= 35 mm and d= 15 mm whereas star points by H= 5/30 mm, L= 10/60 mm, d=5/30 mm. Further simulations were finally performed according to

the results from such DOE plan. Finally, the correlation between the laser heat treatment strategies and the die aperture ratios for obtaining a particular slope was found.

3.3 Rheological characterization of the MRFs

To model MRFs behaviour for sheet metal forming applications, two different approaches were evaluated. The first was based on the methodology proposed by Wang et al. [23,26] and it consisted of the combination of extrusion tests and FE simulation; in particular, to define the MRF properties for different magnetic field intensities, first appropriate values of the Young's modulus and yield stress were identified for different magnetic flux densities and piston velocities (i.e. strain rates). In both cases the optimal values were chosen on the basis of the minimisation of the difference between the value of extrusion force recorded experimentally and the one obtained from the FE simulations. The second proposed methodology was based on an inverse analysis approach using data from bulge tests performed adopting the MRF as forming medium. Bulge tests were conducted on sheets having known properties using an equipment with a solenoid to generate the magnetic field, which was specifically designed and manufactured. The pressure rate and the magnetic flux density were varied according to a Design of Experiments (DoE) while the strain experienced by the sheet material was acquired by means of a Digital Image Correlation (DIC) system to compare it with the numerical one. The two methodologies are discussed in detail in the following subsections.

3.3.1 MRF characterization by means of Extrusion tests

3.3.1.1 Extrusion tests - FE Model

Figure 3.11 shows the FE model (Abaqus/Explicit) of the Extrusion test (on the basis of the Wang et al. works [23,26]) for characterizing the MRF. To reduce computational costs, a 2d axisymmetric model was adopted. The piston and the cavity were modelled as analytical rigid bodies whereas the MRF as a deformable body. In **Figure 3.11**a the main components and dimensions of the model are summarized; they were taken from literature [23,26], as well as the fluid properties and the experimental results to validate the FE model. During the simulations, the piston moved upward within the cavity at different velocities. The piston lenght is slightly larger than the length of the cavity to avoid numerical problems related to edge effects. The MRF was modelled so that, in the initial condition, it filled the entire cavity except for the upper cylindrical part. The fluid was modeled as an elastic-perfectly plastic material.

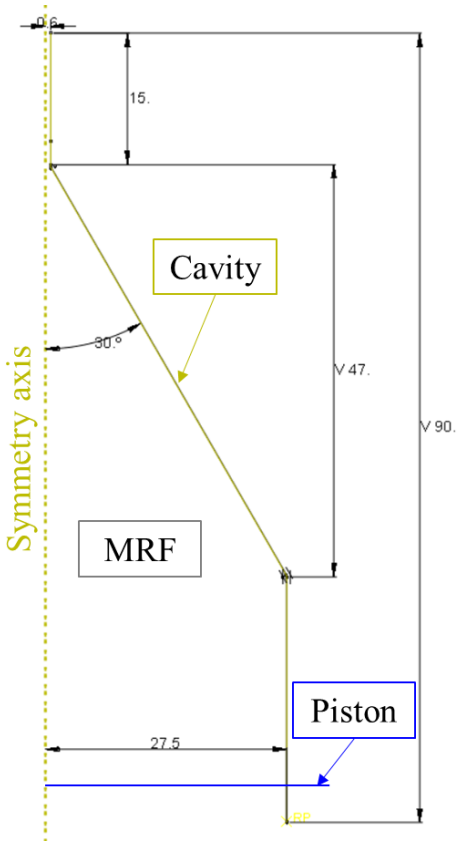

Figure 3.11 FE Model of the Cavity for the simulation of the MRF Extrusion Tests (dimensions: mm)

The mesh of MRF is shown in **Figure 3.12**. Since the deformation of the elements that occurs in extrusion problems is very high, especially in the cylindrical upper part of the cavity, an adaptive meshing (ALE) was used [97] to allow a better mesh quality by avoiding or limiting element distortions and thus convergence problems. However, adaptive meshing does not alter the topology (elements and connectivity) of the mesh, which implies some limitations on the ability to maintain a high-quality mesh under extreme deformation. Thus, the MRF was partitioned into more regular shaped sub-regions, which were therefore easier to discretise. The truncated-conical region was first sub-divided from the lower cylindrical region and it was partitioned according to the path that the fluid would have followed during the extrusion process (**Figure 3.12**a). Then, the MRF was meshed with 445 CAX4R (4-node axisymmetric bilinear quadrilaterals with reduced integration and hourglass control) elements. To find the optimal elements' size which allowed to obtain accurate results with low simulation time, an iterative procedure was conducted. **Figure 3.12**b shows the final mesh.

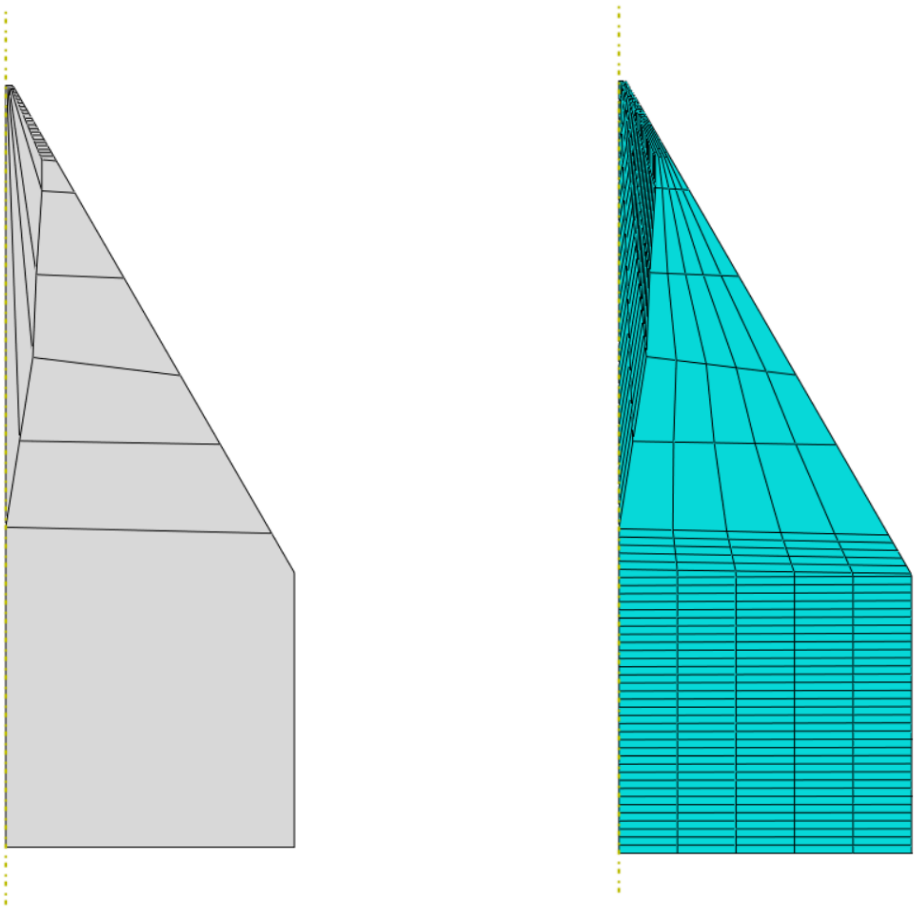

(a) (b)

Figure 3.12 (a) Partition of the MRF; (b) Mesh of the MRF

To determine the mechanical properties for each combination of magnetic field and piston speed, an approach based on a structured plan of simulations was used. This approach supported the identification of the optimal values of the parameters defining the elasto-plastic behavior of the MRF, namely Young's modulus (E) and Yield Stress (σ_y), whereas the Poisson's ratio (ν) was set at 0.25, being this value generally associated with clays. This choice represents a boundary condition and it was due to the fact that MRF gradually assumes, as the intensity of the magnetic field increases, a semi-solid behavior. For the adaptive mesh tool (ALE), the frequency of execution was set to 10 increments (default value), whereas the number of mesh sweeps to be performed in each adaptive mesh increment was set equal to 5 (slightly larger than the default value which is equal to 1). As output variables (i) the Extrusion Force F', namely the vertical component (RF2) of the reaction force on the Piston, (ii) Von Mises stress (S, MPa) and (iii) the Equivalent Plastic Strain (PEEQ) were considered.

3.3.1.2 Extrusion tests – Iterative procedure for determine the plastic properties

Figure 3.13 shows the procedure adopted for the determination of the MRF properties. It is divided in two steps, the first aimed at determining the MRF's elastic and the second the plastic properties.

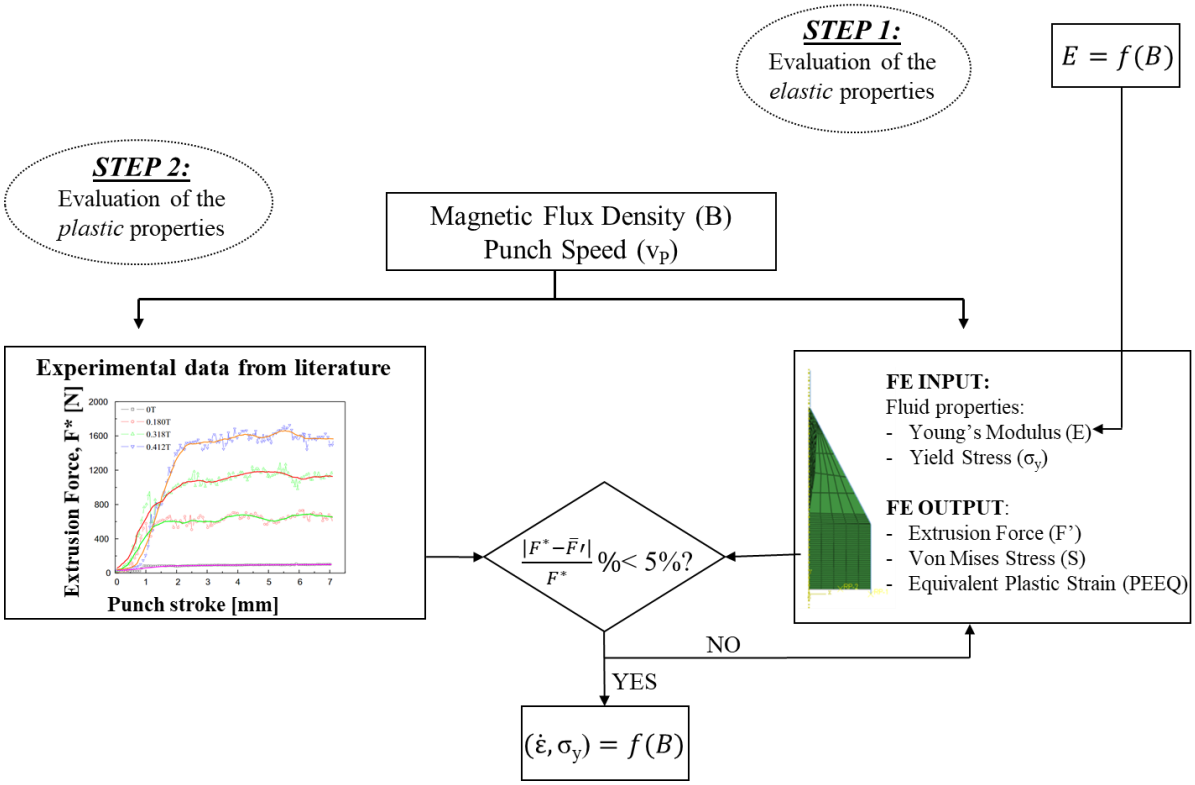

Figure 3.13 Iterative procedure to determine MRF properties

In particular, the first part led to the calibration of the elastic modulus E. Thus, for the first step, σ_y and the piston velocity were kept constant (at 0.02 MPa and 1.6 mm/s respectively), whereas the values of E were varied using values within the range reported in literature for an MRF having similar characteristics [28] and they are summarized in **Table 3.3**. The friction coefficient between the MRF and the cavity was set equal to 0.07 for B = 0 T, 0.12 for B = 0.180 T and 0.15 for B = 0.318 T [23].

B [T]	Elastic Properties	
	E [MPa]	ν
0	1 – 1.5	0.25
0.180	1.2 – 1.5	0.25
0.318	3 - 3.6	0.25

Table 3.3 Elastic properties of MRF assumed for the FE simulations of the extrusion tests at different magnetic flux densities

Then, the plastic properties of the MRF (Step 2 in **Figure 3.13**) according to magnetic flux density (B) and piston velocity (v_p) were determined. To this aim, for each value of B and v_p, several simulations were done by iteratively changing only the σ_y value, being the Young's Modulus constant for each magnetic field (whose values were previously determined in Step 1). The Extrusion Force values, F' (output variable of the FE simulations) were then compared to the experimental Extrusion Force ones, F* (taken from literature [23]). It is worth mentioning that the evolution of the Extrusion Force with the punch stroke (see **Figure 3.14**) was characterized by an almost linearly rising force at the beginning up to a peak and then it became almost constant while the MRF was overflowing out of the upper cylindrical part.

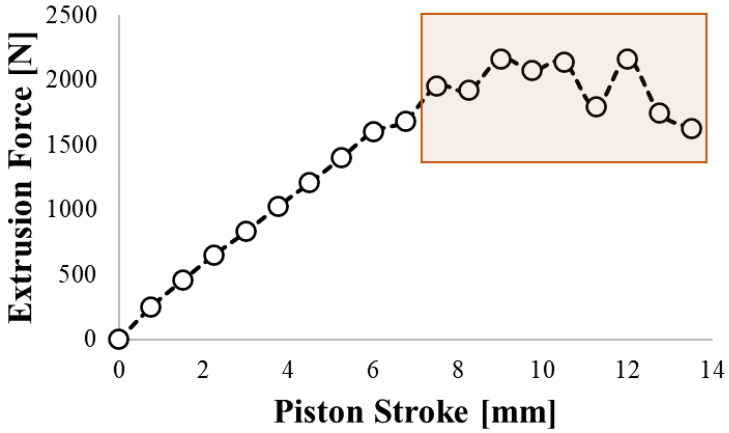

Figure 3.14 Force trend during extrusion tests

Thus, to make a comparison, the average Extrusion Force values after the stabilization (values highlighted inside the orange box in **Figure 3.14**) were considered. The iteration process was stopped when the relative error between F' and F* was less than 5%. Once the stable condition was reached, the equivalent plastic strain (PEEQ) and strain rate value (PEEQR) were calculated at a specific point located outside the extrusion die (Point A in **Figure 3.15**) using Eq. 19. The calculated PEEQR was then correlated to the σ_y value set for the specific piston velocity:

$$PEEQR = \frac{PEEQ(t_2) - PEEQ(t_1)}{t_2 - t_1} \tag{19}$$

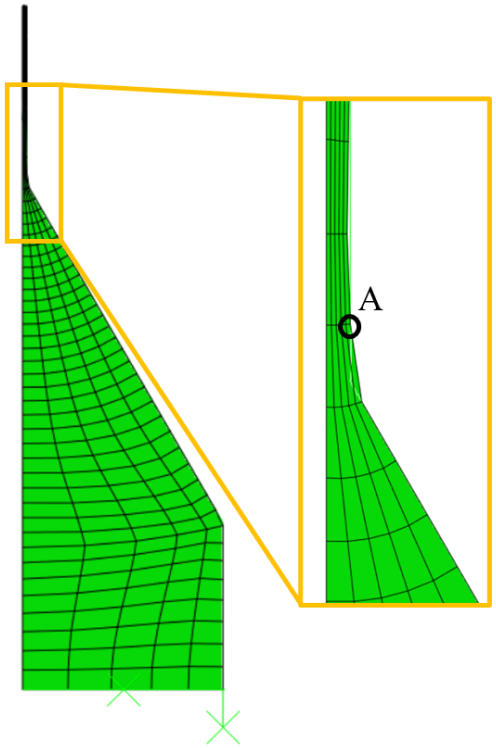

Figure 3.15 Location of the point (A) for the evaluation of the PEEQR

This procedure was adopted for each of the investigated piston velocity values and magnetic flux densities. After the identification of the values of the elastic and plastic properties of the MRF for each value of B and v_P, additional simulations were conducted for validation purposed. First, the stress values as a function of the strain rate were obtained by collecting the results from the described procedure. Secondly, FE simulations of the MRF extrusion process were conducted assigning a strain rate dependent material model to the MRF instead of the perfectly plastic behaviour used in the previous model. Furthermore, only the piston velocity was varied in the FE model and the extrusion force was monitored. Finally, the experimental and numerical forces were then again compared.

3.3.2 MRF Characterization by means of Bulge tests

3.3.2.1 The investigated MRF

An alternative route to material characterisation was also investigated that is different to that described so far, this was based on hydraulic bulge testing. The attention was thus focused on a hydrocarbon oil-based MRF (MRHCCS4-A, supplied by Liquid Research Limited) with a packing fraction by weight of 70%. In Figure 3.16 the physical properties (a), (b) the Shear Stress vs. Shear Rate curves at zero field for various temperatures and (c) the magnetic

induction (B-H) curve (which represents the magnetic flux density, B, as a function of the magnetic field strength, H) of the MRF are shown.

Property	Value
Operating Temperature	-40 [°C] to 140 [°C]
Density	2.49 [g/cc]
Colour	Grey
Flash Point	>190 [°C]

(a)

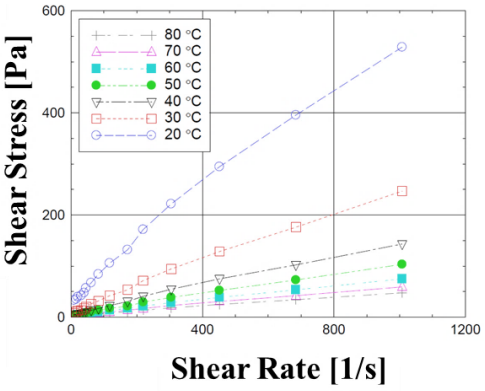

(b)

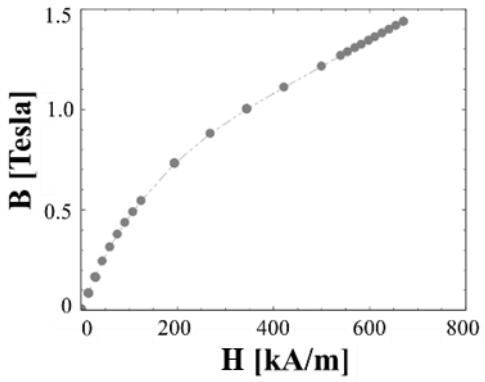

(c)

Figure 3.16 (a) Physical properties (b) Shear stress vs. shear rate curves at zero field for various temperatures and (c) B-H curve of the MRF MRHCCS4-A

3.3.2.2 Design of the MRF characterization equipment

To design the equipment for conducting the experimental bulge tests for the MRF characterization, two different sub-systems must be distinguished, the mechanical and the electromagnetic systems. Figure 3.17 shows a schematic of the mechanical components and the monitoring system, whereas **Figure 3.18** shows the main components of the manufactured set-up.

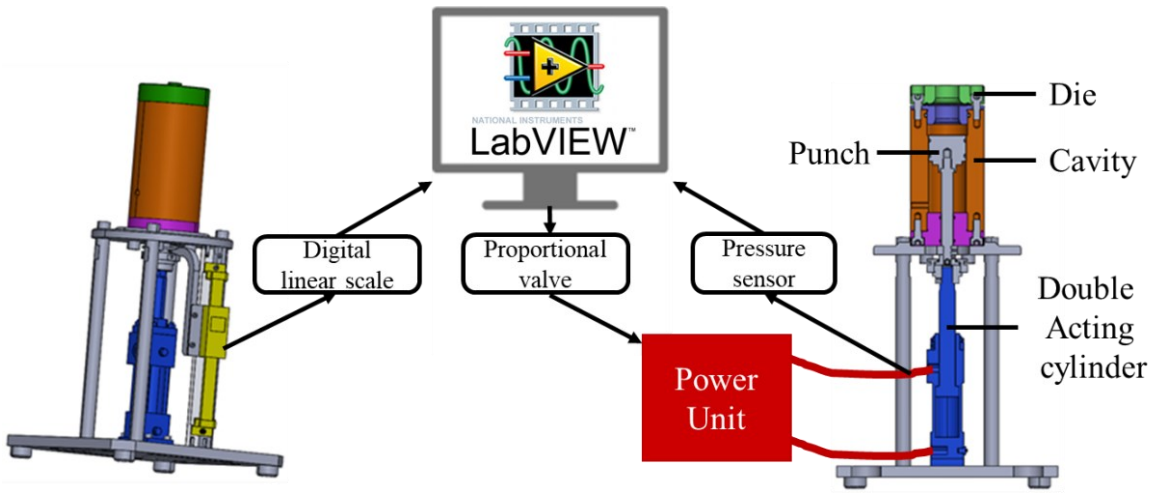

Figure 3.17 Schematic of the designed mechanical components and monitoring system for the MRF characterization

AISI316 was chosen as material for the die, the punch and the cavity (to be filled with the MRF) to ensure the magnetic induction lines got properly across the MRF. The punch is connected to a double acting cylinder, which is moved by a hydraulic power unit, controlled by a proportional valve via the LabVIEW software. The digital linear scale acquires continuously the punch displacement and it is connected to the LabVIEW software, whereas a pressure sensor is placed close to the oil inlet of the double cylinder to acquire the oil pressure.

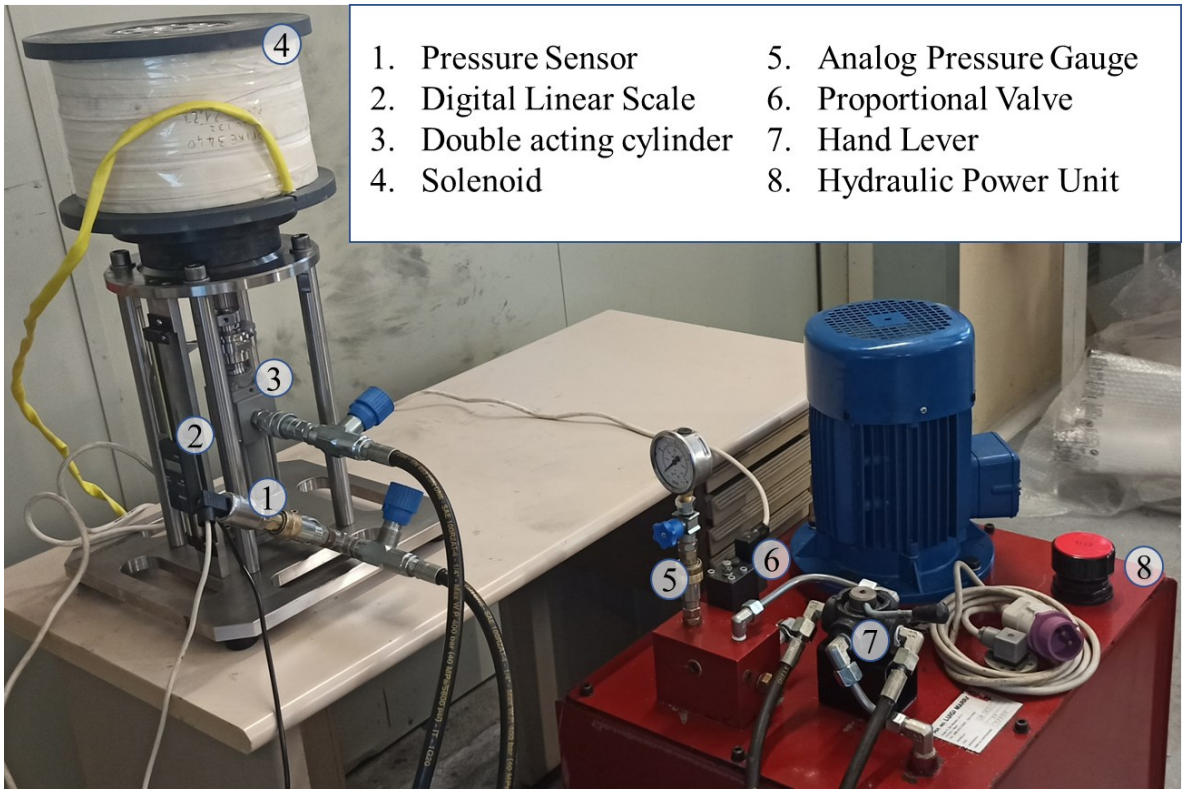

Figure 3.18 Main components of the designed experimental set-up

To avoid MRF leakage, both the cavity and the punch were equipped with O-rings (2 for the punch and 1 for the cavity, as shown in Figure 3.19).

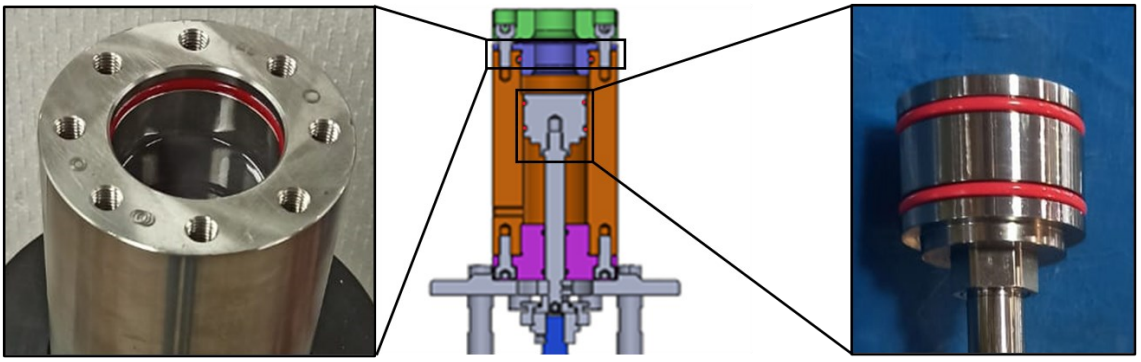

Figure 3.19 Positioning of the o-rings inside the cavity and outside the punch

Regarding the electromagnetic system, the solenoid was designed to generate a constant magnetic field in a sufficiently wide area of the MRF. The geometrical parameters which define a solenoid are shown in Figure 3.20a; they are the wire diameter (Φ_f), the inner diameter (Φ_i), the external diameter (Φ_e), the coils width (W) and the solenoid height, H_s. In this case, H_s (160 mm) and Φ_i (100 mm) represent geometrical constraints given by the mechanical parts' geometry, corresponding to the height and the external diameter of the cavity in Figure 3.17. Figure 3.20b shows the solenoid equivalent RL circuit [98].

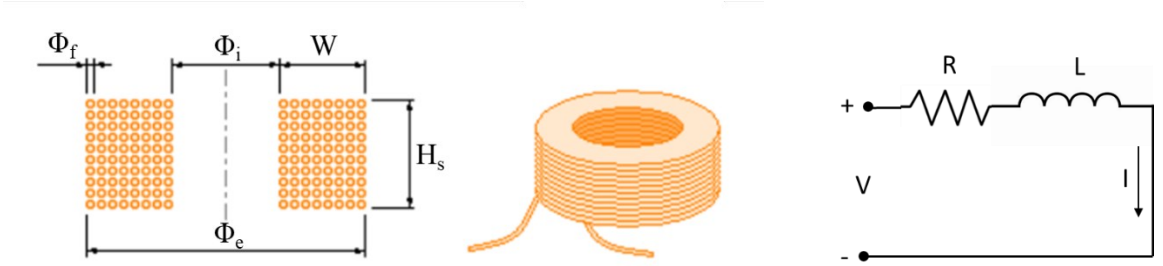

(a) (b)

Figure 3.20 Parameters for the solenoid design

When working in Direct Current (DC), the application of Kirchhoff's Voltage law to the Figure 3.20b gives Eq. 20:

$$V = R \cdot I \tag{20}$$

Where V is the DC source voltage, R is the resistance represented by the solenoid and I is the current intensity.

The starting point of the design was the calculation of the amper-turns ($N \cdot I$) necessary to achieve the desired value of magnetic flux density (B), that, according to the literature [23], had to be equal to 0.2 T. From the Ampère's law, the amper-turns for obtaining the target magnetic flux density were calculated (Eq. 21):

$$N \cdot I = \frac{B \cdot H}{\mu} = 25465\ Aturns \tag{21}$$

Where N is the number of turns of the multi-turn coil and μ is the vacuum permeability, which is a constant value equal to 1.2564E-06 H/m.

The electromagnetic problem was numerically simulated using the AC/DC module of the Comsol Multiphysics software. Figure 3.21 shows the 2d axisymmetric model adopted in presence of magnetic field (Figure 3.21b) and without it (Figure 3.21a). In the first case, the B-H curve shown in Figure 3.16b was implemented within the FE model.

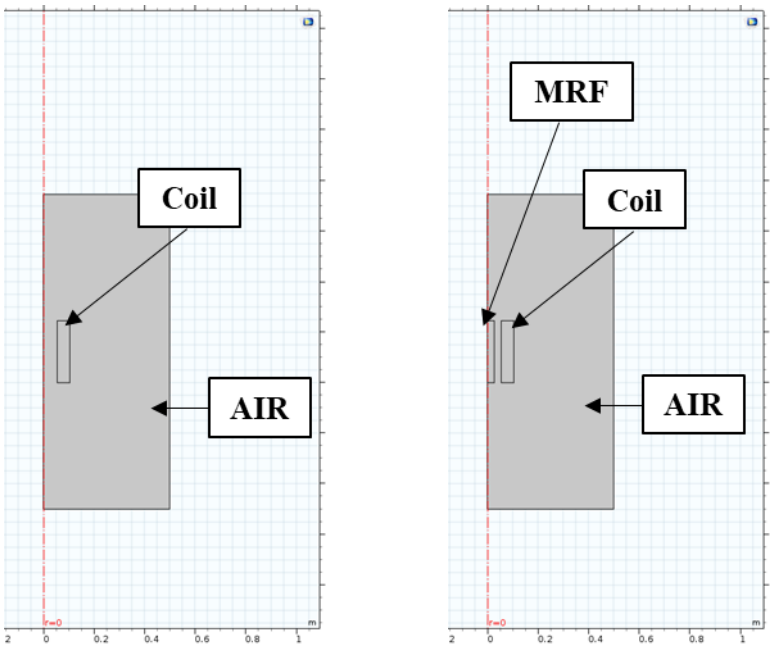

(a) (b)

Figure 3.21 Comsol FE model for the evaluation of the magnetic flux density

Different combinations of number of turns (N) and current intensity (I) were set in the simulations keeping constant their product (NI), as shown in Table 3.4 to evaluate the resulting magnetic flux density. The maximum value of the current intensity (3 A) was due to the maximum current that the power unit could manage.

N	I [A]
50930	0.5
25465	1
12732	2
8488	3

Table 3.4 Combination of number of turns (N) and current intensity (I) simulated with COMSOL software

To choose the enameled copper wire diameter, it is worth considering that the maximum current density, J, must be limited to 2.5 A/mm^2 to prevent the conductor from melting or burning, the insulating material failing, or the desired electrical properties changing. Thus, the current density was defined form Eq. 22 (where I_{max} is the maximum current intensity and Φ_f is the copper wire diameter), a proper copper wire diameter of 1.32 mm was chosen from that commercially available, which could withstand a maximum current intensity of 3.42 A.

$$J = \frac{I_{max}}{\pi \cdot {\Phi_f}^2 / 4} \tag{22}$$

To determine the solenoid width (W in Figure 3.20a), the coil packing factor (k) should be considered, which is the ratio of total conduction area of the winding and coil cross section window area and it is given by Eq 23:

$$k = \frac{S \cdot N}{W \cdot H} \tag{23}$$

$$S = \pi \cdot \left(\Phi_f / 2\right)^2 \tag{24}$$

Where N is the number of turns of coil, S is the cross-sectional area of the copper wire (given by Eq. 24), W is the solenoid width and H is the solenoid height. This value may range from 0.2 to 0.9 but it is commonly set as 0.7.

The approximate length of wire needed for winding can be calculated by Eq. 25 and it can be used for determining the solenoid weight.

$$l = \pi \frac{W \cdot (\Phi_e^2 - \Phi_i^2)}{{\Phi_f}^2} \tag{25}$$

The final manufactured coil is shown in Figure 3.22a: limitations coming from the maximum weight that could be applied on the upper plate of the equipment (the one bolted to the cavity) led to the final winding geometry characterized by 3440 turns and a final weight of 21.27 kg. The other main geometrical characteristics are shown in Figure 3.22b.

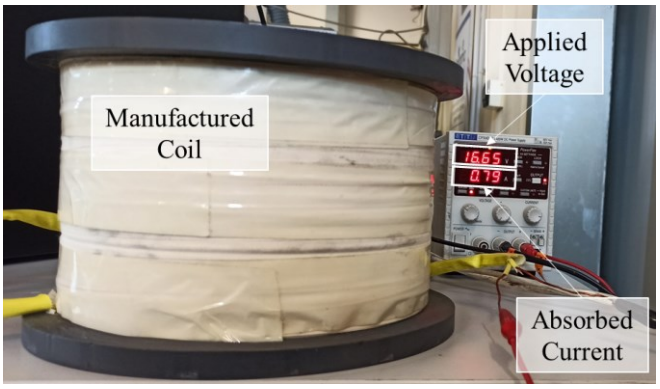

(a)

Internal Diameter, Φ_i	130 mm
External Diameter, Φ_e	250 mm
Number of turns, N	3440
Wire diameter, Φ_f	1.32 mm
Height, H	160 mm
Width, W	60 mm

(b)

Figure 3.22 (a) Manufactured coil (b) Main geometrical characteristics of the manufactured coil

The actual packing factor, k, was calculated using Eq. 23 and 24 and it was equal to 0.5. To evaluate the actual coil resistance, the coil was connected to the power source and the applied voltage increased from 0 V to 60 V while acquiring the absorbed current (Figure 3.22a). Then, Eq. 20 was used and the resulting coil resistance was 21 Ω.

The calculated actual coil's parameters were then implemented in FE Simulations (using Comsol Multiphysics software) to evaluate the resulting magnetic field distribution into the solenoid when changing the current flowing through it from 0 to the maximum value (I= 3 A), both in absence of MRF in the cavity (Figure 3.23a) and when the cavity was filled with MRF (Figure 3.23b). It can be seen that in both cases the magnetic field distribution was uniform in a sufficiently wide region within the cavity.

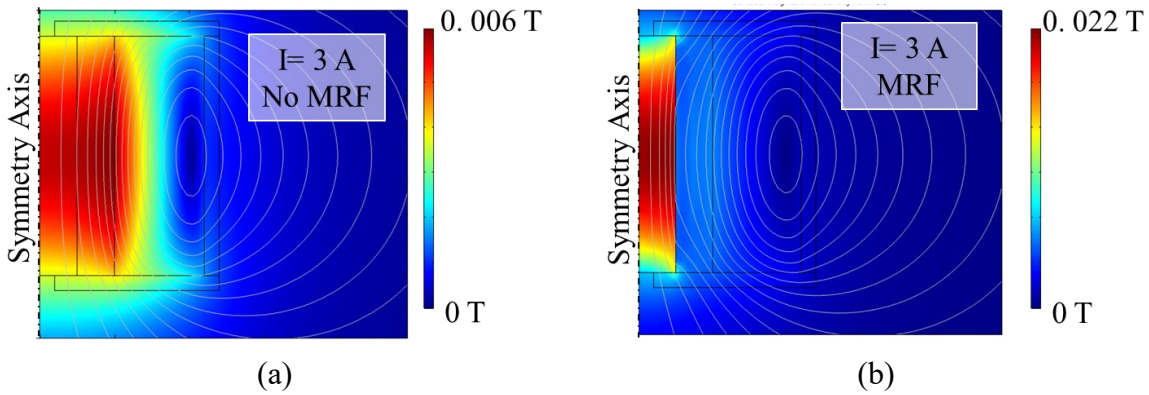

(a) (b)

Figure 3.23 Magnetic field distribution within the solenoid when a current of 3 A is flowing (a) in absence of magnetic field (b) when the cavity is filled with MRF

The numerical results were validated by measuring the maximum value of magnetic flux density within the cavity (without MRF) by means of a Gauss Meter.

3.3.2.3 Experimental bulge tests using MRF

Experimental bulge tests were carried out on the equipment discussed in the previous section and initially shown in Figure 3.17. Figure 3.24 shows in details the main components. First, the cavity was filled with 100 ml of MRF, the blank was placed between the cavity and the die, then serrated to prevent any blank drawing.

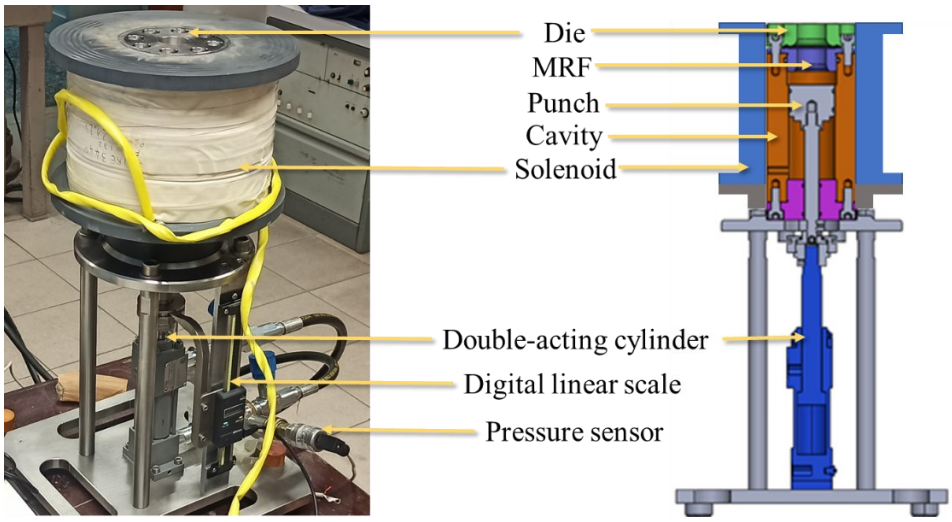

Figure 3.24 Equipment for the bulge tests using MRF as forming medium.

The inner diameter of the cavity and fillet radius of the die are 50 mm and 8 mm, respectively. The pressurized oil was introduced into the double-acting cylinder (connected to the punch), the MRF was compressed, and, in turn, it transferred the loading pressure on the sheet. As previously described, the oil pressure was controlled by a proportional valve connected to a hydraulic power unit and acquired by a pressure sensor, while the punch displacement was acquired by a linear digital scale. The solenoid combined with the DC power supply was used to generate a maximum magnetic flux density of 3.8 mT, using an input current of 2.6 A.

The proportional valve, the pressure sensor and the digital linear scale were controlled by a LabVIEW program and the virtual control panel is shown in Figure 3.25. After each test, the full-field distribution of strains was acquired by means of a Digital Image Correlation (DIC) system (ARAMIS, GOM), whereas the dome height was acquired by means of a height gauge. A three-level full factorial design with two factors was considered as experimental plan. In particular, the oil pressure rate, p_{rate} (0.5 – 2 –5 bar/s) and the applied magnetic flux density, B (0 – 1.8 – 3.8 mT) were considered as input parameters.

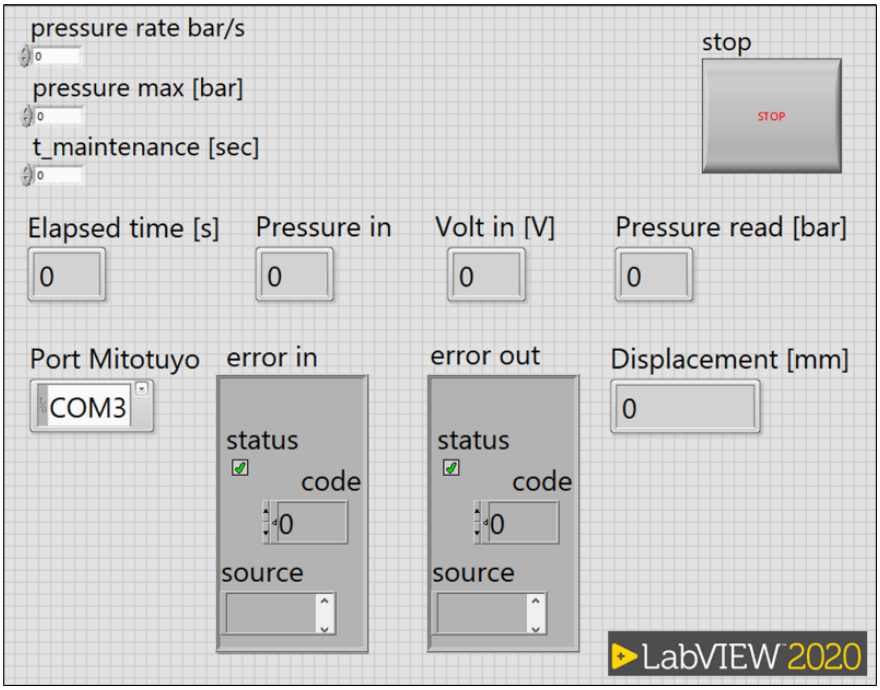

Figure 3.25 Front panel for the control of the test by means of LabVIEW

Once the oil pressure reached 250 bar, it was held for 40 seconds and then the test was stopped. Among the tests, results from those carried out at a pressure rate of 0.5 bar/s and 5 bar/s were used to determine the MRF properties by means of an inverse analysis approach. The remaining conditions, those characterized by a pressure rate of 2 bar/s, were used for validation purposes.

3.3.2.4 FE model for the bulge tests using MRF

Bulge tests were simulated using the commercial software ABAQUS/Explicit. To reduce the computational time, an axisymmetric FE model was used, as shown in Figure 3.26a. The sheet and the MRF were modelled as deformable bodies: the former was meshed with 250 CAX4R (4-node axisymmetric bilinear quadrilaterals with reduced integration and hourglass control) elements, whereas the latter with 2550 and progressively reducing the average size of the element in the proximity of the contact with the blank, as shown in Figure 3.26b. Furthermore, to avoid excessive distortions of the MRF elements, an adaptive mesh with a frequency of 10 increments with 5 remeshing sweeps per increment was set (similarly to what was done for the simulation of the MRF extrusion tests). At first, the loading conditions regarding the two pressure rates of 0.5 and 5 bar/s were simulated. Simulations were performed assigning to the punch the speed resulting from the experimental tests. Values of the Young's Modulus, *E,* and Poisson's ratio, *ν,* were varied according to a full factorial DoE with 3 levels (1- 5 -15 MPa and 0.35 – 0.4 – 0.49 for E and ν respectively). The final values of the dome height and the major strain were collected as numerical outputs to be compared with the experimental ones.

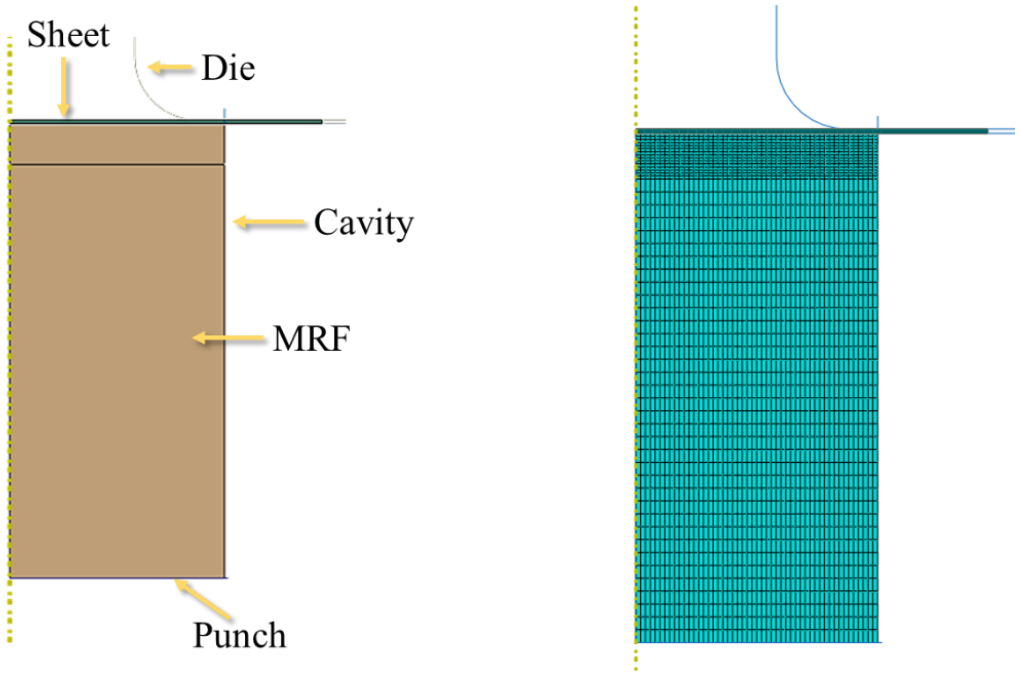

(a) (b)

Figure 3.26 (a) Scheme of the FE model (b) Mesh of the MRF

3.3.2.5 Inverse analysis procedure

The inverse analysis approach was treated as an optimization problem, where the final aim was to minimise the error function that quantifies the discrepancy between the numerical data and

those acquired through experiments. The proposed methodology, schematically depicted in Figure 3.27, was applied to calibrate the rheological parameters in each of the investigated levels of the magnetic flux density, B, and pressure rate, p_{rate} (as described in the previous section).

Results from numerical simulations were collected in terms of final Bulge Height (h) and maximum plastic strain (ε) that were, in turn, used to calculate the error with the experimental data (strains from ARAMIS and bulge height from the linear gauge) according to Eq. 26 and Eq. 27.

$$Err_h = \frac{h_{exp} - h_{sim}}{h_{exp}} \tag{26}$$

$$Err_\varepsilon = \frac{\varepsilon_{exp} - \varepsilon_{sim}}{\varepsilon_{exp}} \tag{27}$$

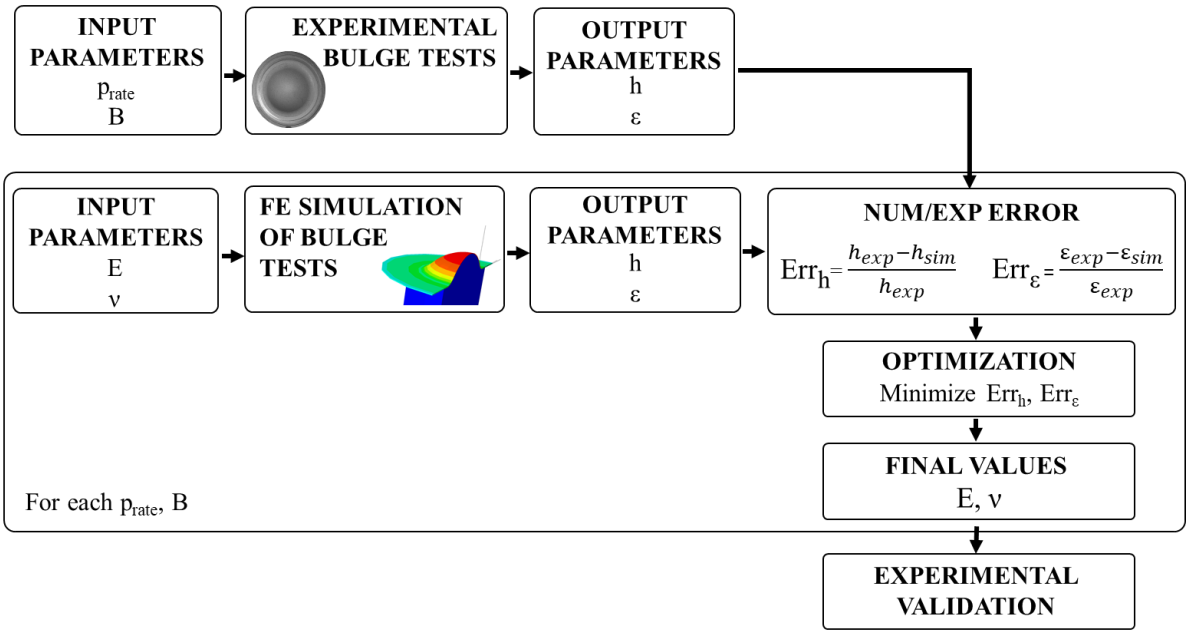

Figure 3.27 Methodology for the inverse analysis

The two error quantities were then set as the output variables; an accurate Response Surface (RS) was trained on each error parameter by choosing the most accurate interpolating algorithm among the five Radial Basis Functions available within the integration platform modeFRONTIER (Hardy's MultiQuadratics, Inverse MultiQuadratics, Gaussians, Duchon's Polyharmonic Splines, Wendland's Compactly Supported). The workflow used to create the metamodel is shown in Figure 3.28.

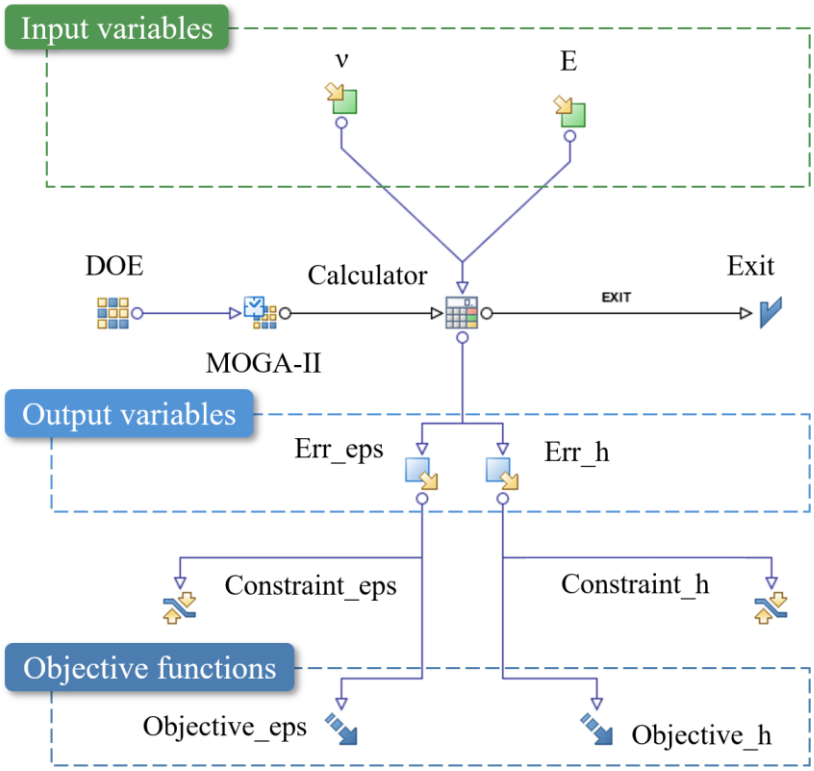

Figure 3.28 Overview of the modeFRONTIER workflow

The workflow shows the two objective functions (highlighted by the blue dashed box) connected to the two output variables: in such a way, the constructed RS could then be used as the starting point for a virtual optimization. The optimization round, managed by a multi-objective genetic algorithm (MOGA-II, an improved version of the MOGA algorithm), was based on 1000 successive generations, each composed of 9 individuals (as the initial DoE). At the end of the optimization round, optimal designs could be eventually evaluated: those designs were characterized by the optimal values of the defined input parameters (E and ν) able to minimize the two error functions. The optimization round was repeated for all the investigated operative conditions: in such a way, the two input parameters – i.e. elastic modulus and Poisson's ratio – could be expressed as a function of the magnetic flux densities and pressure rates. After the optimization procedure, an additional set of simulation was performed at an intermediate value of pressure rate (2 bar/sec) with the calibrated E and ν from the inverse analysis to validate the methodology.

4. Influence of the laser heat treatment on the AA5754-H32 strain path during hydraulic bulge tests

In this chapter, results from the new methodology for the determination of the right hand of the Forming Limit Curve (FLC), based on the adoption of local heat treatments aimed to induce different strain paths using a classical circular blank and die in a hydraulic bulge test apparatus are presented.

4.1 Numerical model validation

The numerical model for a standard bulge test was validated using data from experiments performed with a circular die. Figure 4.1a and Figure 4.1b show the equivalent plastic strain (PEEQ) distribution at failure obtained from the FE simulations and the GOM ARAMIS system acquisition, respectively. Figure 4.1c shows the numerical/experimental comparison of the dome height (h_d) evolution during the tests. In particular, the experimental dome height was obtained using the approach given by Panknin [110] as a function of the bulge radius (ρ) calculated by the GOM ARAMIS system (Eq. 30):

$$\rho = \frac{(R_f + R_d)^2 + h_d^2 - 2R_f h_d}{2h_d} \tag{30}$$

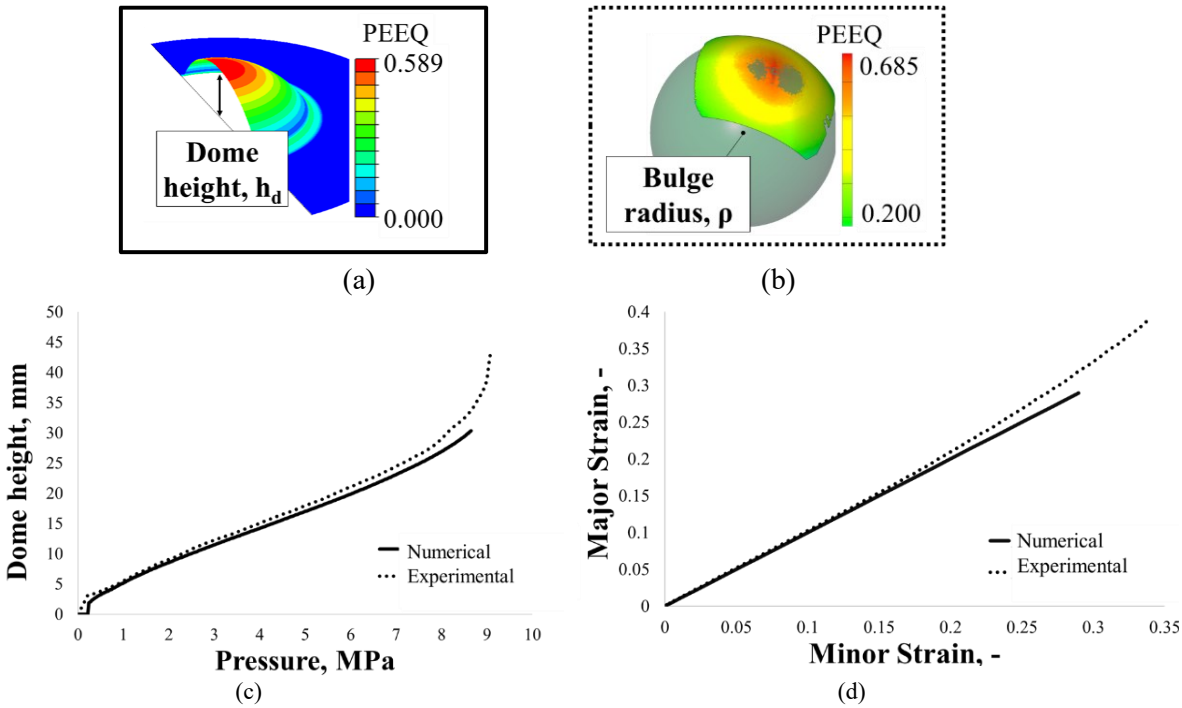

Figure 4.1 Results of circular bulge tests on ASR sheets: (a) Equivalent plastic strain (PEEQ) distribution at failure obtained from the FE simulations (b) Equivalent plastic strain (PEEQ) distribution at failure acquired by the GOM ARAMIS system (c) Numerical and experimental dome height vs pressure; (d) Numerical and experimental strain paths of the dome.

In Figure 4.1d the strain path extracted at the dome from the simulation was plotted together with that acquired by the GOM ARAMIS DIC system. Both graphs show a good correlation between experimental and numerical data.

4.2 Laser heat treatment parameters investigations

As described in Section 3.2.2, heat treatments for locally altering the material properties of the test samples were modelled dividing the sheet in parts having different mechanical properties, namely one having the base material (AA5754-H32) and the other having the annealed material (AA5754-H111) hardening behaviour. To assess the most suitable extent of the annealed zone, FE simulations were conducted to initially evaluate the effect of the three most influencing parameters, namely the length (L), the height (H) and the distance of the laser track from the center of the sheet (d) on the strain path at the dome. Analysis of variance (ANOVA) was adopted to determine how the size (identified by the parameters H and L) and the position (defined by the parameter d) of the heat treated region affected the strain path at the dome. In particular, the slope of the strain path (Major strain/Minor strain) was considered as response variable. In Figure 4.2 the ANOVA table is presented: the test for significance of regression (p-value associated with the model) shows that the influence of the height (*H*) and the distance from the center (*d*) of the laser track significantly affected the slope of the strain path, as the p-value was lower than 0.05.

Source	DOF	Sum of square	Mean square	F-value	p-value
Model	9	8.314	0.924	22.66	0.002
Linear	3	5.616	1.872	45.92	0.000
H	**1**	**0.662**	**0.662**	**16.24**	**0.010**
L	1	0.161	0.161	3.95	0.104
d	**1**	**4.689**	**4.689**	**115.03**	**0.000**
Square	3	1.396	0.465	11.42	0.011
H*H	1	0.229	0.229	5.63	0.064
L*L	1	0.163	0.163	4.00	0.102
d*d	1	0.301	0.301	7.37	0.0042
2-way interaction	3	0.335	0.112	2.74	0.153
H*L	1	0.061	0.061	1.49	0.277
H*d	1	0.074	0.074	1.82	0.235
L*d	1	0.216	0.216	5.3	0.070
Error	5	0.204	0.041		
Total	14	8.518			
Model summary					
S	R-Sq	R-sq(adj)	R-sq(pred)		
0.202	97.61%	93.30%	72.45%		

Figure 4.2 Preliminary FE simulations results: ANOVA table for Response Surface Regression Analysis

The consideration from the ANOVA table was further confirmed by Main Effect Plot (Figure 4.3). Here, it can be observed that the slope of the strain path was mostly affected by the distance of the laser track from the center of the blank (*d*) and in particular the slope significantly increases when the distance (*d*) is decreased: thus, the narrower the non-heated region close to the dome, the closer the strain condition was to plane strain. Additionally, the slope was increased by an increment of the height of the laser track (H) from 5 mm to 15 mm, however when H reaches the value of 30 mm the slope increased slightly.

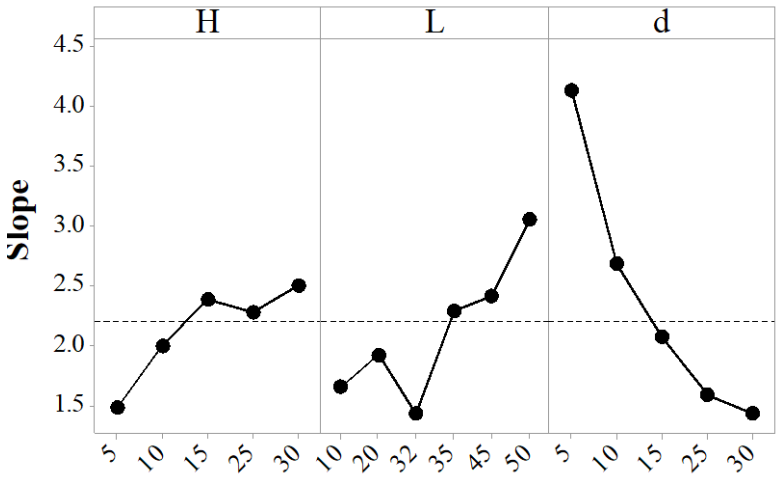

Figure 4.3 Preliminary FE simulations results: Main Effect Plot for the slope of the strain path of the dome

A hydraulic bulge test is considered to be valid when fracture occurs within 15 degrees of the top surface of the dome. Figure 4.4 shows the FLDCRT map resulting from the FE simulation of the bulge test conducted on blanks heat treated using two different set of parameters (H=20 mm, L=50 mm, d=10 mm in fig. 5a; H=15 mm, L= 10 mm, d=15 mm in Figure 4.4b).

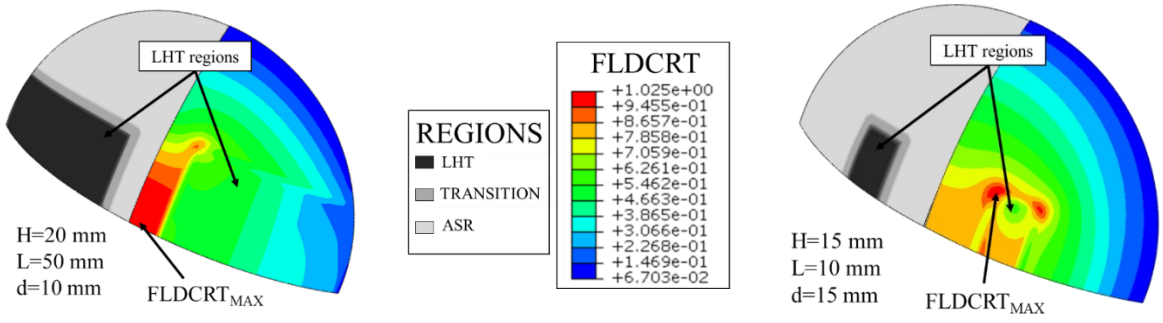

(a) (b)

Figure 4.4 Numerical FLDCRT maps for the LHT condition characterized by (a) H=20 mm, L=50 mm, d=10 mm (b) H015 mm, L= 10 mm, d=15 mm.

It can be noticed that when the heat treated region was sufficiently wide (Figure 4.4a), rupture occurred at the top of the dome area (the FLDCRT output variable overcame the

critical value in the centre before than in any other area); on the contrary, when the extent of the heat-treated portion was not enough wide, (as in Figure 4.4b), FE simulation results suggested that failure occurs far from the top of the dome area and, in particular, at the corner of the heated area.

4.3 Investigation about the strain path modification through the laser heat treatment

As explained in Section 3.2.2, the proposed methodology was aimed first at the correlation between the laser heat treatment strategies and the die aperture ratios for obtaining a particular slope. The possibility to alter the slope of the strain path at the dome by means of local laser heat treatments was investigated varying a large range of the parameter *d* (from 3 to 30 mm), that was considered the most influencing factor (as discussed in section 3.2). The height (H) was kept constant and equal to 5 mm whereas the length (L) was extended up to the outer diameter of the blank, to limit the occurrence of critical conditions as those shown in Figure 4.4b.

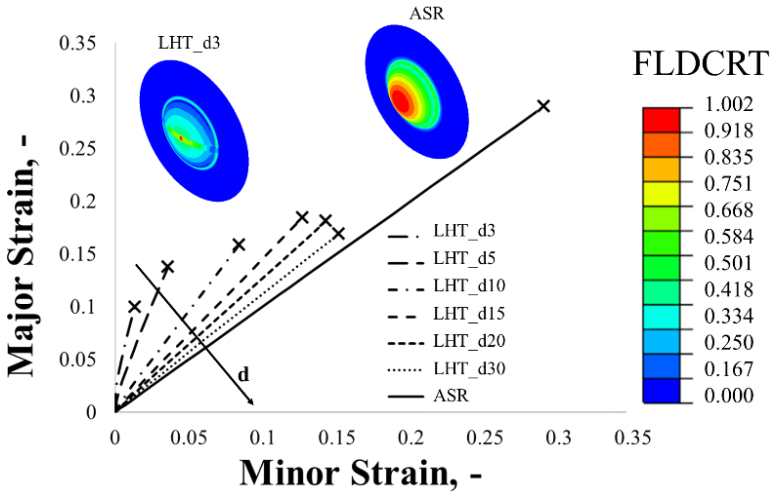

Figure 4.5 Numerical results in terms of strain paths and FLDCRT maps concerning the bulge tests conducted on heat treated samples

Figure 4.5 shows the strain paths at the dome of samples in AA5754-H32 which were laser heat treated before the bulge test using different values of the parameter d. In the same figure the FLDCRT maps of the untreated specimen in the as received (ASR) condition and a specimen characterised by the smallest value of the parameter d (3 mm, indicated by the label "*LHT_d3*") are shown. Results suggest that if the distance of the laser heat treated zone was decreased from the centre of the sheet, the slope of the strain path at the dome increased, moving closer to the plane strain condition, due to the constraining action exerted by the surrounding material (still

in the as-received H32 conditions). In addition, it can be observed that the rupture zone was always located in the centre.

Figure 4.6 shows the strain paths of the AA5754-H32 dome and the FLDCRT map of the sheets obtained from FE simulations by using the elliptical dies approach (i.e. the conventional approach). It can be observed that the strain ratio (Major Strain/Minor Strain) increases when the die aperture ratio (a.r.) decreases from 1 to 0.4.

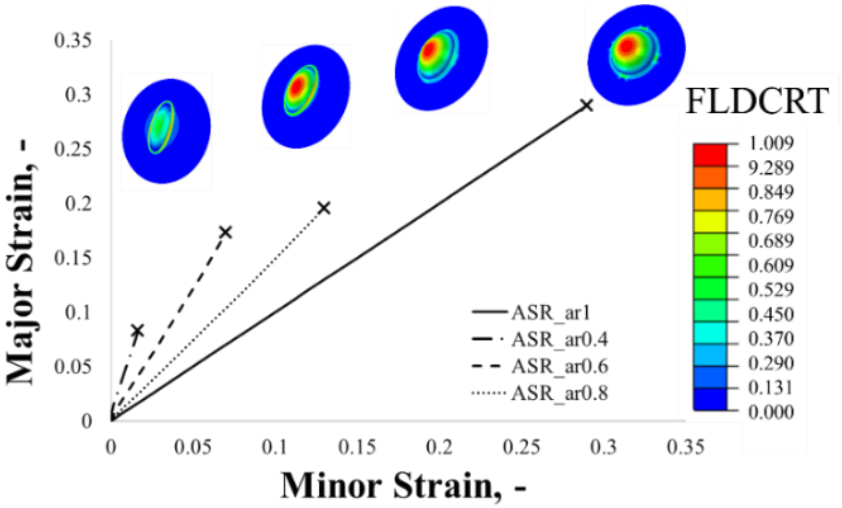

Figure 4.6 Results of the simulations with the conventional approach

It is worth noting in the elliptical aperture ratios of 0.4 and 0.6, the simulations predicted an edge failure instead of a failure located on the top of the dome. As reported in [111], in the case of elliptical bulge tests, the die size, the sheet thickness and the material forming properties affect the occurrence of the failure in the dome or on edge. The calculated slopes were eventually plotted as function of the main influencing factor, i.e. the aperture ratio for the conventional approach and the parameter *d* in the case of the innovative methodology (see Figure 4.7).

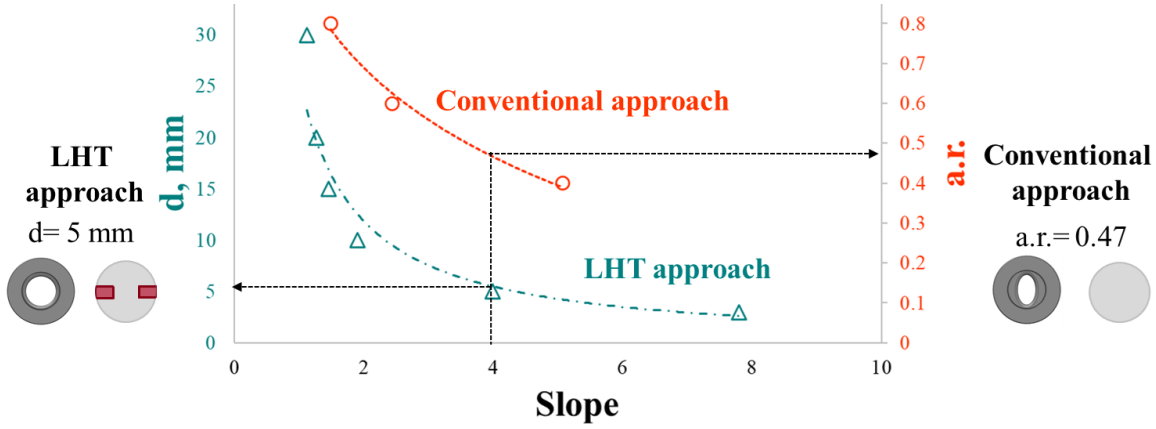

Figure 4.7 Correlation between the two approaches

As an example, the point of the FLC characterized by a slope of the strain path equal to 4 could be obtained with an elliptical die with a 0.47 aperture ratio (conventional approach) or by carrying out a local laser heat treatment characterised by a distance d from the center equal to 5 mm (new methodology).

As a consequence, the LHT approach was revealed to be more flexible and versatile since it is able to achieve several slopes in the strain path by only changing the heating strategy. On the other hand, the conventional approach required the manufacturing of a single die with a single aperture ratio to get a specific slope of the strain path. Nevertheless, it should be highlighted that the proposed methodology becomes effective when adopted on strain-hardenable Al alloys characterized by an initial pre-strained condition (as in the case of the AA5754, initially in the H32 state): in fact, the role of the laser heating is the reduction of the dislocation density, thus locally bringing the material to the fully annealed state. On the other hand, the proposed methodology can be easily extended to the heat treatable alloys (representing a broad range of alloys of industrial interest) in which the properties can be tailored and easily reverted by means of specific heat treatments.

5. Evaluation of the rheological behaviour of the MRF

In this chapter, results of the two different approaches used to model the MRFs behaviour, (1) based on the combination of extrusion tests and FE simulation and (2) based on an inverse analysis approach using data from bulge tests performed on the Al alloy adopting the MRF as a forming medium are presented.

5.1 MRF characterization by means of extrusion tests

To model MRFs behaviour for sheet metal forming applications, the first investigated approach reviewed was based on the methodology proposed by Wang et al. [23,26]; it consisted of the combination of extrusion tests and FE simulation; in particular, to define the MRF properties for different magnetic field intensities, first appropriate values of the Young's modulus and yield stress for different magnetic flux densities and piston velocities (i.e. strain rates) were identified. Then, the plastic properties of the MRF according to magnetic flux density, *B*, and piston velocity, v_p, were determined. In both cases the optimal values were chosen on the basis of minimising the difference between the value of extrusion force recorded experimentally and that obtained from the FE simulations. It is worth mentioning that in this case, experimental data were taken from literature [23,26]. In the following subsections, results obtained by means of this approach are presented.

5.1.1 Elastic properties of the MRF

Figure 5.1 shows the Numerical Extrusion Force according to time for the determination of MRF Young's Modulus in the case of B=0T (**Figure 5.1**a) B=0.180 T(**Figure 5.1**b) and B=0.318 T (**Figure 5.1**c). It can be noticed that for each magnetic flux density, results in terms of extrusion force were similar. Therefore, a value of E equal to 1 MPa was adopted for B=0 T, a value of 1.2 MPa for B=0.180 T and 3.6 MPa for B=0.318 T.

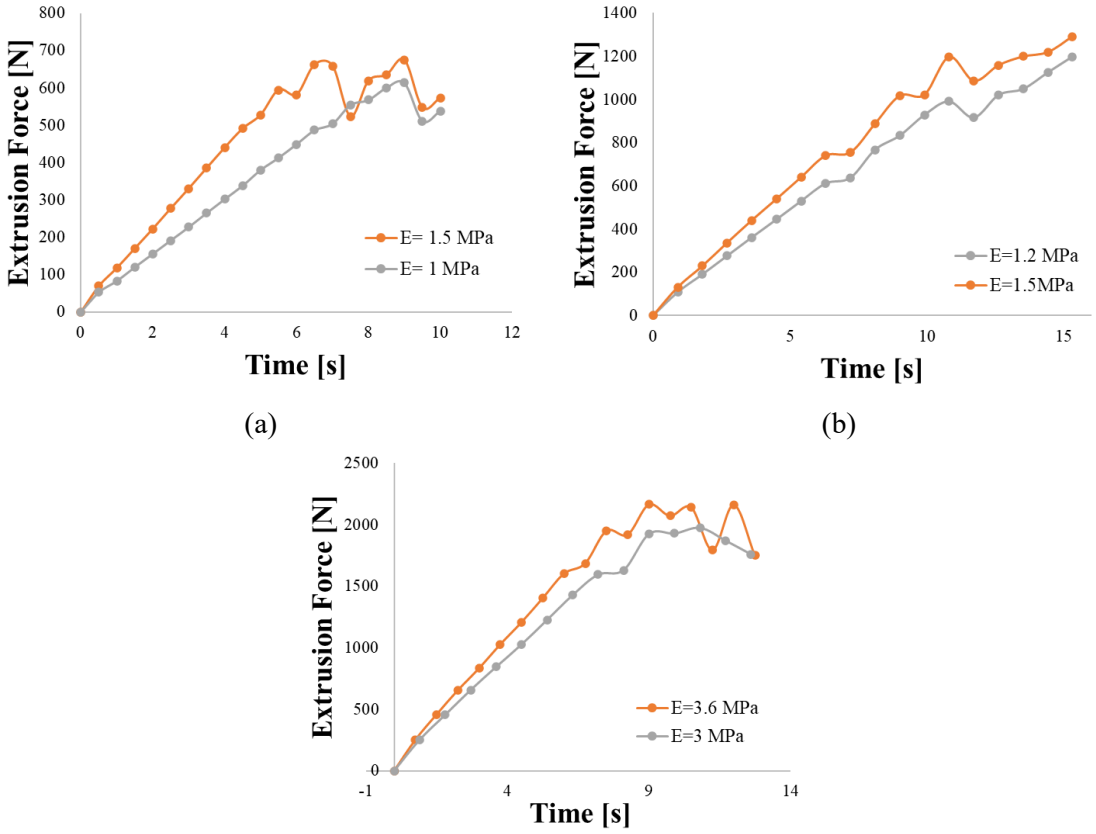

Figure 5.1 Numerical Extrusion Force vs. time for the determination of MRF Young's Modulus in the case of (a) B=0T (b) B=0.180 T and (c) B=0.318 T

5.1.2 Plastic properties of the MRF

The determination of the yield stress associated with each piston velocity and magnetic field was generated using the procedure described in section 3.3.1. **Figure 5.4** shows the evolutions of the extrusion force obtained for each combination (σ_y, v_p) of the input parameters. It can be observed that the minimum value of piston stroke for all the obtained force reached almost constant values was 7 mm.

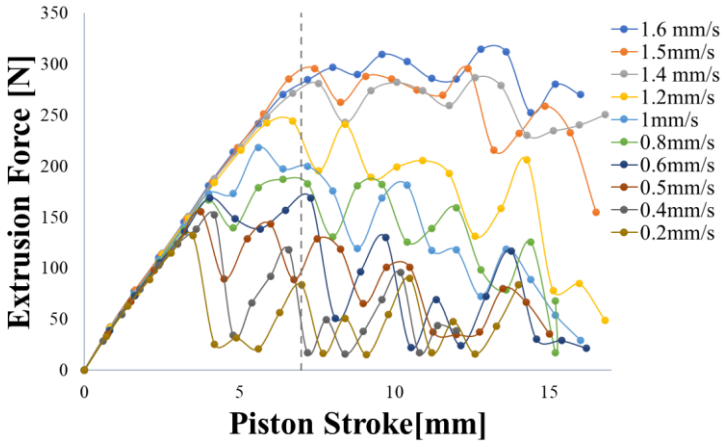

Figure 5.2 Numerical Extrusion Force at different various piston velocities for B=0 T

For this reason, the equivalent plastic strain rate (PEEQR) value of the node located outside the extrusion cylindrical die at a piston stroke of 7 mm was extracted (it is indicated as "$PEEQR_{S7}$" in **Figure 5.3**) and correlated with the yield stress (point A in **Figure 5.3**).

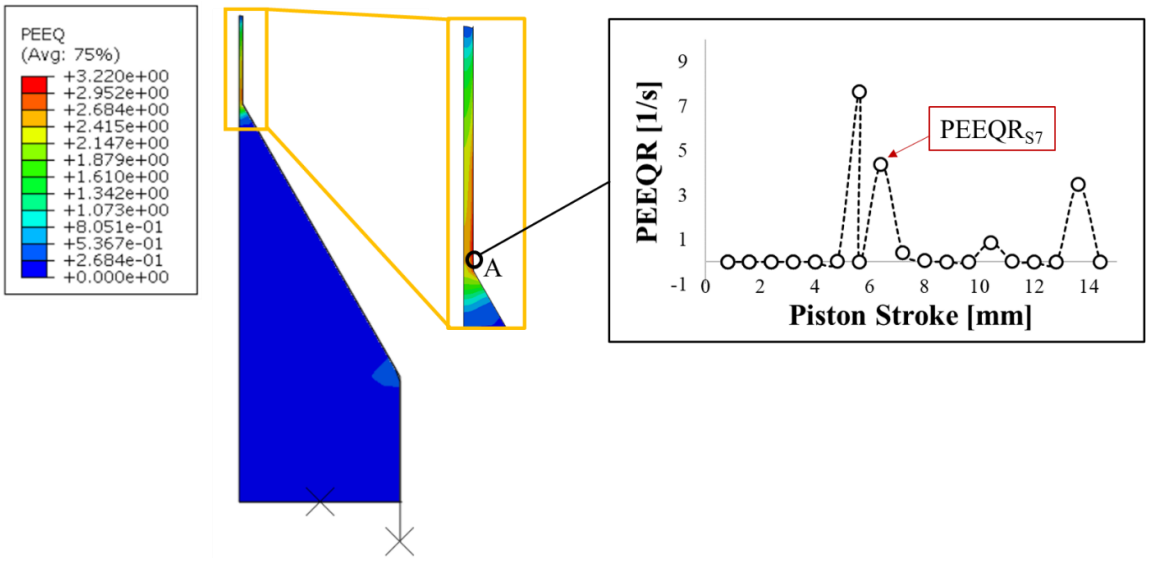

Figure 5.3 Equivalent plastic strain (PEEQ) map and equivalent plastic strain rate (PEEQR) of point A, for a piston velocity of 1.6 mm and B= 0T

Figure 5.4a shows the results in terms of yield stress that allowed to reduce the discrepancy between the numerical extrusion force value and the one experimentally acquired below 5%. In **Figure 5.4**b, the values of the yield stress (σ_y), the experimental force (F*), the numerical force (F') and their relative error $\left(\frac{|F^*-F'|}{F^*}\% \right)$ for each piston velocity (in absence of magnetic field, B = 0 T) were reported, as well as the equivalent strain rate value (PEEQR) at the monitored point (A in **Figure 5.3**).

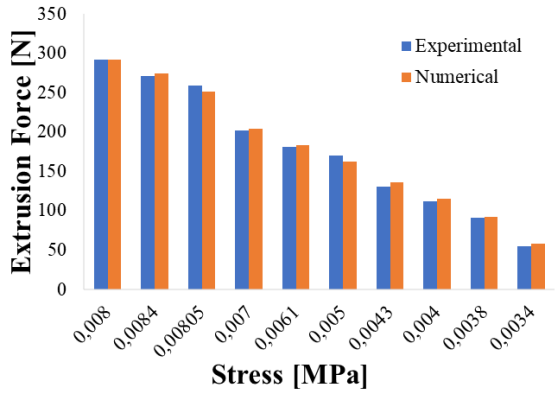

(a)

v_P [mm/s]	σ_y [MPa]	F' [N]	F* [N]	$\frac{\lvert F^*-F'\rvert}{F^*}\%$	$PEEQR_{S7}$
1,6	0,008	291,87	291,5	0,127	7,63
1,5	0,0084	270,89	274,6	1,351	7,47
1,4	0,00805	258,53	250,85	3,064	6,37
1,2	0,007	201,23	203,42	1,077	8,11
1	0,0061	181,18	183,05	1,022	7,94
0,8	0,005	169,76	162,7	4,339	5,89
0,6	0,0043	130	135,6	4,130	5,05
0,5	0,004	111,95	115,25	2,863	4,09
0,4	0,0038	91,08	91,52	0,481	3,27
0,2	0,0034	55	57,67	4,631	1,43

(b)

Figure 5.4 (a) Numerical- experimental comparison between extrusion forces obtained at certain yield stress values for a magnetic flux density of 0 T (b) Table of the input and output variables of the simulations and experimental tests (B=0 T)

Finally, Figure 5.5 shows the yield stress vs strain rate curve along with the power law fitted.

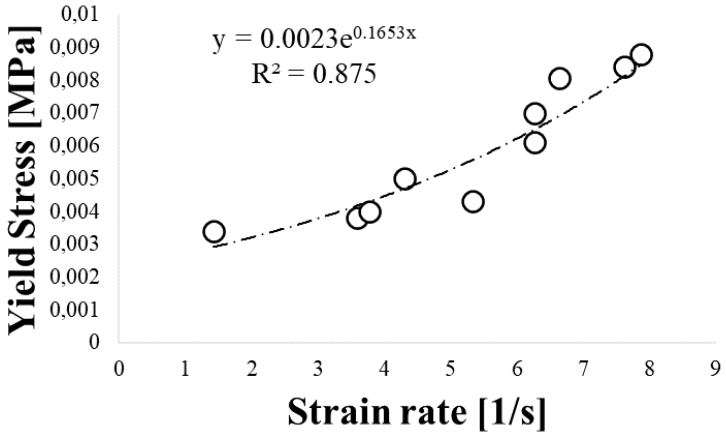

Figure 5.5 Yield Stress vs. Strain Rate for the MRF when B= 0 T

When changing the magnetic flux density, the extrusion forces became stable at different piston strokes, namely 18 mm for B = 0.180 T and 12 mm for B = 0.318 T. Thus, the strain rate values were calculated at those values of piston stroke. This was due to the different elastic and plastic properties assigned to the MRF for the different magnetic flux density values. Figure 5.6 shows the Yield Stress vs. Strain Rate curves obtained when B= 0.180 T and B=0.318 T. It can be noticed that, when increasing the magnetic flux density, the yield stress associated with a certain strain rate increased accordingly.

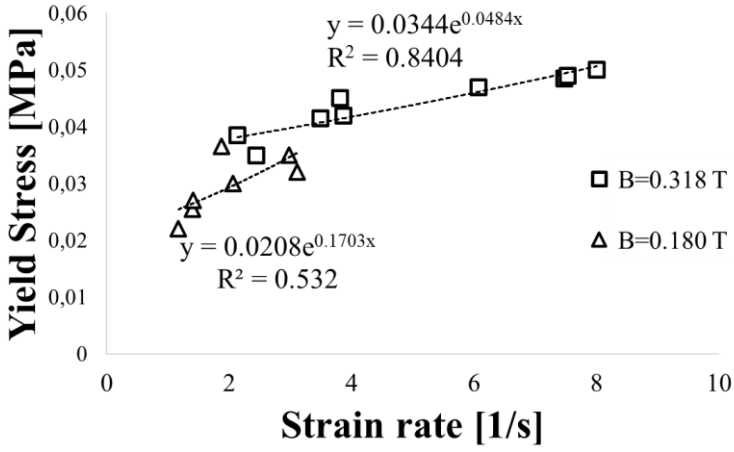

Figure 5.6 Numerical - experimental comparison between extrusion forces obtained at certain yield stress values for a magnetic flux density of 0.180 T and 0.318 T

To validate the models, as described in section 3.3.1, FE simulations of the extrusion process were conducted assigning a more refined constitutive equation to the MRF by implementing the three curves (Yield stress vs. Strain rate) shown in Figure 5.5 and Figure 5.6 instead of the perfect plastic behaviour used in the preliminary model. In this case, only the piston velocity was varied in the FE model. Then, the extrusion forces were recorded and compared with the

experimental ones. **Figure 5.7** shows the comparison between the experimental extrusion force and the numerical force obtained with the strain-rate dependent MRF material model for different magnetic flux densities.

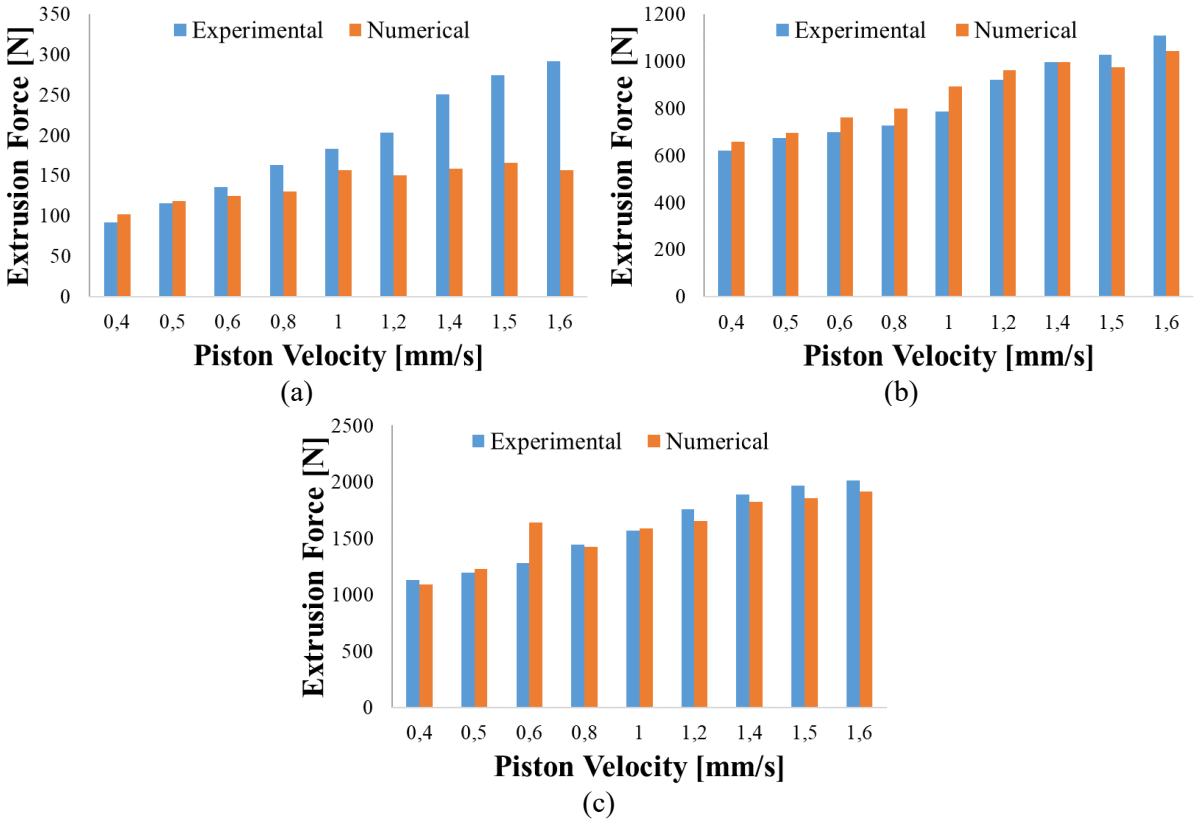

Figure 5.7 Comparison between the experimental extrusion force and the numerical one obtained with the strain-rate dependent MRF material model for (a) B=0 T (b) B=0.180 T and (c) B=0.318 T

The proposed bar chart suggest that when a magnetic field was applied (Figure 5.7c and Figure 5.7d), the strain rate dependent MRF constitutive equation was able to satisfactorily predict the extrusion force for most of the investigated piston velocities; in fact, in both cases, the average percentage difference between the experimental and numerical extrusion force was about 6%. On the other hand, in absence of magnetic field (Figure 5.7a), the MRF model was less accurate in predicting the extrusion force, especially for the high values of piston velocities. In fact, in this case, the average numerical-experimental percentage error was 23%.

Such a discrepancy could be explained by considering that, even though the fluid contains magnetic particles, they are inactive in absence of magnetic field and, thus, the MRF constitutive behaviour was remarkably far from a solid-state condition (on the contrary, it behaves like a liquid). Therefore, the elasto-plastic material model resulted to be less accurate in describing its rheological behaviour.

5.2 MRF characterization by means of bulge tests

The second proposed methodology for the MRF modelling was based on an inverse analysis approach using data from bulge tests performed adopting the MRF as forming medium. This methodology was chosen as an alternative of the previous one described in Section 3.3.1, since bulge tests better reproduce the stress conditions to which the MRF is subjected during a sheet metal forming process. Bulge tests were conducted on sheets having known properties using equipment having a solenoid to generate the magnetic field, that was specifically designed and manufactured. The pressure rate and the magnetic flux density were varied according to a Design of Experiments (DoE) while the strain experienced by the sheet material was acquired by means of a Digital Image Correlation (DIC) system to compare it with that obtaioned from FE simulations. In the following subsections, results obtained by means of this approach are presented.

5.2.1 Experimental bulge tests results on AA5754-H111 sheets using MRF

Figure 5.8a gives an overview of the bulged AA5754-H111 specimens, including the ID number, the adopted values of the pressure rate and the magnetic flux density, as well as the top view of the obtained final shapes. Figure 5.8b reports the high repeatability in the time evolution of the punch displacement curves during the replications of the tests conducted using a pressure rate of 5 bar/s and applying a magnetic flux density equal to 1.8 μT (basically, th ID06).

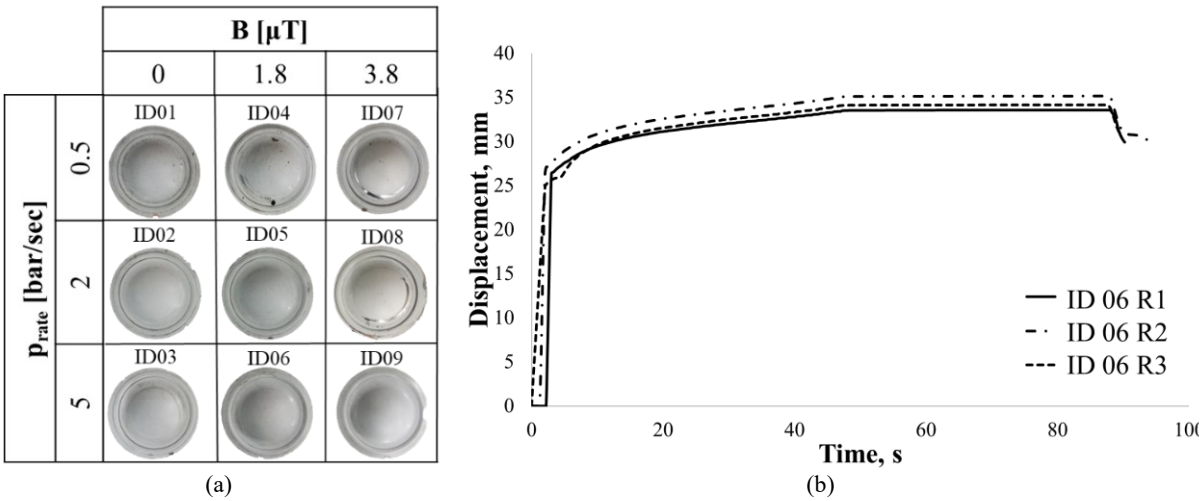

(a) (b)

Figure 5.8 (a) Overview of the experimental campaign (b) Displacement of the punch vs. time of ID03

Figure 5.9 shows the main results in terms of major strain and dome height: it can be noticed that, for all the investigated magnetic flux densities, higher values of dome height and major strain (strictly related each other) could be reached when increasing the pressure rate.

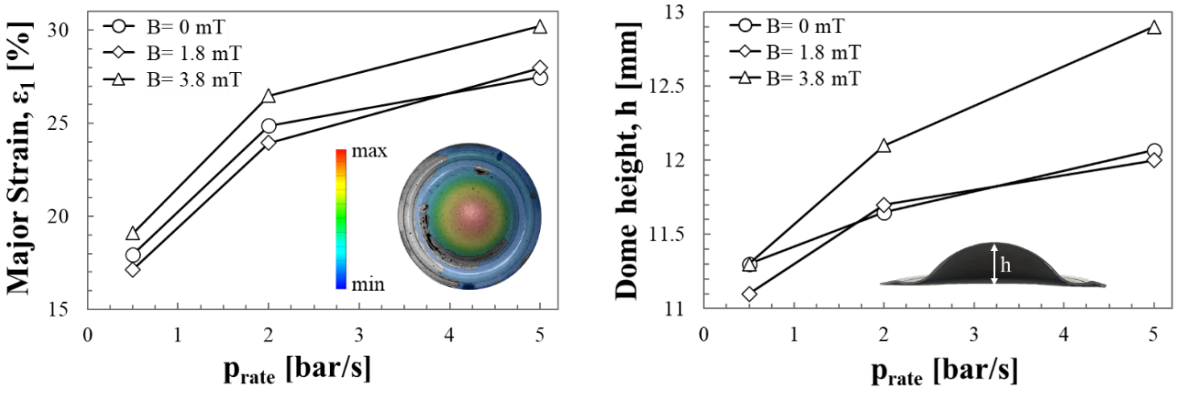

(a) (b)

Figure 5.9 (a) Major Strain at the dome and (b) Dome height reached during bulge tests according to the imposed pressure rate and applied magnetic field

If the proposed trends are more deeply analysed, it could be noticed that improvement in major strain and dome height resulted more evident when applying 3.8 mT than when the magnetic field density was increased from 0 mT to 1.8 mT. These results suggest that more evident changes in the MRF rheological behaviour occurred when it was subjected to a magnetic field greater than 1.8 mT. This was further confirmed by the macroscopic analysis of the MRF appearance at different magnetic field densities (Figure 5.10a,b,c): only in the case of 3.18 mT a significant change in the texture can be easily noticed.

(a) (b) (c)

Figure 5.10 (a) MRF MRHCCS4-A without magnetic field; (b) MRF MRHCCS4-A when a Magnetic flux density, B= 1.8 mT is applied; (c) MRF MRHCCS4-A when a Magnetic flux density, B= 3.8 mT is applied.

5.2.2 FE simulation bulge tests results on AA5754-H111 sheets using MRF

As described in section 3.3.2, FE simulations of the bulge tests were performed varying the values of E and ν according to a full factorial DoE with 3 levels (1- 5 -15 MPa and 0.35 – 0.4 – 0.49 for E and ν respectively), considering two values of p_{rate} (0.5 bar/s and 5 bar/s).

Figure 5.11 shows the major strain maps at the end of the bulge test for p_{rate}= 5 bar/s and different values of ν (0.35, 0.4, 0.49) when E = 1 MPa (Figure 5.11a), E = 5 MPa (Figure 5.11b) and E= 15 MPa (Figure 5.11c).

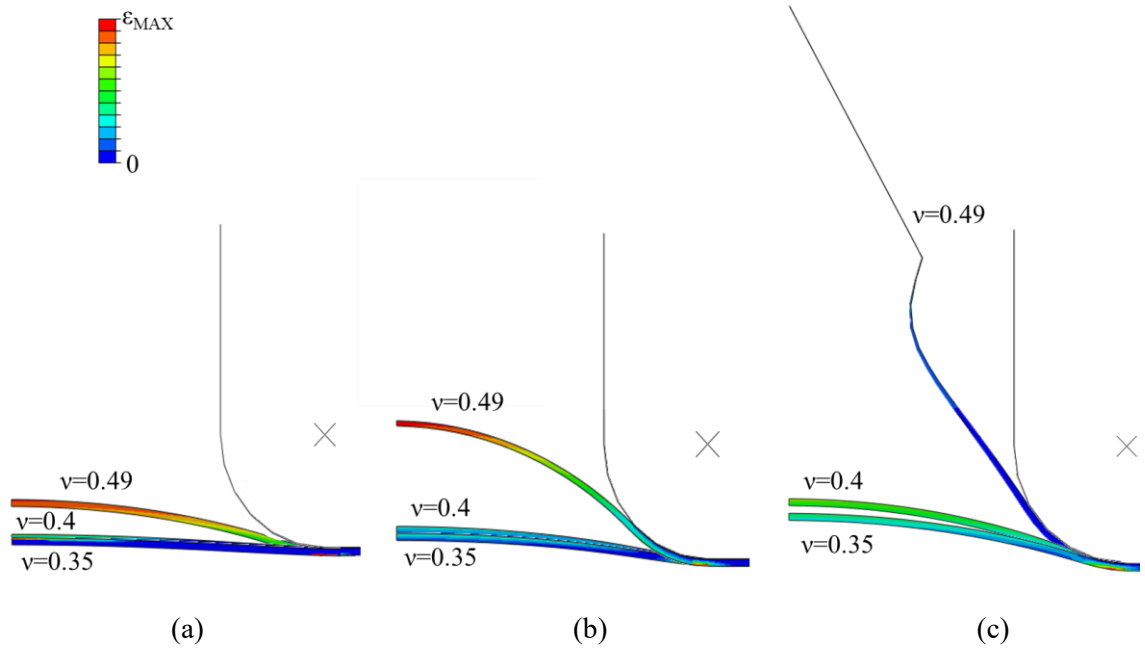

Figure 5.11 Major strain map for p_{rate}= 5 bar/s and different values of ν when (a) E=1MPa (b) E= 5 MPa and (c) E= 15 MPa

It can be seen that when increasing ν, both strain and dome height increased; moreover, this difference became much more pronounced when going from E=1 MPa to E=15 MPa. The same trend can be noticed in the case of p_{rate}= 0.5 bar/s, as shown in **Figure 5.12**

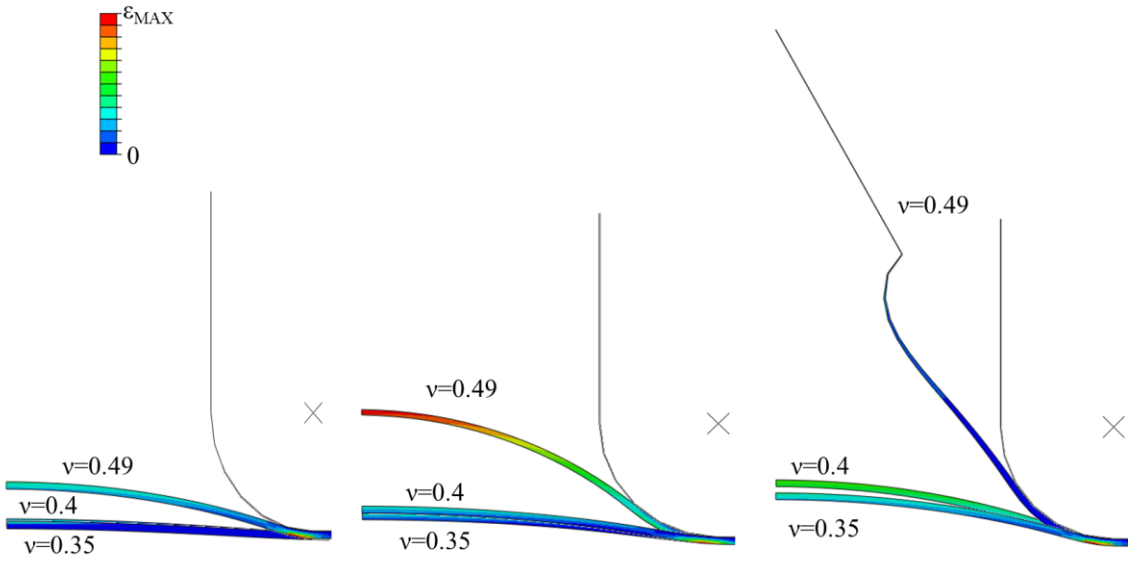

Figure 5.12 Major strain map for p_{rate}= 0.5 bar/s and different values of ν when (a) E=1MPa (b) E= 5 MPa and (c) E= 15 MPa

Table 5.1 shows a summary of the values of the dome height (h) and major strain at the dome (ε), resulting from the simulation plan, in the case of a pressure rate of 0.5 bar/s and 5 bar/s. It can be noticed that the selected range of E and ν allowed to obtain values of h from 0.73 to 38.21 mm and values of ε in the range 0.025 – 280 %, thus including also obtained experimental values.

		p_{rate}=0.5 bar/s		**p_{rate} =5 bar/s**	
E [MPa]	**ν**	**h [mm]**	**ε [%]**	**h [mm]**	**ε [%]**
1	0.35	0.73	0.01	0.76	0.025
1	0.4	0.89	0.05	0.92	0.056
1	0.49	3.3	1.3	3.44	1.5
5	0.35	1.73	0.3	1.8	0.34
5	0.4	2.19	0.5	2.28	0.58
5	0.49	8.97	13.97	9.7	16.72
15	0.35	3.3	1.31	3.44	1.56
15	0.4	4.2	2.48	4.41	2.68
15	0.49	36.29	268	38.21	280

Table 5.1 Dome height, h and Major Strain at the dome, ε resulting from the simulation plan

It is worth mentioning that output values corresponding to highest values of E (15 MPa) and ν (0.49) were not physically feasible (as shown in **Figure 5.11**c and **Figure 5.12**c).

5.2.3 Rheological properties of the MRF resulting from inverse analysis

The adopted inverse analysis procedure, which combined the results from a subset of the experimental data with the numerical results of the simulation plan, were combined to obtain the optimal values of E and ν for two investigated conditions in terms of magnetic flux density (0 mT and 3.8 mT). It can be noticed that, as summarized in Figure 5.13b, values of E varied from 5.81 MPa (in absence of magnetic field and for the lowest pressure rate) to 7 MPa (for the highest values of both magnetic field pressure rate). In addition, the results from the optimization suggested that the Poisson's ratio could be considered as a constant value regardless of the applied magnetic field and pressure rate values. Moreover, from Figure 5.13a it can be also noticed that Young's Modulus was mainly influenced by the applied magnetic field density (in accordance with the work by Liu et al. [28]), whereas it slightly increased according to the pressure rate. To validate the methodology, the experimental loading conditions at pressure rate equal to 2 bar/s were simulated: a constant value of ν=0.49 was used for the validation, whereas the values of the Young's Modulus, for each investigated magnetic flux density, were linearly extrapolated as shown in Figure 5.13a.

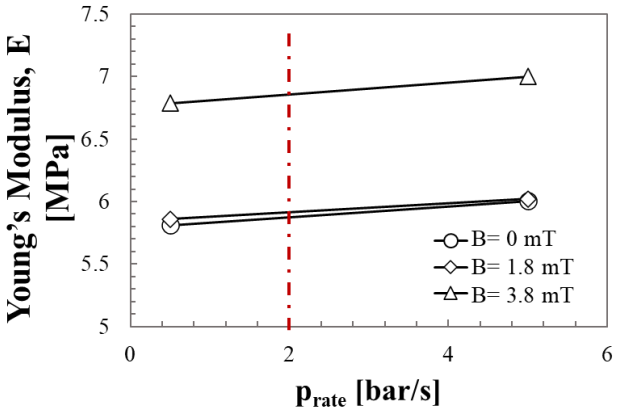

(a)

B [mT]	p_{rate} [bar/s]	E [MPa]	ν
0	0.5	5.81	0.49
0	5	6.00	0.49
1.8	0.5	5.86	0.49
1.8	5	6.02	0.49
3.8	0.5	6.79	0.49
3.8	5	7.00	0.49
0	2	5.87	0.49
1.8	2	5.91	0.49
3.8	2	6.86	0.49

(b)

Figure 5.13 (a) Trend of Young's Modulus, E according to pressure rate, p_{rate} resulting from the inverse analysis procedure; (b) summary of values of E and ν after the the inverse analysis procedure for p_{rate}= 0.5 bar/s and p_{rate}= 5 bar/s; E and ν prediction for p_{rate}= 2 bar/s.

Figure 5.14 reports a general overview of the results, combining those coming from the inverse analysis (at the magnetic flux densities of 0 mT and 3.8 mT) with those coming from the numerical simulations run for validation purposes.

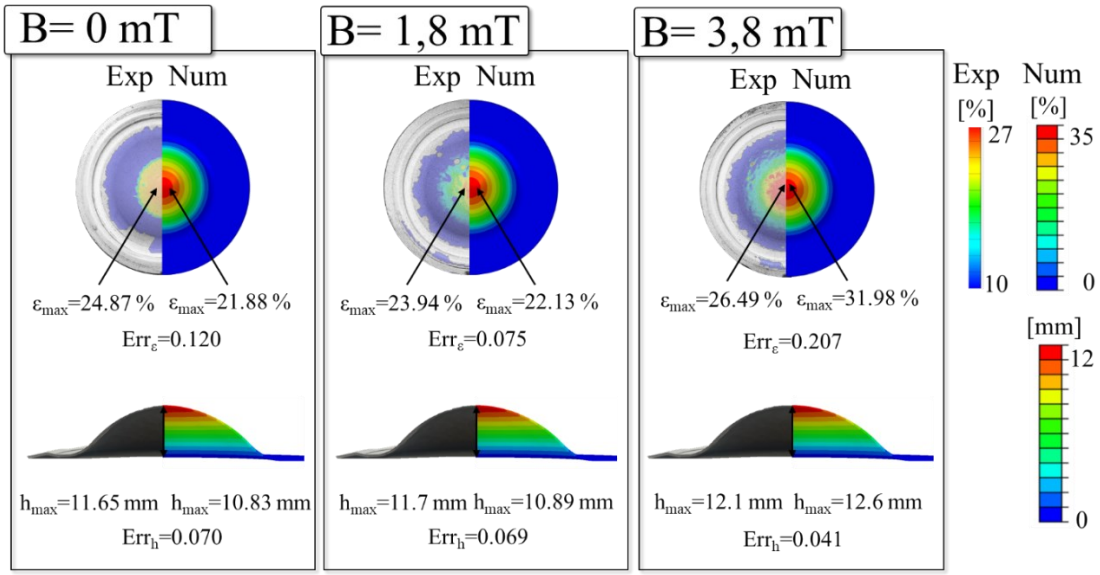

Figure 5.14 Experimental vs. numerical results of the validation of the procedure (p_{rate}=2 bar/s)

The discrepancy reported in Figure 5.14 were equal to 0.07 (0 mT), 0.069 (1.8 mT) and 0.041 (3.8 mT) regarding the final dome height; as for the final major strain, the errors were equal to 0.12 (0 mT), 0.076 (1.8 mT) and 0.21 (3.8 mT).

The inverse analysis approach, based on the construction of an accurate RS, showed good potential since it provided optimal values of the defined input parameters that resulted to be effectively descriptive of the MRF behavior both in absence of magnetic field and when a magnetic field is applied.

If compared to the methodology proposed by Wang et Al. [23,26], it can be said that the Extrusion Tests allows to study only the MRF behavior, instead a different set-up is needed to characterize the sheet metal blank. Whereas the methodology based on hydraulic bulge tests allows to study the material (sheet metal blank) formability while characterizing the MRF.

6. Application of MRFs to manufacturing processes

In this chapter, the feasibility of manufacturing a magnesium AZ31B biomedical component by means of MRF Hydroforming and a deep drawn part using MRF is evaluated. First, results from the mechanical characterization of the alloy by means of tensile tests (both at room and higher temperatures) and Single Point Incremental Forming (SPIF) tests are provided. Then, as for the biomedical component, the post-forming characteristics of a resorbable cheekbone prosthesis formed by means of innovative manufacturing processes (SPF and SPIF) are presented. Results from the FE simulations of bulge tests on Mg alloy at room temperature using MRF as forming medium are then given, with the aim of comparing the strains reached by the SPFed and SPIFed biomedical components with ones reachable with the MRF Hydroforming technology.

6.1 Manufacturing a biomedical component adopting MRFs

As previously discussed, Mg AZ31B alloys are attractive materials in the biomedical sector but they exhibit poor formability at room temperature. In this subsection, MRF Hydroforming is studied as a possible technology to manufacture a biomedical component. First, results from the mechanical characterization of the alloy by means of tensile tests (both at room and higher temperatures) and Single Point Incremental Forming (SPIF) tests are provided. Then, the post-forming characteristics of a resorbable cheekbone prosthesis formed by means of innovative manufacturing processes (SPF and SPIF) are presented. Finally, results from the FE simulations of bulge tests on Mg alloy at room temperature using MRF as forming medium are given, with the aim of comparing the strains reached by the SPFed and SPIFed biomedical components with ones reachable with the MRF Hydroforming technology.

6.1.1 The investigated biomedical component

As discussed in Chapter 2, Magnesium alloys are gaining interest for temporary prostheses manufacturing since they are biocompatible and biodegradable, thus allowing to avoid a second surgery to remove the implant. The geometry chosen for evaluating the potential of the MRF Hydroforming was a resorbable magnesium cheekbone prosthesis, being a small component with high shape details. Moreover, being a maxillofacial part, it must also fulfil aesthetics requirements. Thus, it must fit perfectly with the anatomy of the patient (requiring a high accuracy of the manufactured part). For this kind of implants, the ability to be absorbed into the human body could be very useful to repair small damages without any additional surgery step to remove the implant.

The geometry of the part was extracted from a skull simulacrum, using data from Digital Imaging and COmmunications in Medicine (DICOM) images (Figure 6.1a). Through the manipulation using mirroring techniques the geometry of the defected area was reconstructed (Figure 6.1b) and the final shape of the prosthesis to be integrated in the bone region of the patient was obtained (Figure 6.1d).

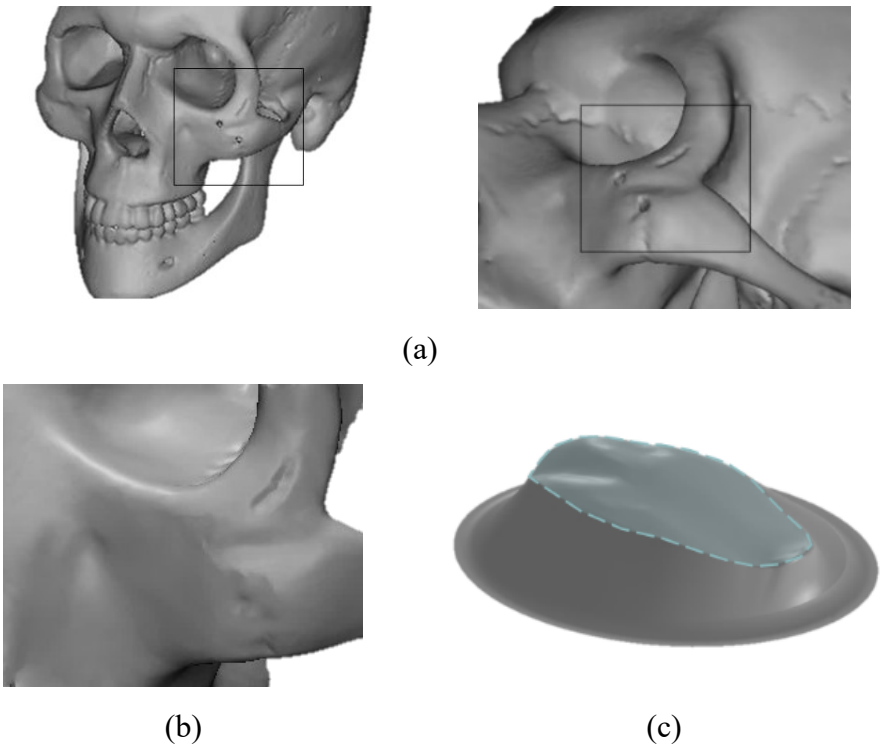

(a)

(b) (c)

Figure 6.1 Prostheses geometry determination: (a) CAD model from DICOM, (b) CAD model repaired and (c) final shape (the green area inside the dashed line)

6.1.2 Manufacturing of a resorbable cheekbone prosthesis by means of innovative processes

The first step for the manufacturing of the resorbable cheekbone prosthesis with innovative processes (SPF and SPIF) was magnesium alloy (AZ31B-H24) characterization by means of tensile tests and SPIF tests. Figure 6.2 shows the flow stress curves resulting from tensile tests at different temperatures (Room Temperature, 150 °C and 250 °C) and different crosshead speed (4.2 mm/min, 42 mm/min and 420 mm/min). It demonstrates that the ductility of AZ31B magnesium alloy increased significantly with the increase of temperature and that the flow stress is more sensitive to the strain rate at high temperature than low temperature. It is worth mentioning that all the results refer to the rolling direction.

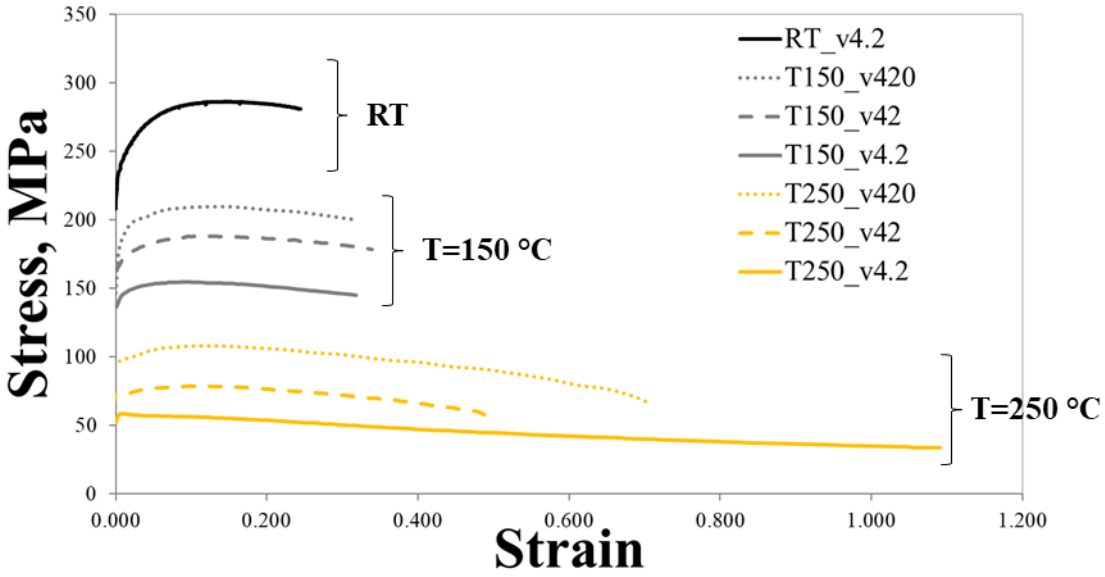

Figure 6.2 Results from tensile tests in AZ31B at different temperatures and crosshead speeds

The stress–strain curves from tensile tests were approximated by the Hollomon power law (Eq. 29).

$$\sigma = K \cdot \varepsilon^{n} \tag{29}$$

Where *K* is the strength coefficient, *n* the strain hardening exponent, σ and ε the true stress and the true plastic strain, respectively. The average value of the strength coefficient (K), the hardening exponent (n), the Yield stress (σ_y) and the Ultimate Tensile Strength (UTS) obtained from tensile tests have been summarized in Figure 6.3.

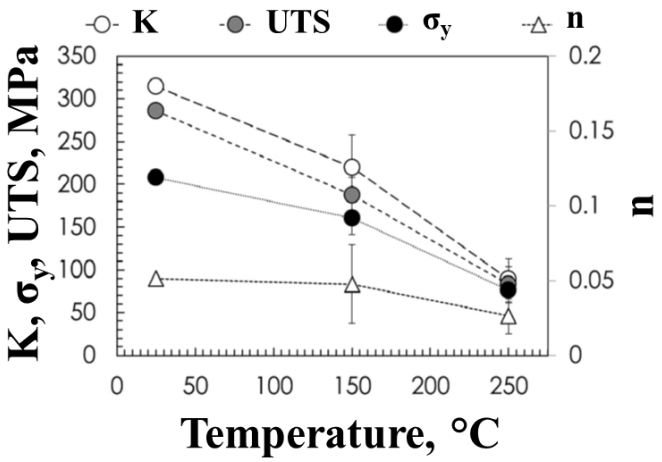

Figure 6.3 Average values of K, n, Ys and UTS obtained from tensile tests.

It can be noticed that the tensile properties of the material are strongly affected by the temperature and the strain rate, the decrease of the mean value of K, n, Ys and UTS is more

evident when the temperature exceeds the temperature of 150 °C; wide error bars in the case of the test at 150 °C and 250 °C are due to the strain rate effect. **Figure 6.4** shows the variation of the yield strength (average values are considered for each condition) obtained from tensile tests, at different temperature and crosshead speeds. It is observed that the strain rate effect on the yield strength becomes more and more pronounced when the temperature is increased.

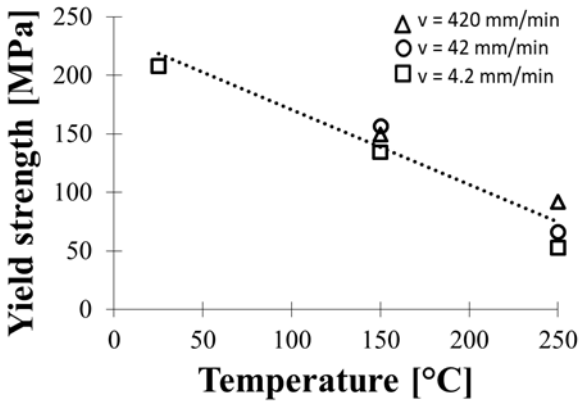

Figure 6.4 Yield strength variation according to temperature at different crosshead speeds

Regarding SPIF tests, not all the different combinations of process parameters allowed to reach the target depth and a final safe part. Figure 6.5 reports an overview of the experimental campaign in terms of the final outcome of the deformed parts.

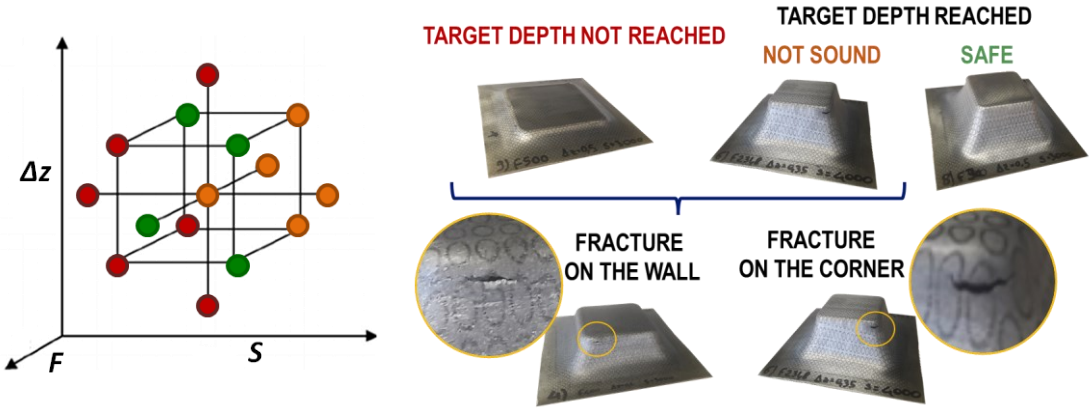

(a) (b)

Figure 6.5 (a) Results from SPIF-ability tests: green circles represent safe parts, orange circles represent parts which reached the target depth but were not safe, red circles represents parts for which fracture occurred before reaching the target depth; (b) Examples of safe and not safe components

In particular, Figure 6.5a shows the designed CCD along with a specific color for each of the possible outcome of the SPIF test: more in details, green circle if the final component reached the target depth without rupture , orange circle if it reached the target depth but rupture occurred and red circle if fracture occurred before reaching the target depth. Examples of the mentioned

cases are shown in Figure 6.5b. In the same figure, it can be noticed that for some specimens fracture occurred in the wall area, whereas for other specimens it occurred on the corner area. Figure 6.6 shows a summary of results of the SPIFability tests, in terms of maximum major strain reached ($\varepsilon_{1,max}$) and the depth at fracture ($z_{fracture}$) according to the maximum temperature reached during the tests.

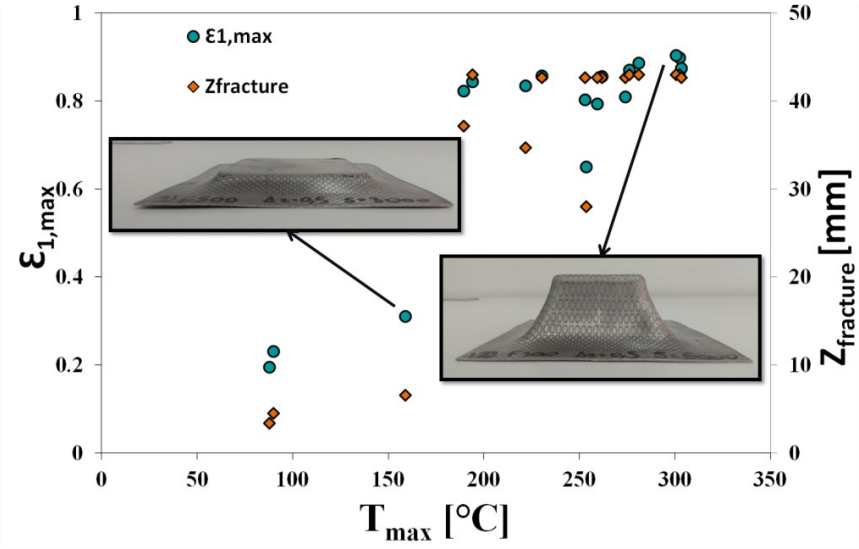

Figure 6.6 $\varepsilon_{1,max}$ and $Z_{fracture}$ values for each temperature

It can be seen that different combinations of the process parameters led to different maximum temperatures of the blank, ranging from 88 up to 300 °C. It is evident that the Mg formability (maximum major strain experienced by the material) clearly increased when the temperature was higher. In fact, more than 65% of the target depth was reached when the temperature was at least 190°C; on the contrary, in all tests where that value was not reached, only small depths (less than 7 mm) were achieved.

The SPIF-ability tests where the process temperature levels (88 °C, 159 °C and 275 °C) results were closest to those set during the tensile tests (25, 150 and 250 °C) were considered for evaluating the Fracture Forming Lines (FFLs). In particular, the FFLs plotted in Figure 6.7 were obtained analysing samples from tests where the fracture occurred in the corner and combined with others where the fracture occurred in the wall area. In the test characterised by T_{max} = 275 °C (Figure 6.7c) the fracture occurred simultaneously both in the corner and in the wall, strains at fracture were obtained from two different samples (one with the fracture in the corner and the other with the fracture in the wall). The correlation between the temperature and the formability is also confirmed by the FFLs: in fact, the values of the intercept of the FFL on the Major Strain axis (FFL_0) increases according to the maximum temperature (0.142 at 88 ◦C,

0.530 at 159 ◦C and 1.327 at 275 ◦C); in addition, the values of the slope of the FFL (-1.48 at 88 ◦C, -1.65 at 159 ◦C and -0.99 at 275 ◦C) are consistent with its typical value (-1) [101].

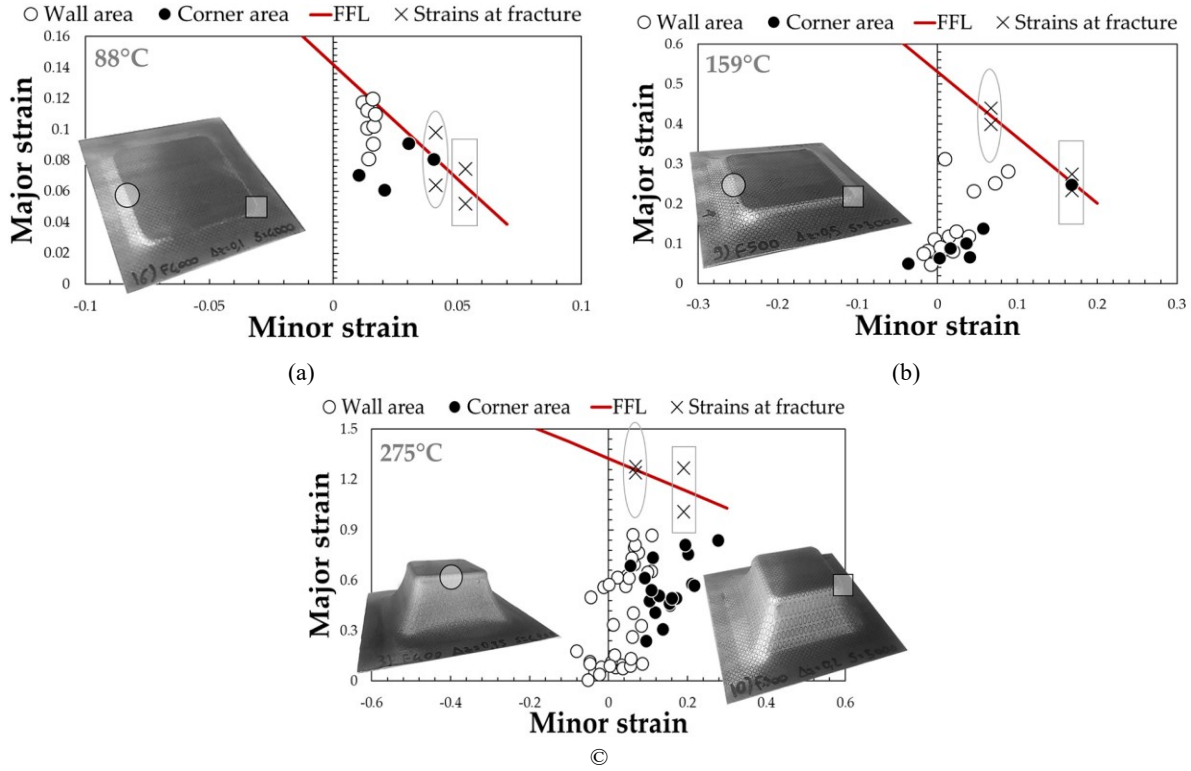

Figure 6.7 Strain distribution and FFLs from SPIFability tests: (a) T_{max} = 88 ◦C, (b) T_{max} =159 °C and (c) T_{max} =275 °C

Figure 6.8a shows the temperature trends during two tests carried out using the same levels of step down (Δz = 0.5 mm) and Feed Rate (F = 300 mm/min) and different values of Spindle Speed (3000 and 5000 RPM). It is clearly evident the predominant effect of the Spindle Speed on the temperatures reached during the process: when increasing spindle speed from 3000 RPM to 5000 RPM, temperature variation between the two tests was more than 100°C.

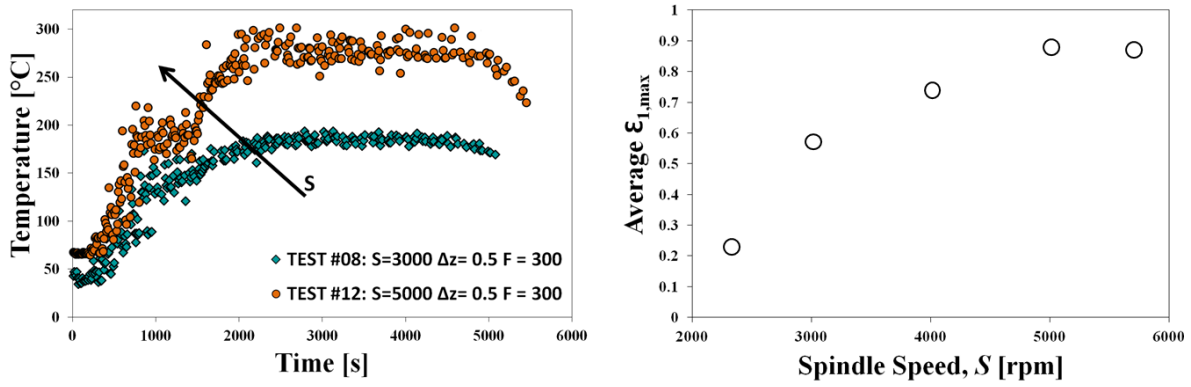

Figure 6.8 (a) Temperature trend for SPIFability tests at different Spindle Speeds, S (b) Average $\varepsilon_{1,max}$ for each level of Spindle Speed, S

In fact, the recorded difference could be easily explained by considering the friction at the tool/sheet interface: if the tool rotates at higher speed, the tool surface will slide over the work piece much more often, generating more heat.The effect recorded was shown to be in accordance with other previous research conducted on the same alloy [102] as well as on other metals (AISI 304 [103], Ti [104]) and on polymers (PVC, PC, PP, UHMWPE, PCL [105]) where it was found that temperature mostly depends on spindle speed. In addition, Figure 6.8b, showing the average maximum major strain ($\varepsilon_{1,max}$) according to the Spindle Speed value adopted during the tests, confirms the influence of the Spindle Speed on the Mg formability during SPIF-ability tests.

For this reason, for the subsequent hardness and microstructure analyses, three samples without rupture characterized by different values of Spindle Speed (3000 RPM, 4000 RPM and 5000 RPM) were chosen. The final geometry, maximum temperature, final depth, and maximum values of the major strain reached by the selected specimens are summarized in Table 6.1. The different samples experienced different temperature levels during the forming process, mainly due to the different levels of the spindle speed; on the other hand, since all the specimens reached the target depth, they were characterized by similar maximum values of the major strain.

	Specimen		
Parameter	AZ31-S3000	AZ31-S4000	AZ31-S5000
Final geometry	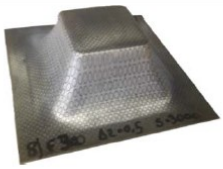	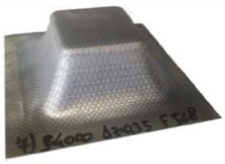	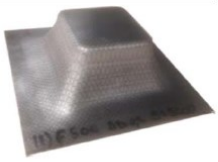
Max temperature (°C)	194	230	302
Final depth (mm)	43	42.7	43
Maximum major strain	0.84	0.86	0.9

Table 6.1 Final geometry, maximum temperature, final depth, and maximum values of the major strain reached by the selected specimens

The microstructure of the undeformed material (AZ31) and of the samples extracted at the forming depth of z=30 mm from the specimens AZ31-S3000, AZ31-S4000, AZ31-S5000 have been shown in Figure 6.9 together with the average grain size.

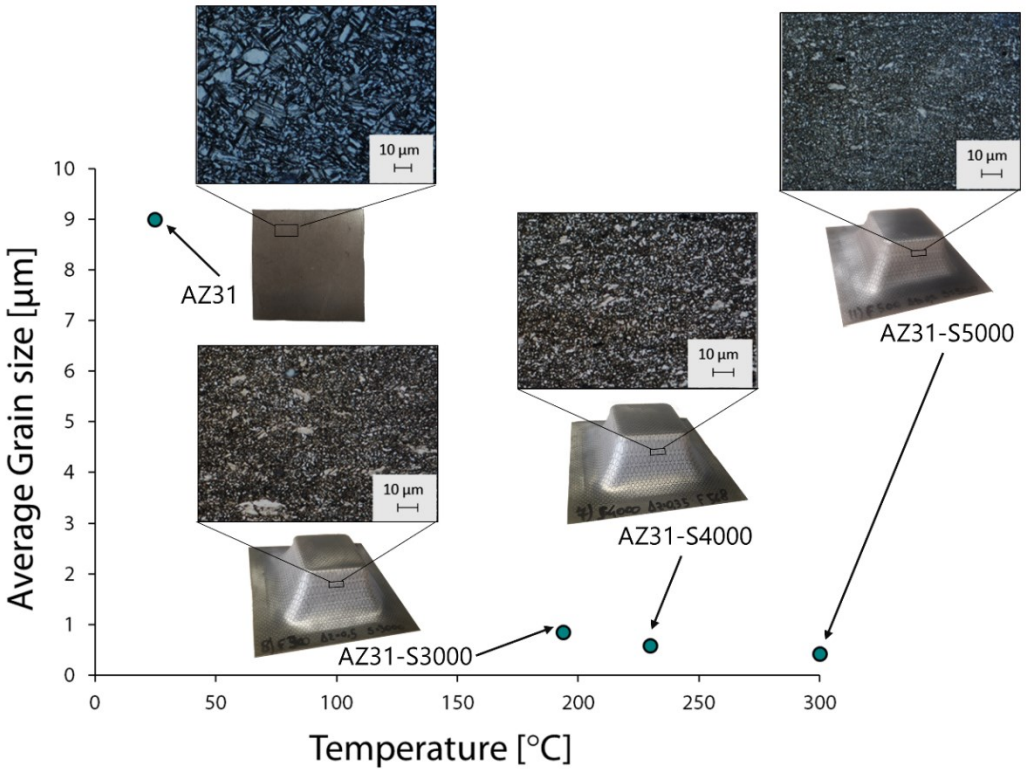

Figure 6.9 Effect of temperature on the average grain size of Mg samples extracted from the specimens processed by SPIF at z =30 mm)

It can be seen that the undeformed material was characterized by a non-homogeneous grain distribution and by an average size of 9 µm. On the contrary, the microstructure of the samples extracted by the specimens obtained by SPIF appeared partially recrystallized and characterized by not only a more homogeneous grain distribution but also by a much larger number of grains, considerably finer (average dimension lower than 1 µm) than the initial ones. The dynamic recrystallization could be promoted by the high level of temperature reached by the material [106][107]. Moreover, comparing the different forming conditions, a slight decrease in the average grain size can be noticed when higher temperatures were experienced by the material.
Before analysing the grain size distribution along the thickness direction, thickness distribution was first evaluated and it is shown in Figure 6.10. It can be seen that moving from the region of the specimen which was clamped during the test (point A) to the central region (point B) the thickness reduced and, as a consequence, the major strain increased.

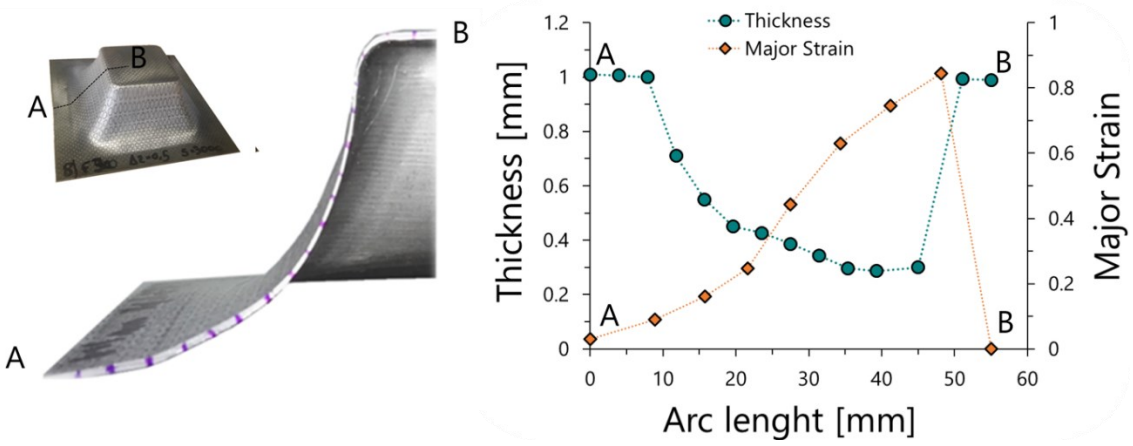

Figure 6.10 Thickness and major strain distribution along the arc length of AZ31-S3000 specimen

To assess the effect of the strain level (i.e. of the thickness) on the microstructure evolution, samples were extracted from the same specimen (AZ31-S5000) at different depths (z = 10 mm and z = 30 mm) and analysed using the Optical Microscope and the grain size distributions along the thickness direction have been compared in Figure 6.11.

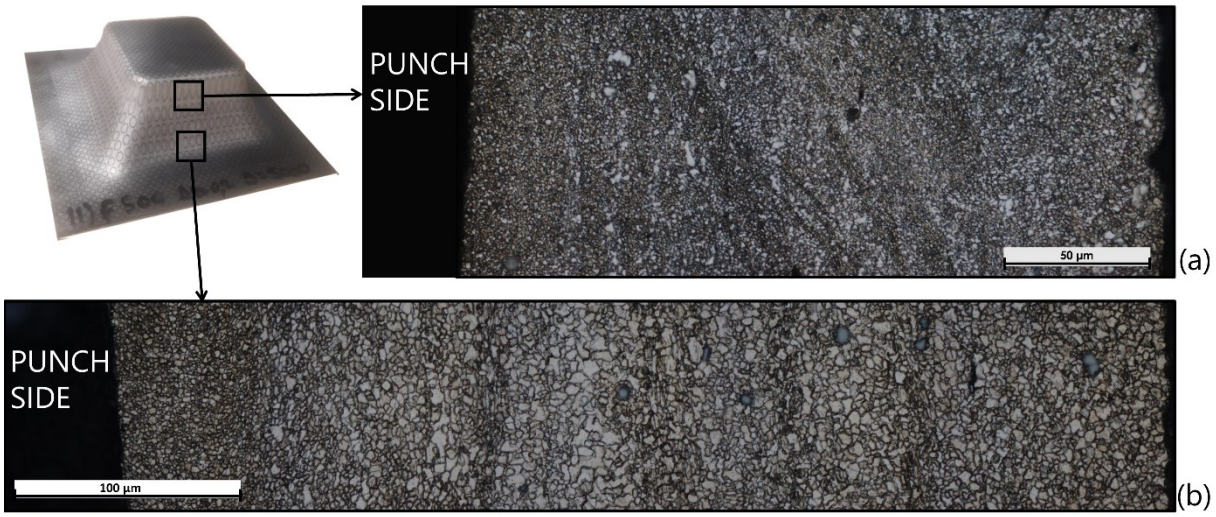

Figure 6.11 (a) Microstructure along thickness direction for test AZ31-S5000 at different depths: (a) z=30 mm (t=0.24mm); scale bar: 50 µm and (b) z=10 mm (t=0.47mm); scale bar: 100 µm

It could be observed that at high forming depths (i.e., high strains and low thickness values) the microstructure appeared homogeneous (Figure 6.11a), whereas at low forming depths (i.e., low strain and high thickness values) the grain size was small at the tool/blank interface (punch side, left part of Figure 6.11b) and tended to increase moving towards the external surface (right side in Figure 6.11b).

For the investigated specimens, the difference in the average grain size between the outer and inner blank surfaces was about 1 µm. Such an experimental result can be justified by the combined effect of the temperature and the strain rate experienced by the material during the

SPIF process. The internal side (punch side) of the specimen experienced high temperatures, being in direct contact with the punch, which promoted here the dynamic recrystallization; at the same time, the internal surface was subjected to high strain rates, which gave an additional contribution to the grain refinement [102]. At high forming depths, the gradient of both the temperature and the strain rate along the thickness direction decreased and its effect disappeared.

In Figure 6.12 the effect of the maximum temperature experienced during the forming process by the material is reported in terms of both microhardness measurements (performed on the samples extracted from the investigated SPIF specimens at z = 30 mm) and forming force values (acquired when the rotating tool was at the same depth). In the case of samples extracted from the specimen AZ31-S3000, the final hardness was higher than that of the as received material (AZ31). Thus, the effect of the strain hardening can be considered predominant in this case. On the contrary, for samples extracted from the specimens AZ31-S4000 and AZ31-S5000, the hardness was lower than the as received material (AZ31); moreover, the two samples were characterised by a hardness values lower than the sample extracted from the AZ31-S3000 specimen.

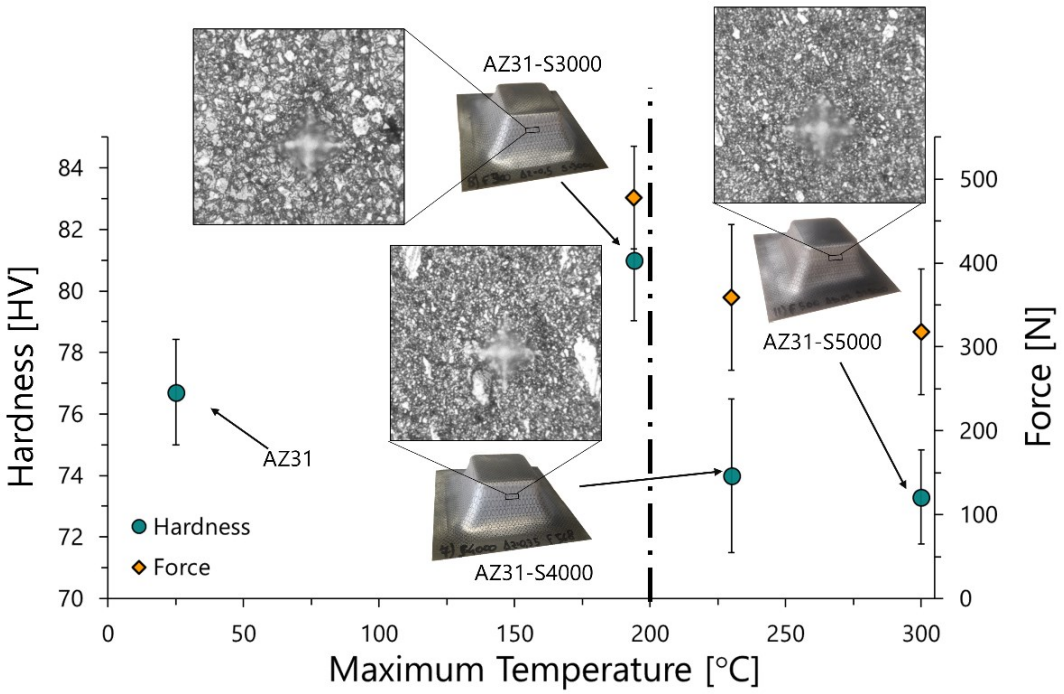

Figure 6.12 Hardness of the Mg samples extracted from the as-received sheet (AZ31) and from the specimens processed by SPIF (AZ31-S3000, AZ31-S4000, and AZ31-S5000) and forming force for different temperature levels (194, 230, and 300 °C) at the same depth (z=30 mm)

Thus, it can be said that as the maximum temperature increased (due to the Spindle Speed increase), the material softening due to dynamic recrystallization occurred, therefore resulting in a decrease of the forming force. The reason why different hardness level were measured may be due to the different temperatures experienced during forming: since 200 °C can be assumed as the transition temperature from brittle to ductile behaviour for the investigated alloy [108], only the specimens AZ31-S4000 and AZ31-S5000 experienced a temperature higher than 200°C, while AZ31-S3000 did not.

The activities for the prostheses manufacturing and the subsequent evaluation of their post forming characteristics were conducted using the facilities available in Politecnico di Bari (Italy), University of Girona (Spain) and University of Seville (Spain).
To manufacture the prosthesis by SPF, Square blanks (size: 150 mm × 150 mm) were used. Argon gas was used as forming medium and the pressure profiles obtained from FE simulations [99] were implemented. In particular, tests were conducted adopting 2 different pressure profiles, able to keep the strain rate close to the targets 0.001 and 0.0005 s^{-1}. Each condition was replicated three times. To perform experimental tests a 2500 kN electro-hydraulic press machine (Figure 6.13a) equipped with heated tools for high temperatures (up to 1000 °C) was adopted. To drastically reduce the costs of the manufacturing process, an expendable ceramic insert was fabricated by investment casting and adopted as a die for SPF tests. In particular, the following manufacturing route was implemented to create the ceramic tool (Figure 6.13b): (i) the design of the die geometry (Step1); the fabrication of the pattern by stereolithography (Step 2); the creation of a highly flexible resin pattern replica (Step 3); the production the ceramic die using the resin replica (Step 4). Thanks to the adoption of expendables inserts, components with undercuts could be produced and easily extracted at the end of the forming operations.

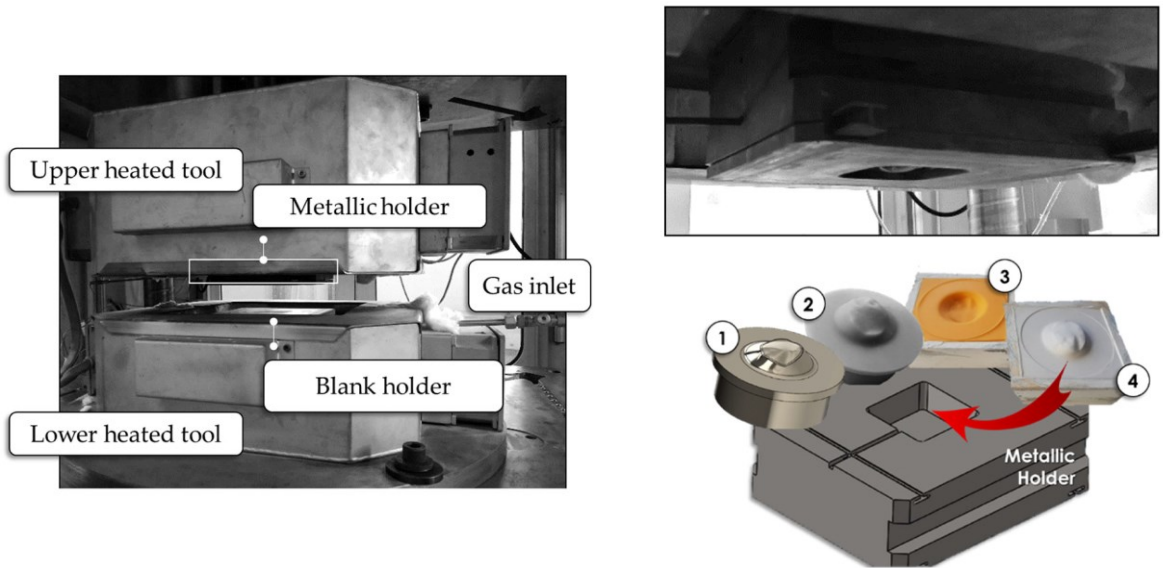

(a) (b)

Figure 6.13 (a)Experimental facilities used to manufacture the case study via SPF; (b) adopted procedure to manufacture the expendable die

The experimental setup adopted to manufacture the prostheses via SPIF is reported in Figure 6.14. The same equipment adopted for the SPIFability tests (Kondia HS1000 Vertical machining center) was used. Since the dimension of the initial blank was equal to the one adopted for the SPF process, 4 tests could be simultaneously carried out using the same blank. To reduce the spring-back and bending effects, a metal frame was adopted to support the blank during the forming process. SPIF tests were performed using a punch diameter of 4 mm and varying, according to a Central Composite Design (CCD) experimental plan (α equal to 1.5), the following process parameters: (i) Step Down (SD), (ii) Feed Rate (FR), (iii) Spindle Speed (SS), thus obtaining 15 test conditions.

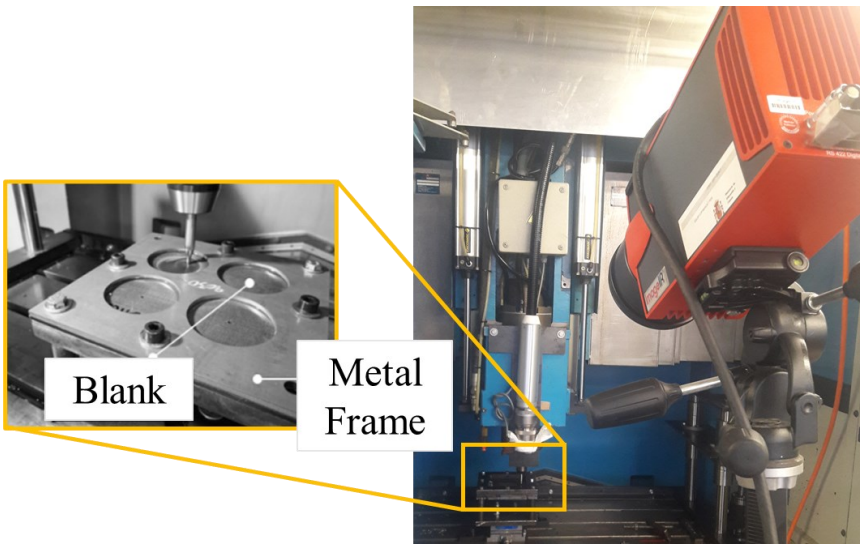

Figure 6.14 Experimental SPIF facilities used to manufacture the case study

The highest and the lowest values of the investigated process parameters (in Table 6.2) were chosen taking into account the limits of the experimental setup while trying to avoid too large cycle times. The final strain state on the outer surface of the prosthesis obtained by SPIF and the thickness distribution along a longitudinal central path were evaluated off-line using the 3D circle-grid-analysis acquired by the digital measurement system ARGUS® (accuracy: 0.1%, camera resolution: 1624 × 1236 pixels). A circular grid pattern (diameter: 1 mm) was thus marked on the blank before the test.

	Feed Rate [mm/min]	Spindle Speed [rpm]	Step Down [mm]
Min	120	2500	0.0150
Max	600	7500	0.0900

Table 6.2 Max and min values of the SPIF process parameters adopted for the case study manufacturing.

The thickness distribution obtained by means of the ARGUS system was also compared to the one obtained using a calliper (Mitutoyo 573–701 Absolute Digimatic Offset, accuracy: 0.02 mm, resolution: 0.01 mm). In this case, to obtain the thickness distribution, each sample was cut by means of a metallographic cutting-off machine and the thickness was measured (3 replications for each measurement) along the central longitudinal path.

Thickness distributions of the prosthesis manufactured by SPF when setting the investigated strain rate levels are presented in Figure 6.15. Even if the differences between the thickness distributions are small, a lower mean value of the thinning was obtained when using the gas pressure profile calculated setting the target strain rate to 0.0005 s^{-1}.

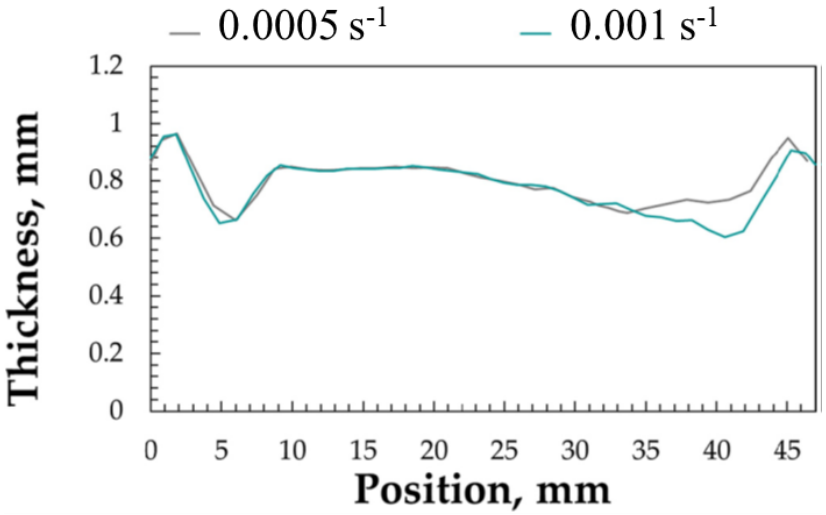

Figure 6.15 Thickness distributions from experimental SPF tests

In particular, the strain rate reduction determined an increase of the minimum thickness of about 10% (the minimum thickness values measured on the prostheses were 0.62 mm and 0.57 when using an equivalent strain rate of 0.0005 s^{-1} and 0.001 s^{-1} respectively), which affects both the mechanical response and corrosion behaviour [109].

In Table 6.3 the results of the SPIF tests aimed at producing the case study are reported in terms of minimum thickness for all investigated conditions are reported. It can be noticed that the combination of high SD and FR values provided parts with the lowest thinning, thus allowing a good mechanical response of the prosthesis.

ID	FR [mm/min]	SS [rpm]	SD [mm]	Min Thickness [mm]
0	200	3333	0.0275	0.78
1	200	3333	0.0775	0.86
2	200	6667	0.0275	0.73
3	200	6667	0.0775	0.82
4	520	3333	0.0275	0.85
5	520	3333	0.0775	0.80
6	520	6667	0.0275	0.75
7	520	6667	0.0775	0.84
8	120	5000	0.0525	0.81
9	600	5000	0.0525	0.81
10	360	2500	0.0525	0.83
11	360	7500	0.0525	0.82
12	360	5000	0.0150	0.74
13	360	5000	0.0900	0.89
14	360	5000	0.0525	0.79

Table 6.3 Results in terms of Ra, SA and min-thickness from SPIF tests aimed at producing the case study

In Figure 6.16, the experimental thickness distributions (measured by the caliper) concerning three selected SPIF tests, namely ID12, ID10 and ID5 are shown along with the thickness distribution concerning the ID5 measured by the ARGUS system (dashed line); in addition, also images of the 3 samples and the strain map acquired by the ARGUS system have been included in the same figure.

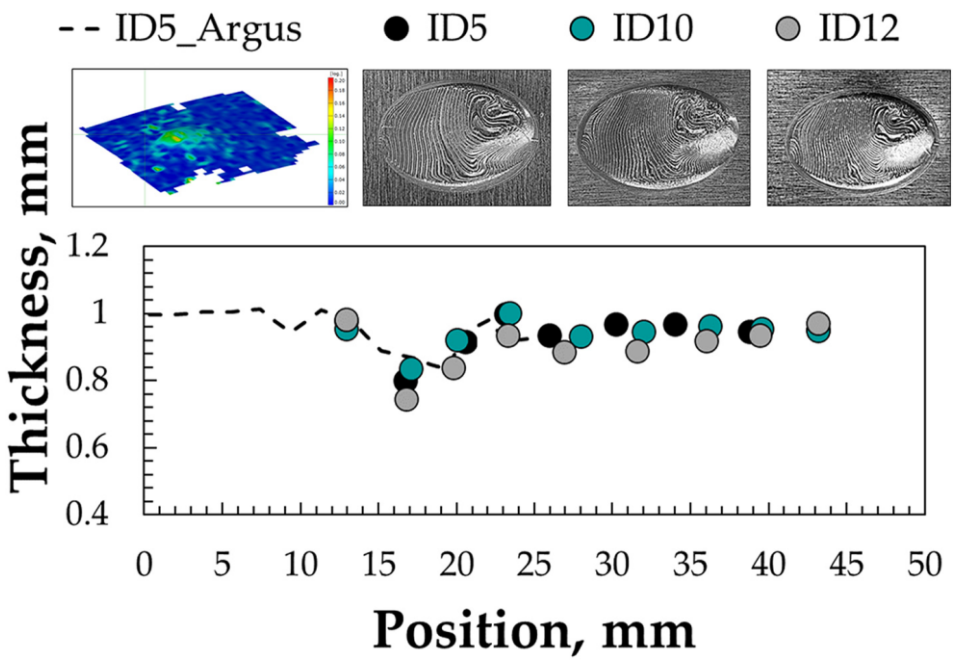

Figure 6.16 Experimental thickness distributions concerning ID12, ID10 and ID5 (circles indicate measurements by the calliper, while the dashed line indicates measurements by the ARGUS system)

It can be noticed that the investigated process parameters determined differences of about 0.3 mm in the range 12-20 mm, especially when large strain occurred. As for the ID5, the robustness of data from ARGUS was checked by comparing the thickness distribution (obtained by applying the volume constancy) with the thickness values from the caliper measurements. Although the thickness measured using the calliper was slightly lower than those from ARGUS (especially in the deeper region of the prosthesis), a satisfactory fitting could be achieved.

In Figure 6.17 the experimental strains of ID05 (for which fracture occurred) and the FFL obtained at 88°C are shown. It is worth mentioning that the FFL obtained at 88 °C was chosen for evaluating ID05 strains since during this test temperature was lower than 88 °C. It can be seen that the level of principal strains is slightly above the FFL, thus showing the effectiveness of the obtained FFL. When comparing the two manufacturing processes, the blank capability to copy the die geometry (in this case made of a ceramic material using an investment casting process, thus drastically reducing the tool cost) during the SPF allowed to obtain very good surface quality, however a larger thinning (more than 20%) was measured on the formed prosthesis, which was strictly related to the stretching condition that the material experienced during the forming. Nevertheless, attention should be also focused on mechanical and technological aspects related to the adoption of the investigated processes. In fact, the excellent results in terms of surface quality and accuracy coming from the SPF process were partially counterbalanced by the need of producing a die having the shape of the part to be manufactured.

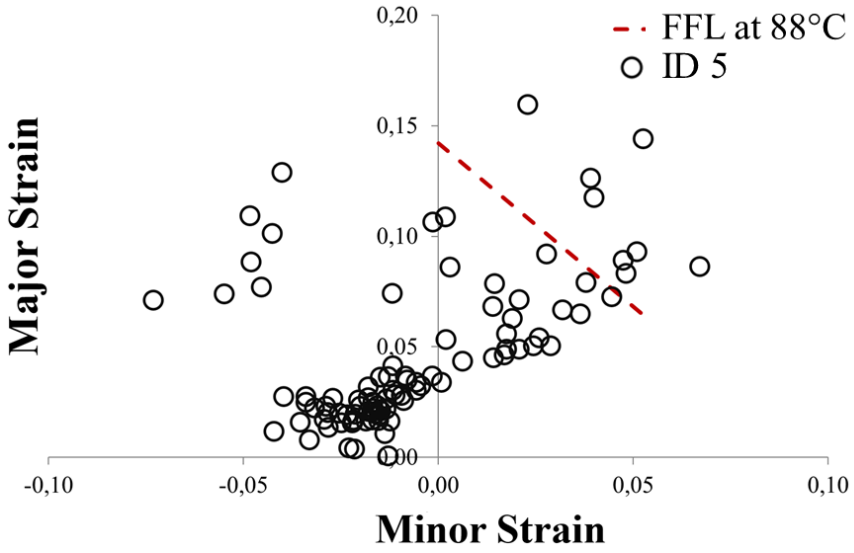

Figure 6.17 Experimental values of principal strains concerning ID5 compared to the FFL at 88°C FFLs from Section 6.1

In addition, the AZ31 alloy exhibited its superplastic tendency only at high temperature (450 °C), which made the SPF process more complex than the SPIF. The latter, in fact, was highly flexible and, at the same time, able to reach levels of strain well above the FLC, thus making possible to the production of very complicated shapes (as the one here discussed). In light of this, the SPIF process should be regarded as a promising solution to quickly and economically manufacture customised prostheses (as in the case of an urgent bone reconstruction) or resorbable implants. On the contrary, the SPF process should be considered more adequate for the manufacturing of permanent (and even more complicated) implants, specifically designed and associated with high quality requirements.

6.1.3 Evaluation of the feasibility to manufacture a magnesium resorbable prosthesis by means of MRF Hydroforming

Bulge tests were simulated using the commercial software ABAQUS/Explicit and using the same FE model of the bulge tests used for the inverse analysis, described in section 3.3.2.4. In this case, Mg mechanical properties at room temperature obtained with tensile tests (described in section 3.1.2) were assigned to the sheet. Instead, MRF's mechanical properties (i.e., Young's Modulus, *E,* and Poisson's ratio, *v*) obtained by means of the inverse analysis (described in section 3.3.2.5) were given to the MRF. Regarding the loading conditions, the highest and the lowest pressure rates used during the experimental bulge tests in aluminium alloy (0.5 and 5 bar/s) were simulated. The final values of strain were then compared in order to assess the effect of the magnetic flux density (B) and pressure rate (p_{rate}) on Mg formability, due to the changes of the rheological properties of the MRF. Moreover, the obtained strains

were compared to the resorbable magnesium prosthesis obtained by means of SPF and SPIF, in order to evaluate the feasibility to manufacture the previous case study by means of MRF Hydroforming.

Based on the results of the MRF characterization by means of inverse analysis (described section 5), the highest and the lowest pressure rate value (0.5 and 5 bar/s) and the highest and the lowest value of magnetic flux density (0 and 3.8 μT) were adopted for the FE simulation of the bulge tests on AZ31B alloy using MRF. **Figure 6.18** shows the effect of the magnetic flux density (B) and pressure rate (p_{rate})on Mg formability: on the one hand, for each pressure rate, increasing the magnetic field from 0 μT to 3.8 μT led to higher stain levels at the same punch displacement. On the other hand, when changing the pressure rate level for each magnetic field, no changes in strain levels were observed.

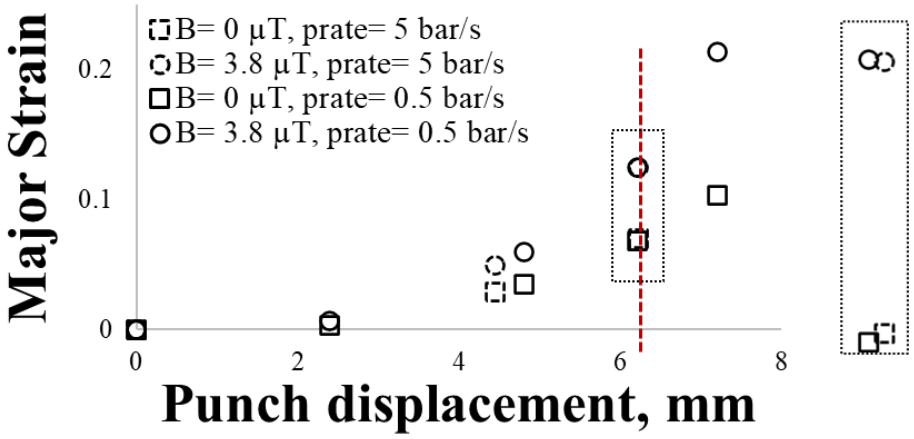

Figure 6.18 Strains vs. punch displacement at different magnetic flux densities (B) and pressure rates (p_{rate})

To evaluate the feasibility to manufacture a magnesium resorbable cheekbone prosthesis by means of MRF Hydroforming, strains obtained by means of bulge tests were compared to the ones of the magnesium prostheses obtained by means of SPF and SPIF processes (whose results have been shown in section 6.2). **Table 6.4** shows the maximum strains reached by the Mg prosthesis formed by SPF and SPIF as well as the maximum strain before failure reached during bulge tests using MRF.

	SPIF (Prosthesis)	**SPF (Prosthesis)**	**BULGE MRF (Hemispherical geometry)**
ε_{max}	0.17	0.22	0.23

Table 6.4 Maximum strains reached by the Mg prosthesis formed by SPF, SPIF and the maximum strain before failure reached during bulge tests using MRF

It can be thus stated that, since the level of strains is comparable, the MRF Hydroforming would be a suitable process to produce such prosthesis.

6.2 Manufacturing a deep drawn part adopting MRFs

In this subsection, results of Hydromechanical Deep Drawing process using MRF on the magnesium alloy are presented to evaluate the advantages of adopting MRFs in the hydromechanical deep drawing process.

6.2.1 FE model of the Hydromechanical Deep Drawing Process

To reproduce hydromechanical deep drawing tests using MRF within the Abaqus/CAE environment, a 2D axisymmetric approach was adopted to reduce computational costs. To set the punch radius and the entry radius of the cavity (which acts as a die during the deep drawing process), the following geometrical constraints were considered, given the equipment previously designed for the bulge tests (Figure 6.19a):

- Die cavity internal radius= 16 mm;
- Blank holder (BH) fillet radius= 8 mm;
- Internal BH radius= 16 mm;
- Maximum sheet diameter= 68 mm (**Figure 6.19**b)

As shown in Figure 6.19, the preliminary FE model did not take into account the presence of the MRF. The tools (punch, blankholder and die cavity) were modelled as analytical wire-based rigid bodies, therefore no mesh was needed, whereas the blank (0.5 mm thick) was modelled as a deformable shell body and it was meshed with 204 CAX4R (4-node axisymmetric bilinear quadrilaterals with reduced integration and hourglass control) elements (3 elements along the thickness direction and 68 along the radial direction). Material plastic behaviour was modelled according to the isotropic Von Mises Yield formulation. The contact between the blank and the punch was modelled according to a penalty formulation, setting the coefficient of friction between the blank and the punch equal to 0.2 [100] and the other contact pairs (BH-Sheet, Die cavity-Sheet) equal to 0.05. The mechanical properties of the AA5754-H111 ($E = 70$ GPa, $\nu = 0.3$, $\rho = 2.7$ g/cm^3) as well as the flow curve and the FLC (which is necessary to activate the damage criterion) were assigned to the sheet.

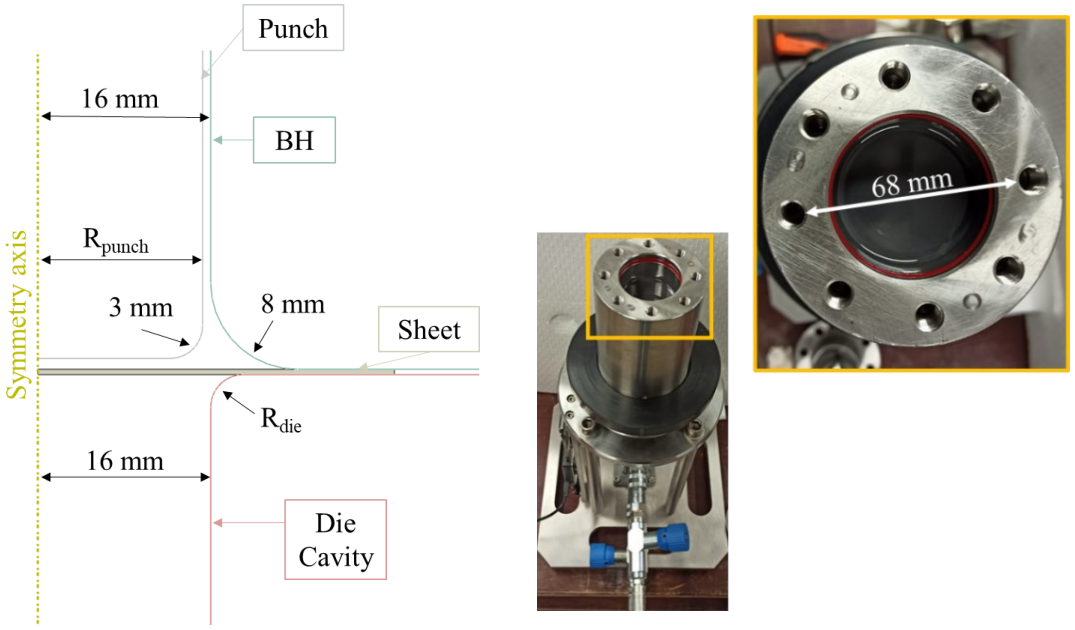

(a) (b)

Figure 6.19 (a) FE model of the deep drawing process (b)Top view of the die cavity of the experimental equipment with the indication of the maximum sheet diameter

To increase computational efficiency, a Semi-Automatic Mass Scaling was applied to the sheet, setting the stable time increment equal to 1E-005 and updating the scaling with a frequency of 100 increments. In the simulation plan, different values of punch radius (R_{punch} in Figure 6.19a) – 13.25 mm, 14.75 mm, 15.25 mm – and die cavity fillet radius (R_{die} in Figure 6.19a) – 3 mm, 5 mm and 8 mm – were investigated. Being the maximum sheet diameter (D_0) equal to 68 mm (see Figure 3.31b), the maximum achievable drawing ratios, β (see Eq. 28) would have been 2.6, 2.3 and 2.2 if adopting a punch radius, R_{punch}, equal to 13.25 mm, 14.75 mm, 15.25 mm respectively.

$$\beta = \frac{D_0}{2 * R_{punch}} \tag{28}$$

Numerical results were analyzed in terms of strain paths of the most critical node on the sheet, i.e. the one experiencing the contact with the punch radius and located on the outer surface.

To evaluate the reliability of the FE simulations using Mass Scaling, the Internal Energy (ALLIE) and Kinetic Energy (ALLKE) were compared (Figure 6.20a). Finally, to verify that ALLKE is a small fraction (5-10%) of ALLIE. FE simulation results of one combination of punch diameter (i.e., 30.5 mm) and die entry radius (i.e., 3 mm) in terms of thickness distribution after the Deep Drawing (DD) process (Figure 6.20b) were also compared. Both the comparisons showed that the adopted Mass Scaling (1E-005) allowed to obtain reliable results.

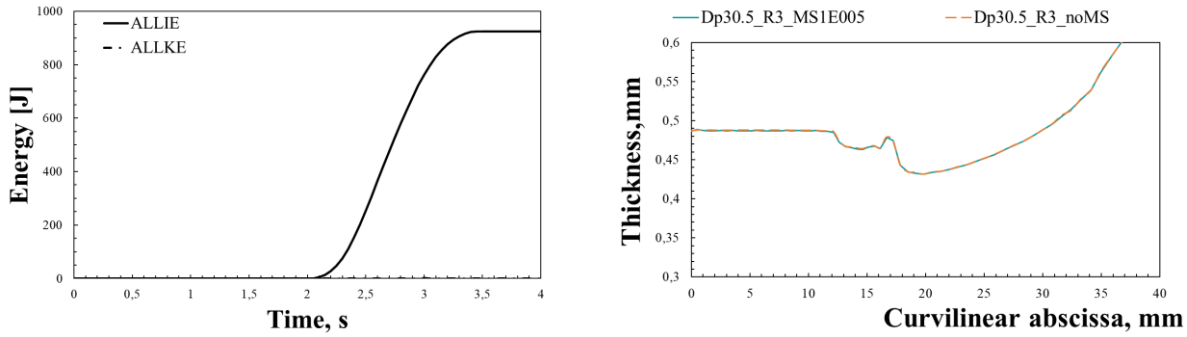

(a) (b)

Figure 6.20 (a) ALLIE and ALLKIE comparison and (b) Thickness distribution after the DD process of Al 5754-H111 sheets using mass scaling (blue solid line) and without using it (orange dashed line)

To design the Punch diameter, D_p and the Die fillet radius, R_{die}, for the hydromechanical deep drawing using MRF, the most critical node (point A in Figure 6.21a), i.e., the one that is located on the external portion of the sheet corresponding to the punch-sheet contact area was evaluated. Figure 6.21b,c,d show the strain path evolution of point A during the DD process (without using MRF) for the different combinations of R_{die} and D_p. In the case of R_{die}=3 (Figure 6.21b), it can be observed that on the one hand, values of D_p equal to 29.5 mm and 30.5 mm supported obtaining safe deep drawn parts with LDR values equal to 2.3 and 2.23 respectively; on the other hand, when a D_p=26.5 mm was used, the strain path of point A not only exceeded the critical strains evidenced by the FLC, but its trend didn't fall into the plane strain region as it expected [112]. The strain paths evolutions of point A in the case of R_{die}=5 mm and 8 mm are similar for each value of D_p, as shown in Figure 6.21c,d. Additionally, where D_p is equal to 29.5 mm and 30.5 mm, safe deep drawn parts were obtained, unlike where the value of D_p is equal to both 26.5 mm; in that case, even if R_{die} was increased from 3 mm (Figure 6.21b) to 5 mm and 8 mm (Figure 6.21c and d respectively) allowing the resulting strain path of point A to be closer to the plane strain condition, it did not result in obtaining a safe deep drawn part. Thus, in the hydromechanical deep drawing (HMDD) tests with MRF, D_p=30.5 mm and R_{die}=3 mm was used.

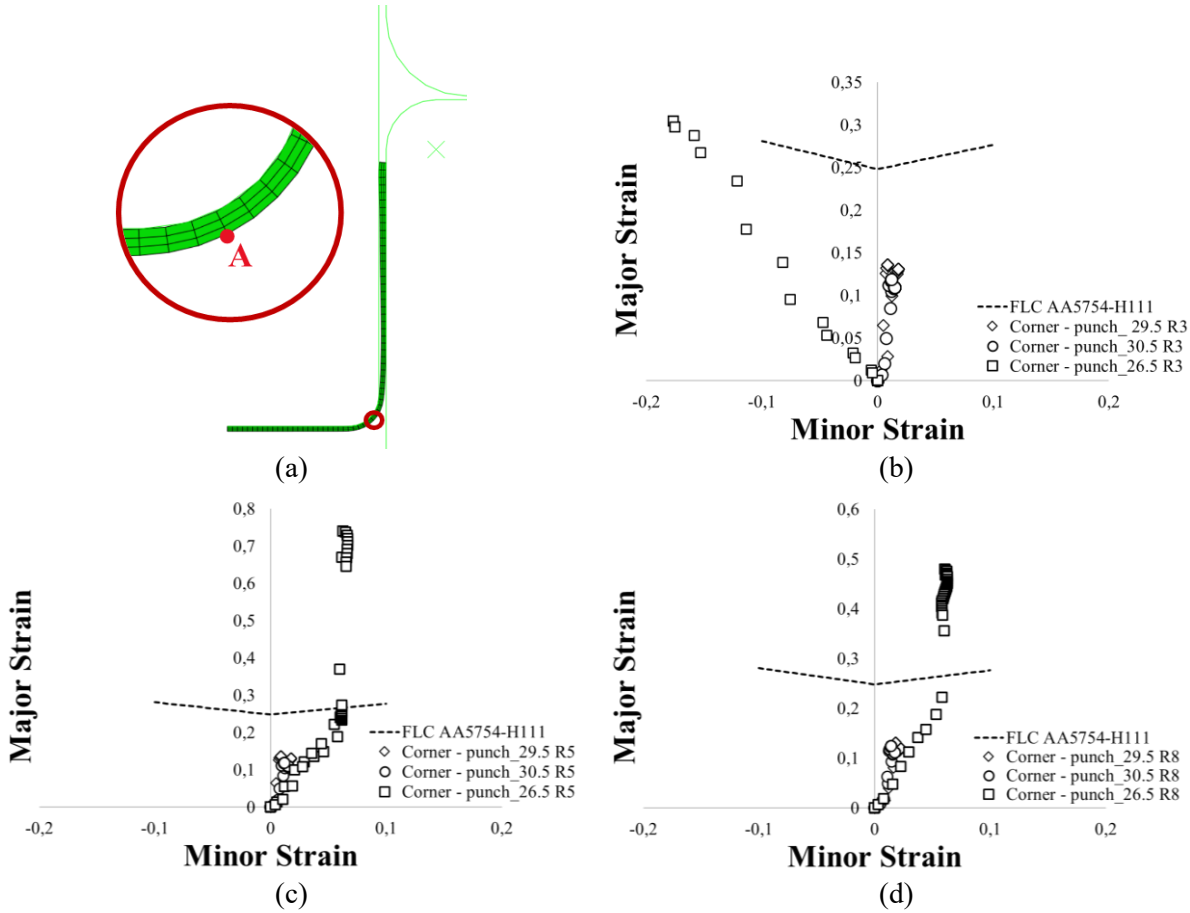

Figure 6.21(a) Node of the deformed sheet selected for the strain path analysis; the node is indicated by a red dot; (b) Strain path evolution of point A for different D_p values and R_{die}=3; (c) Strain path evolution of point A for different D_p values and R_{die}=5;(d) Strain path evolution of point A for different D_p values and R_{die}=8;

As for the hydromechanical deep drawing FE model, the MRF was added in the assembly and modelled as deformable body. It was then meshed with 3200 CAX4R (4-node axisymmetric bilinear quadrilaterals with reduced integration and hourglass control) elements, progressively reducing their average size in the proximity of the contact with the blank, as shown in Figure 6.22a. The rheological behaviour of the MRF obtained from the characterization described in section 3.3 was implemented in the FE model. The strain paths of the node (Point A in Figure 6.22b) located on the external portion of the sheet corresponding to the punch-sheet contact were analysed to evaluate the effect of using MRF during the hydromechanical deep drawing process.

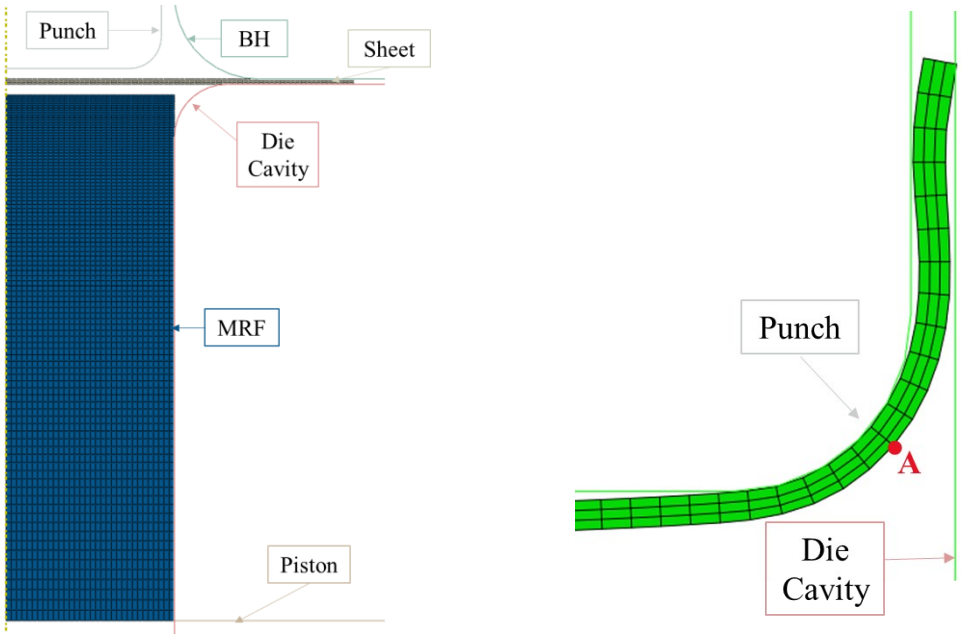

(a) (b)

Figure 6.22 (a) FE model of the deep drawing process using MRF (b) Node (point A) chosen for the strain path analysis

6.2.2 Hydromechanical Deep Drawing using MRF on AZ31B

To assess any effect of using MRF during the hydromechanical deep drawing process, AZ31B-H24 was chosen, being a hard to deform material at room temperature. In literature, it was found that the Limit Drawing Ratio (LDR) at room temperature is approximately 1.3[59].**Figure 6.23** shows the strain map distribution of the equivalent plastic strain (PEEQ) of the AZ31B sheet having a diameter of 38 mm after the DD process (**Figure 6.23**a) and the HMDD process (**Figure 6.23**b) and using a punch having a diameter of 30.5, thus resulting in a β= 1.25.

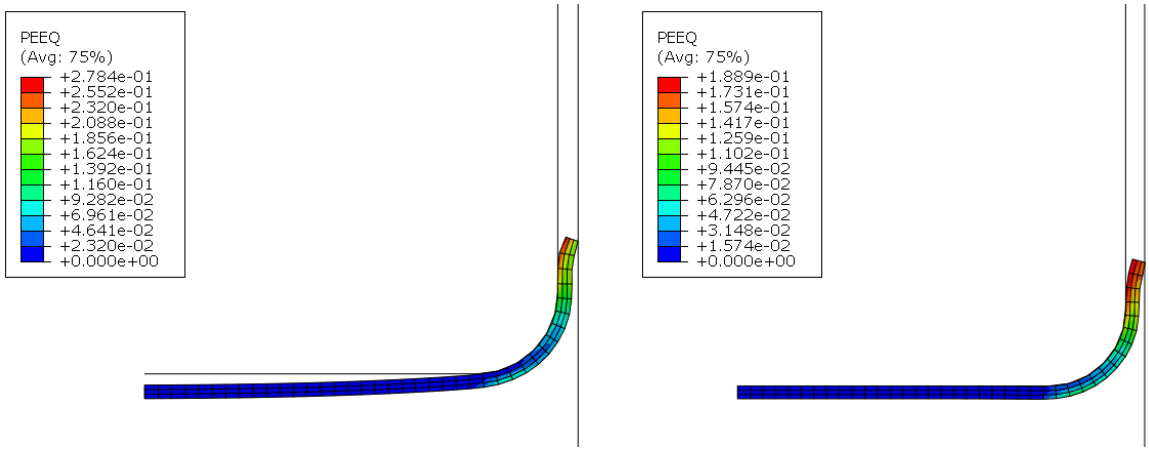

(a) (b)

Figure 6.23 Strain map distribution of the equivalent plastic strain (PEEQ) of the AZ31B sheet (diameter 38 mm) after (a) DD process and (b) HMDD process

From the figures it can be noticed that during the HMDD process the force generated by the pressure under the blank, which is opposite to the blank holder force, had an influence in terms of strain distributions. In fact, in the case of HMDD (**Figure 6.23**b) levels of maximum strains are overall lower compared to the DD process (**Figure 6.23**b). The effect of using MRF in the DD process is more evident in **Figure 6.24**.

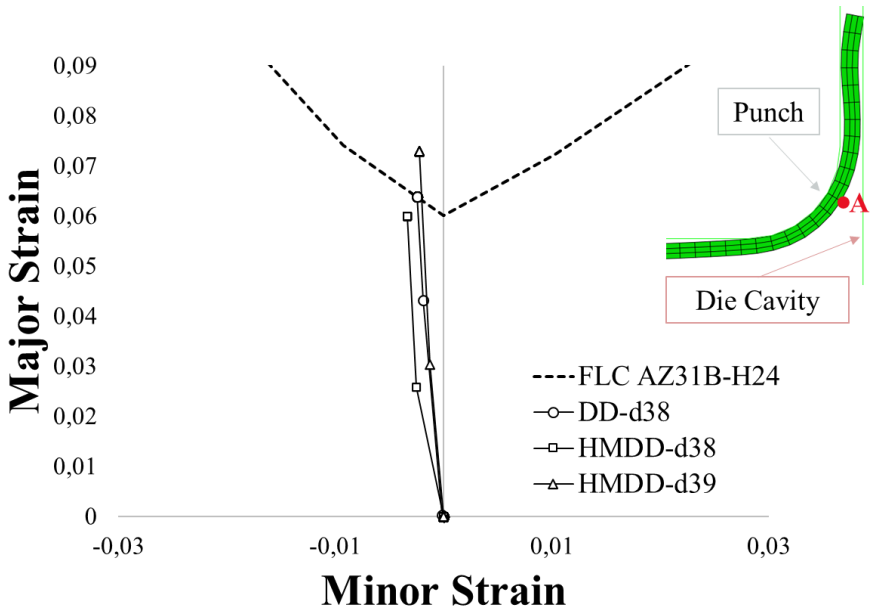

Figure 6.24 Strain paths of the point A compared to the AZ31B-H24 FLC in the case of DD process on a AZ31B sheet having d=38 mm (DD-d38), HMDD process on a AZ31B sheet having d=38 mm (HMDD-38) and HMDD process on a AZ31B sheet having d=39 mm (HMDD-39)

Strain paths of the point A (located on the external portion of the sheet corresponding to the punch-sheet contact area) are shown. It can be noticed that in absence of MRF (Strain path indicated ad "DD-38"), the LDR of AZ31B is less than 1.25, since its maximum equivalent plastic strain is located on the AZ31B FLC. Instead in the case of the hydromechanical deep drawing (Strain path indicated ad "HMDD-38"), the Mg sheet reached a LDR of 1.25, being the equivalent plastic strains located in the safe zone of the FLD. However, even if the pressure given by the MRF led to an improvement in terms of formability, the maximum LDR reachable from the sheet is 1.25. In fact, looking at the strain path obtained with HMDD increasing the sheet diameter to obtain a higher LDR (Strain path indicated ad "HMDD-39" in **Figure 6.24**) its maximum equivalent plastic strain is located above the AZ31B FLC, thus indicating that rupture occurred. The reason of this limited improvement in Mg drawability even if using a fluid pressure is due to the Mg hexagonal close-packed (HCP) crystalline structure, which restricts slips to the basal plane and making the Mg difficult to plastically deform at room temperature.

Conclusions

In this thesis, the feasibility of expanding the manufacturing of lightweight complex-shaped components using alternative processes, such as hydroforming using magnetorheological fluids (MRFs) was evaluated. To this aim, the characterization of both the MRF and the lightweight alloys was studied. As for the lightweight materials investigated, the attention was focused on Al alloys and Mg alloys because they are attractive materials for the transportation and biomedical sector, respectively. The mechanical characterization of the Mg alloy (AZ31B-H24) led to the exploration of two flexible manufacturing processes, namely Single Point Incremental Forming (SPIF) and Superplastic Forming (SPF), to manufacture a resorbable cheekbone prosthesis and they both enabled the successful manufacture of research demonstrator components. Comparing both processes, SPF supported obtaining a better surface quality, however at the same time it required a more complex set-up, having higher temperatures (450°C) and requiring a die to shape the part into.

The aluminum alloy investigated (AA5754) was characterised both in H32 and in H111 temper. In the case of the H32 temper, a new methodology for the determination of the right hand of the Forming Limit Curve (FLC), based on the adoption of local heat treatments aimed at determining different strain paths on the test blank while using the classical circular die for bulge tests was proposed. Numerical results showed that by modifying the size and position of the laser heat treatment on the sheet, it was possible to achieve a change in the strain path of the dome and in turn investigate the deformation of the FLD in the range of positive minor strains. The proposed methodology is promising and it can be extended to the heat treatable alloys that represent a broad range of materials often used for industrial applications.

As for the rheological characterization of the MRF, two different approaches were evaluated. The first, was based on a methodology taken from literature and it consisted on the combination of extrusion tests and FE simulation. The second, is presented in this work for the first time and is based on an inverse analysis approach using data from bulge tests performed on the investigated Al alloy (AA5754-H111) adopting the MRF as forming medium. The approach proposed in literature allowed to study only the MRF behavior, whereas a different set-up was needed to characterize the sheet metal blank. The novelty of the proposed new methodology is that it potentially allows to study the lightweight alloy formability and characterizing the MRF at the same time, using the specifically designed equipment with a solenoid to generate the magnetic field, which was presented in the present thesis. The complexity of such equipment is very low and it is very flexible. In fact, besides the bulge tests for characterising metal sheets,

it can be interfaced with a universal testing machine to conduct DD (deep drawing) and HMDD (hydromechanical deep drawing) tests. The latter allowed to slightly increase magnesium formability. Moreover, since the strain level of the prostheses obtained by SPF and SPIF is comparable to the strain level reached by bulge tests using MRF on Mg sheets, the MRF Hydroforming would be a suitable process to produce such prosthesis. However, to obtain very complex geometries with higher strain levels when considering magnesium sheets, warm conditions are needed, thus processes such as SPIF and SPF are preferable.

Future works will be focused on the investigation of more levels of both magnetic field and pressure rates during bulge tests for the MRF characterization and on more refined constitutive equations to further improve the prediction capabilities of the proposed methodology for the MRF characterization. Moreover, as for the new methodology proposed for determining the right hand of the Forming Limit Curve (FLC), future works will be aimed at evaluating the optimal laser parameters to obtain the desired characteristics on the treated zone and at understanding the correlation between the mechanical properties of the test sample after the laser heat treatment (hardness and microstructure).

List of scientific works

1. G. Palumbo, **A. Cusanno**, M.L. Garcia Romeu , I. Bagudanch, N. Contessi Negrini, T. Villa, S. Farè "*Single Point Incremental Forming and Electrospinning to produce biodegradable magnesium (AZ31) biomedical prostheses coated with porous PCL*", Materials Today: Proceedings 7, **2019**, 394–401, https://doi.org/10.1016/j.matpr.2018.11.101

2. **A. Cusanno**, G. Centeno, M.L. Garcia-Romeu, G. Palumbo, "*On the assessment of formability and failure of Mg sheets formed by SPIF*", Proceedings of the 13th International Conference on Numerical Methods in Industrial Forming Processes (NUMIFORM 2019), 23-27 Giugno **2019**, Portsmouth, New Hampshire, USA;

3. A. Piccininni, **A. Cusanno**, G. Palumbo, A. Forcellese, E. Mancini, M. Simoncini, "*Mechanical characterization of an age-hardenable aluminum alloy at high strain rates for the simulation of the Electro Magnetic Forming*", Proceedings del convegno AITEM 2019 (Associazione Italiana Tecnologie Manifatturiere), 9-11 Settembre **2019**, Padova, Italia

4. **A. Cusanno**, N. Contessi Negrini, T. Villa, S. Farè, M.L. Garcia-Romeu and G. Palumbo,"*Post Forming Analysis and In Vitro Biological Characterization of AZ31B Processed by Incremental Forming and Coated With Electrospun Polycaprolactone.*" ASME. J. Manuf. Sci. Eng. January **2021**; 143(1): 011012, https://doi.org/10.1115/1.4048741

5. **A. Cusanno,** S. Moturu, D. Carty, G. Palumbo, "*Influence of the Laser Heat Treatment on the AA5754-H32 strain path during hydraulic bulge tests*", ESAFORM 2021 [Online], Online since 05 April 2021, connection on 03 June **2021**. URL : https://popups.uliege.be/esaform21/index.php?id=1536

6. P. Guglielmi, **A. Cusanno**, I. Bagudanch, G. Centeno, I. Ferrer, M.L. Garcia-Romeu, G. Palumbo, "*Experimental and numerical analysis of innovative processes for producing a resorbable cheekbone prosthesis*", J. Manuf. Process., **2021**, 70:1-14, https://doi.org/10.1016/j.jmapro.2021.07.060

7. A.C. Parau, C.M. Cotru, P. Guglielmi, **A. Cusanno**, G. Palumbo, M. Dinu, et al. "*Deposition temperature effect on sputtered hydroxyapatite coatings prepared on AZ31B alloy substrate*", Ceram Int, **2021**, https://doi.org/10.1016/j.ceramint.2021.12.258

8. P. Guglielmi, **A. Cusanno**, D. Sorgente, G. Palumbo, "*Modification of the thickness distribution through the laser heat pre-treatment of Mg superplastically formed sheets*", Proceedings del convegno AITEM 2021 (Associazione Italiana Tecnologie Manifatturiere), 17-19 gennaio **2022**, Online

9. G. Palumbo, G. Ambrogio, A. Crovace, A. Piccininni, **A. Cusanno**, P. Guglielmi, L. De Napoli, and G. Serratore, "*A Structured Approach for the Design and Manufacturing of Titanium Cranial Prostheses via Sheet Metal Forming*" Metals 12, **2022**, no. 2: 293, https://doi.org/10.3390/met12020293

10. **A. Cusanno**, A. Piccininni, P. Guglielmi, G. Palumbo, "*Evaluation of the rheological behaviour of Magnetorheological Fluids combining bulge tests and inverse analysis*", accepted for publication in the Proceedings of the ESAFORM 2022 International Conference (Braga, 27th -30th April 2022).

References

[1] M.R. Jolly, J.W. Bender, J.D. Carlson, Properties and Applications of Commercial Magnetorheological Fluids, Journal of Intelligent Material Systems and Structures. 10 (1999) 5–13. https://doi.org/10.1177/1045389x9901000102.

[2] D. Wang, B. Zi, Y. Zeng, Y. Hou, Q. Meng, Temperature-dependent material properties of the components of magnetorheological fluids, Journal of Materials Science. 49 (2014) 8459–8470. https://doi.org/10.1007/s10853-014-8556-x.

[3] J.S. Kumar, Synthesis of Magnetorheological fluid Compositions for Valve Mode Operation, 2020. www.sciencedirect.comwww.materialstoday.com/proceedings2214-7853.

[4] J. Roupec, P. Berka, I. Mazůrek, Z. Strecker, M. Kubík, O. Macháček, M.T. Andani, A novel method for measurement of MR fluid sedimentation and its experimental verification, Smart Materials and Structures. 26 (2017). https://doi.org/10.1088/1361-665X/aa83f2.

[5] M. Merklein, S. Rösel, Characterization of a magnetorheological fluid with respect to its suitability for hydroforming, International Journal of Material Forming. 3 (2010) 283–286. https://doi.org/10.1007/s12289-010-0762-8.

[6] M. Minotti, R. Pucci, P. Salvini, CARATTERIZZAZIONE DI FLUIDI MAGNETOREOLOGICI MEDIANTE GIOGO MAGNETICO, n.d.

[7] J. Yu, X. Dong, X. Su, S. Qi, Development and characterization of a novel rotary magnetorheological fluid damper with variable damping and stiffness, Mechanical Systems and Signal Processing. 165 (2022). https://doi.org/10.1016/j.ymssp.2021.108320.

[8] M.R. Jolly, J.W. Bender, J.D. Carlson, Properties and Applications of Commercial Magnetorheological Fluids, Journal of Intelligent Material Systems and Structures. 10 (1999) 5–13. https://doi.org/10.1177/1045389X9901000102.

[9] X. Zhu, X. Jing, L. Cheng, Magnetorheological fluid dampers: A review on structure design and analysis, Journal of Intelligent Material Systems and Structures. 23 (2012) 839–873. https://doi.org/10.1177/1045389X12436735.

[10] A.G. Olabi, A. Grunwald, Design and application of magneto-rheological fluid, Materials and Design. 28 (2007) 2658–2664. https://doi.org/10.1016/j.matdes.2006.10.009.

[11] S.A. Mazlan, N.B. Ekreem, A.G. Olabi, The performance of magnetorheological fluid in squeeze mode, Smart Materials and Structures. 16 (2007) 1678–1682. https://doi.org/10.1088/0964-1726/16/5/021.

[12] S. Zareie, A. Zabihollah, The Recent Advances in Magnetorheological Fluids-Based Applications, n.d. www.intechopen.com.

[13] A. Spaggiari, E. Dragoni, Effect of pressure on the flow properties of magnetorheological fluids, Journal of Fluids Engineering, Transactions of the ASME. 134 (2012). https://doi.org/10.1115/1.4007257.

[14] E.M. Attia, N.M. Elsodany, H.A. El-Gamal, M.A. Elgohary, Theoretical and experimental study of magneto-rheological fluid disc brake, Alexandria Engineering Journal. 56 (2017) 189–200. https://doi.org/10.1016/J.AEJ.2016.11.017.

[15] A. Gaikar, Study of Magnetorheological Fluid and its Applications, International Journal for Research in Applied Science and Engineering Technology. 7 (2019) 271–275. https://doi.org/10.22214/IJRASET.2019.1045.

[16] J. Wang, G. Meng, Magnetorheological fluid devices: Principles, characteristics and applications in mechanical engineering:, Http://Dx.Doi.Org/10.1243/1464420011545012. 215 (2005) 165–174. https://doi.org/10.1243/1464420011545012.

[17] Z.Q. Chen, X.Y. Wang, J.M. Ko, Y.Q. Ni, B.F. Spencer, Jr., G. Yang, MR damping system on Dongting Lake cable-stayed bridge, Https://Doi.Org/10.1117/12.498072. 5057 (2003) 229–235. https://doi.org/10.1117/12.498072.

[18] E.T. Thorarinsson, F. Jonsdottir, H. Palsson, Design of a Magnetorheological Prosthetic Knee, 2006.

[19] F. Gao, Y.N. Liu, W.H. Liao, Optimal design of a magnetorheological damper used in smart prosthetic knees, Smart Materials and Structures. 26 (2017) 035034. https://doi.org/10.1088/1361-665X/AA5494.

[20] J.A. Menapace, Developing Magnetorheological Finishing (MRF) Technology for the Manufacture of Large-Aperture Optics in Megajoule Class Laser Systems, Laser-Induced Damage in Optical Materials: 2010. 7842 (2010) 78421W. https://doi.org/10.1117/12.855603.

[21] Z. Alam, S. Jha, Modeling of surface roughness in ball end magnetorheological finishing (BEMRF) process, Wear. 374–375 (2017) 54–62. https://doi.org/10.1016/J.WEAR.2016.11.039.

[22] S.D. Puma-Araujo, D. Olvera-Trejo, O. Martínez-Romero, G. Urbikain, A. Elías-Zúñiga, L.N.L. de Lacalle, Semi-active magnetorheological damper device for chatter mitigation during milling of thin-floor components, Applied Sciences (Switzerland). 10 (2020). https://doi.org/10.3390/APP10155313.

[23] P. yi Wang, Z. jin Wang, Determination of the flow stress of a magnetorheological fluid under three-dimensional stress states by using a combination of extrusion test and FEM simulation, Journal of Magnetism and Magnetic Materials. 419 (2016) 255–266. https://doi.org/10.1016/j.jmmm.2016.06.024.

[24] P. yi Wang, N. Xiang, Z. jin Wang, Z. xin Li, The rapid response of forming medium's properties to variable loading types of magnetic field and consequent field-dependent sheet formability, Journal of Manufacturing Processes. 31 (2018) 468–479. https://doi.org/10.1016/J.JMAPRO.2017.12.006.

[25] P. yi Wang, Z. jin Wang, N. Xiang, Z. xin Li, Investigation on changing loading path in sheet metal forming by applying a property-adjustable flexible-die, Journal of Manufacturing Processes. 53 (2020) 364–375. https://doi.org/10.1016/J.JMAPRO.2020.03.033.

[26] Z.J. Wang, P.Y. Wang, H. Song, Research on sheet-metal flexible-die forming using a magnetorheological fluid, Journal of Materials Processing Technology. 214 (2014) 2200–2211. https://doi.org/10.1016/j.jmatprotec.2014.04.016.

[27] A. Spaggiari, E. Dragoni, SISTEMA DI CARATTERIZZAZIONE PER FLUIDI MAGNETOREOLOGICI: EFFETTO DELLA PRESSIONE IN MODALITA' SCORRIMENTO, n.d.

[28] H. Liu, Q. Luo, J. Wu, T. Li, Y.Q. Wang, Performance analysis of MRF-based flexible supporting of thin-walled part, ACM International Conference Proceeding Series. Part F1376 (2018) 132–136. https://doi.org/10.1145/3191477.3191505.

[29] F. Czerwinski, Current Trends in Automotive Lightweighting Strategies and Materials, Materials 2021, Vol. 14, Page 6631. 14 (2021) 6631. https://doi.org/10.3390/MA14216631.

[30] D. Kumar, R.K. Phanden, L. Thakur, A review on environment friendly and lightweight Magnesium-Based metal matrix composites and alloys, Materials Today: Proceedings. 38 (2021) 359–364. https://doi.org/10.1016/j.matpr.2020.07.424.

[31] C. Han, Research on the Development and Application of Lightweight Automotive Materials, Journal of Physics: Conference Series. 1676 (2020). https://doi.org/10.1088/1742-6596/1676/1/012085.

[32] S. Rosenthal, F. Maaß, M. Kamaliev, M. Hahn, S. Gies, A.E. Tekkaya, Lightweight in Automotive Components by Forming Technology, Automotive Innovation. 3 (2020) 195–209. https://doi.org/10.1007/s42154-020-00103-3.

[33] M. Goede, M. Stehlin, L. Rafflenbeul, G. Kopp, E. Beeh, Super Light Car-lightweight construction thanks to a multi-material design and function integration, European Transport Research Review. 1 (2009) 5–10. https://doi.org/10.1007/s12544-008-0001-2.

[34] M. Marino, R. Sabatini, Advanced Lightweight Aircraft Design Configurations for Green Operations, (2014). https://doi.org/10.13140/2.1.4231.8405.

[35] J. Galán, L. Samek, P. Verleysen, K. Verbeken, Y. Houbaert, Advanced high strength steels for automotive industry, Revista de Metalurgia. 48 (2012) 118–131. https://doi.org/10.3989/REVMETALM.1158.

[36] F. Czerwinski, Current trends in automotive lightweighting strategies and materials, Materials. 14 (2021). https://doi.org/10.3390/ma14216631.

[37] T. Furuta, Automobile applications of titanium, Titanium for Consumer Applications: Real-World Use of Titanium. (2019) 77–90. https://doi.org/10.1016/B978-0-12-815820-3.00006-X.

[38] L. Zhu, N. Li, P.R.N. Childs, Light-weighting in aerospace component and system design, Propulsion and Power Research. 7 (2018) 103–119. https://doi.org/10.1016/j.jppr.2018.04.001.

[39] T. Sakurai, The Latest Trends in Aluminum Alloy Sheets for Automotive Body Panels, Undefined. (2008).

[40] K. Zheng, D.J. Politis, L. Wang, J. Lin, A review on forming techniques for manufacturing lightweight complex—shaped aluminium panel components, International Journal of Lightweight Materials and Manufacture. (2018). https://doi.org/10.1016/j.ijlmm.2018.03.006.

[41] K.K. Alaneme, A.V. Fajemisin, N.B. Maledi, Development of aluminium-based composites reinforced with steel and graphite particles: Structural, mechanical and wear characterization, Journal of Materials Research and Technology. 8 (2019) 670–682. https://doi.org/10.1016/j.jmrt.2018.04.019.

[42] M. Tisza, I. Czinege, Comparative study of the application of steels and aluminium in lightweight production of automotive parts, International Journal of Lightweight Materials and Manufacture. 1 (2018) 229–238. https://doi.org/10.1016/J.IJLMM.2018.09.001.

[43] C. Ungureanu, I.S. Jawahir, Life-cycle Cost Analysis: Aluminum versus Steel in Passenger Cars, Undefined. (2007).

[44] European Aluminium, VISION 2050 EUROPEAN ALUMINIUM'S CONTRIBUTION TO THE EU'S MID-CENTURY LOW-CARBON ROADMAP A vision for strategic, low carbon and competitive aluminium, 2019. https://european-aluminium.eu/media/2545/sample_vision-2050-low-carbon-strategy_20190401.pdf (accessed January 4, 2022).

[45] G. Demir, A.U. Malcıoğlu, S. Sağdiç, A. Ulus, S. Aslanlar, E. İlhan, Optimization of Thermo-Mechanical Processes of Continuous Casting Products Using High Magnesium Aluminum Alloys in Automotive Industry Applications, in: Minerals, Metals and Materials Series, Springer Science and Business Media Deutschland GmbH, 2020: pp. 386–399. https://doi.org/10.1007/978-3-030-36408-3_55.

[46] S. Toros, F. Ozturk, I. Kacar, Review of warm forming of aluminum-magnesium alloys, Journal of Materials Processing Technology. 207 (2008) 1–12. https://doi.org/10.1016/J.JMATPROTEC.2008.03.057.

[47] G. Palumbo, A. Piccininni, P. Guglielmi, G. di Michele, Warm HydroForming of the heat treatable aluminium alloy AC170PX, Journal of Manufacturing Processes. 20 (2015) 24–32. https://doi.org/10.1016/j.jmapro.2015.09.012.

[48] Chen et al., Metallic implant biomaterials, Materials Science and Engineering R: Reports. 87 (2015) 1–57. https://doi.org/10.1016/j.mser.2014.10.001.

[49] Navarro et al., Biomaterials in orthopaedics, Journal of the Royal Society. 5 (2008) 1137–1158. https://doi.org/10.1007/978-3-319-14845-8_7.

[50] Shadanbaz et al., Calcium phosphate coatings on magnesium alloys for biomedical applications: A review, Acta Biomaterialia. 8 (2012) 20–30. https://doi.org/10.1016/j.actbio.2011.10.016.

[51] Witte et al., Characterization of Degradable Magnesium Alloys as Orthopaedic Implant Material by, (2001).

[52] M. Gupta, S. Nai Mui Ling, Magnesium, Magnesium Alloys an Magnesium Composites, 2010. https://doi.org/10.1002/9780470905098.ch1.

[53] O. Duygulu et al., Investigation on the Potential of Magnesium Alloy AZ31 as a Bone Implant, Materials Science Forum. 546–549 (2007) 421–424. https://doi.org/10.4028/www.scientific.net/MSF.546-549.421.

[54] Farraro et al., Revolutionizing orthopaedic biomaterials: The potential of biodegradable and bioresorbable magnesium-based materials for functional tissue engineering, Journal of Biomechanics. 47 (2014) 1979–1986. https://doi.org/10.1016/j.jbiomech.2013.12.003.

[55] G. Ambrogio, L. Filice, G.L. Manco, Warm incremental forming of magnesium alloy AZ31, CIRP Annals - Manufacturing Technology. 57 (2008) 257–260. https://doi.org/10.1016/j.cirp.2008.03.066.

[56] Staiger et al., Magnesium and its alloys as orthopedic biomaterials: A review, Biomaterials. 27 (2006) 1728–1734. https://doi.org/10.1016/j.biomaterials.2005.10.003.

[57] P.A. Tebbe, G.T. Kridli, Warm forming of aluminium alloys: An overview and future directions, International Journal of Materials and Product Technology. 21 (2004) 24–40. https://doi.org/10.1504/IJMPT.2004.004737.

[58] D. Li, A.K. Ghosh, Biaxial warm forming behavior of aluminum sheet alloys, Journal of Materials Processing Technology. 145 (2004) 281–293. https://doi.org/10.1016/j.jmatprotec.2003.07.003.

[59] K.F. Zhang, D.L. Yin, D.Z. Wu, Formability of AZ31 magnesium alloy sheets at warm working conditions, International Journal of Machine Tools and Manufacture. 46 (2006) 1276–1280. https://doi.org/10.1016/J.IJMACHTOOLS.2006.01.014.

[60] A. Piccininni, G. Palumbo, A. lo Franco, D. Sorgente, L. Tricarico, G. Russello, Multi objective genetic algorithm to optimize the local heat treatment of a hardenable aluminum alloy, AIP Conference Proceedings. 1960 (2018). https://doi.org/10.1063/1.5034965.

[61] F. Reuther, T. Lieber, J. Heidrich, V. Kräusel, Numerical investigations on thermal forming limit testing with local inductive heating for hot forming of aa7075, Materials. 14 (2021). https://doi.org/10.3390/ma14081882.

[62] T. Nishiwaki, R. Sako, H. Tsutamori, Hydro-Mechanical Deep Drawing of Locally Solution-Treated Aluminum Alloy Sheets, in: G. Daehn, J. Cao, B. Kinsey, E. Tekkaya, A. Vivek, Y. Yoshida (Eds.), Forming the Future, Springer International Publishing, Cham, 2021: pp. 2729–2739.

[63] N. Rigas, M. Merklein, Numerical and experimental investigations for distortion-reduced laser heat treatment of aluminum, Production Engineering. 15 (2021) 479–488. https://doi.org/10.1007/s11740-021-01029-3.

[64] N. Bianco, O. Manca, S. Nardini, S. Tamburino, Transient heat conduction in solids irradiated by a moving heat source, in: Defect and Diffusion Forum, Trans Tech Publications Ltd, 2009: pp. 358–363. https://doi.org/10.4028/www.scientific.net/DDF.283-286.358.

[65] M. Geiger, M. Merklein, Aluminum tailored heat treated blanks, (2009) 401–410. https://doi.org/10.1007/s11740-009-0179-8.

[66] S. Bruschi, T. Altan, D. Banabic, P.F. Bariani, A. Brosius, J. Cao, A. Ghiotti, M. Khraisheh, M. Merklein, A.E. Tekkaya, Testing and modelling of material behaviour and formability in sheet metal forming, CIRP Annals - Manufacturing Technology. 63 (2014) 727–749. https://doi.org/10.1016/j.cirp.2014.05.005.

[67] M. Lechner, M. Johannes, A. Kuppert, M. Merklein, Influence of pre-straining and heat treatment on the yield surface of precipitation hardenable aluminum alloys, in: Physics Procedia, Elsevier B.V., 2014: pp. 1400–1409. https://doi.org/10.1016/j.phpro.2014.08.070.

[68] M. Merklein, H. Nguyen, Advanced laser heat treatment with respect for the application for Tailored Heat Treated Blanks, in: Physics Procedia, Elsevier B.V., 2010: pp. 233–242. https://doi.org/10.1016/j.phpro.2010.08.049.

[69] A. Piccininni, G. Palumbo, Design and optimization of the local laser treatment to improve the formability of age hardenable aluminium alloys, Materials. 13 (2020). https://doi.org/10.3390/ma13071576.

[70] P. Guglielmi, D. Sorgente, G. Palumbo, Numerical/experimental investigation of bulge tests on a localized laser heat-treated magnesium alloy AZ31 sheet, ESAFORM 2021. (2021). https://doi.org/10.25518/esaform21.1555.

[71] K.A. Padmanabhan, S.B. Prabu, R.R. Mulyukov, A. Nazarov, R.M. Imayev, S.G. Chowdhury, Superplastic Forming, Analyses and Industrial Applications, (2018) 359–428. https://doi.org/10.1007/978-3-642-31957-0_9.

[72] D. Sorgente, G. Palumbo, L.D. Scintilla, R. Brivio, G. Carozzi, L. Tricarico, Superplastic forming of a complex shape automotive component with optimized heated tools, Materials Science Forum. 838–839 (2016) 494–499. https://doi.org/10.4028/www.scientific.net/MSF.838-839.494.

[73] D. Sorgente, G. Palumbo, A. Piccininni, P. Guglielmi, S.A. Aksenov, Investigation on the thickness distribution of highly customized titanium biomedical implants manufactured by superplastic forming, CIRP Journal of Manufacturing Science and Technology. 20 (2018) 29–35. https://doi.org/10.1016/j.cirpj.2017.09.004.

[74] G. Bernhart, P. Lours, T. Cutard, V. Velay, F. Nazaret, Processes and equipment for superplastic forming of metals, Superplastic Forming of Advanced Metallic Materials. (2011) 49–71. https://doi.org/10.1533/9780857092779.1.49.

[75] Y. Kumar, S. Kumar, Incremental Sheet Forming (ISF), Advances in Material Forming and Joining. (2015) 29–47. https://doi.org/10.1007/978-81-322-2355-9.

[76] G. Palumbo, A. Cusanno, M.L. Garcia Romeu, I. Bagudanch, N. Contessi Negrini, T. Villa, S. Farè, Single Point Incremental Forming and Electrospinning to produce biodegradable magnesium (AZ31) biomedical prostheses coated with porous PCL, Materials Today: Proceedings. 7 (2019) 394–401. https://doi.org/10.1016/j.matpr.2018.11.101.

[77] Echrif et al., Research and Progress in Incremental Sheet Forming Processes, Materials and Manufacturing Processes. 26 (2011) 1404–1414. https://doi.org/10.1080/10426914.2010.544817.

[78] M. Tisza, General overview of sheet incremental forming, Manufacturing Engineering. 55 (2012) 113–120.

[79] G. Palumbo, V. Piglionico, A. Piccininni, P. Guglielmi, L. Tricarico, Evaluation of the optimal working conditions for the warm sheet HydroForming taking into account the yielding condition, Materials and Design. 91 (2016) 411–423. https://doi.org/10.1016/j.matdes.2015.11.113.

[80] G. Palumbo, L. Tricarico, S.H. Zhang, L.X. Zhou, J. Danckert, K.B. Nielsen, Evaluation of the effects of a movable tool in the hydroforming process, International Journal of Materials and Product Technology. 38 (2010) 386–398. https://doi.org/10.1504/IJMPT.2010.033818.

[81] G. Palumbo, Hydroforming a small scale aluminum automotive component using a layered die, Materials and Design. 44 (2013) 365–373. https://doi.org/10.1016/j.matdes.2012.08.013.

[82] K. Zheng, D.J. Politis, L. Wang, J. Lin, A review on forming techniques for manufacturing lightweight complex—shaped aluminium panel components, International Journal of Lightweight Materials and Manufacture. 1 (2018) 55–80. https://doi.org/10.1016/J.IJLMM.2018.03.006.

[83] S.H. Zhang, J. Danckert, Development of hydro-mechanical deep drawing, 1998.

[84] B.S. Kang, B.M. Son, J. Kim, A comparative study of stamping and hydroforming processes for an automobile fuel tank using FEM, International Journal of Machine Tools and Manufacture. 44 (2004) 87–94. https://doi.org/10.1016/J.IJMACHTOOLS.2003.08.009.

[85] G. Cai, C. Wu, D. Zhang, Investigation on the effect of type of cooling on the properties of aluminum alloy during warm/hot hydromechanical deep drawing, Symmetry. 10 (2018). https://doi.org/10.3390/SYM10090362.

[86] Z.J. Wang, J.G. Liu, X.Y. Wang, Z.Y. Hu, B. Guo, Viscous pressure forming (VPF): state-of-the-art and future trends, Journal of Materials Processing Technology. 151 (2004) 80–87. https://doi.org/10.1016/J.JMATPROTEC.2004.04.010.

[87] L.D. Hefti, Commercial airplane applications of superplastically formed AA5083 aluminum sheet, in: Journal of Materials Engineering and Performance, 2007: pp. 136–141. https://doi.org/10.1007/s11665-007-9023-5.

[88] L. Yi, X. Li, Y. Li, G. Yu, Z. Tang, Z. Gu, Investigation of the two-stage SPF process of aluminum alloy door frames, Journal of Materials Research and Technology. 15 (2021) 2873–2882. https://doi.org/10.1016/j.jmrt.2021.09.110.

[89] L. Iorio, E. Maspero, M. Strano, Hydroforming of locally heat treated tubes, Journal of Manufacturing Processes. 16 (2014) 157–165. https://doi.org/10.1016/J.JMAPRO.2014.01.002.

[90] G. Palumbo, P. Guglielmi, A. Piccininni, I. Ferrer, M.L. Garcia-Romeu, Manufacturing of a hemispherical component combining incremental forming and superplastic forming, CIRP Journal of Manufacturing Science and Technology. 31 (2020) 178–188. https://doi.org/10.1016/J.CIRPJ.2020.04.006.

[91] R. Araújo, P. Teixeira, L. Montanari, A. Reis, M.B. Silva, P.A. Martins, Single point incremental forming of a facial implant, Prosthetics and Orthotics International. 38 (2014) 369–378. https://doi.org/10.1177/0309364613502071.

[92] I. Bagudanch, G. Centeno, C. Vallellano, M.L. Garcia-romeu, Revisiting formability and failure of polymeric sheets deformed by Single Point Incremental Forming, Polymer Degradation and Stability. 144 (2017) 366–377. https://doi.org/10.1016/j.polymdegradstab.2017.08.021.

[93] ASTM E112-13, Standard Test Methods for Determining Average Grain Size, ASTM International,West Conshohocken, PAW,2013,ww.astm.org, in: n.d.

[94] H. Campos, A.D. Santos, B. Martins, K. Ito, N. Mori, F. Barlat, HYDRAULIC BULGE TEST FOR STRESS-STRAIN CURVE DETERMINATION AND DAMAGE CALIBRATION FOR ITO-GOYA MODEL, n.d. www.inegi.up.pt.

[95] M. Mattiasson, Sigvant, M and Larsson, Methods for forming limit prediction in ductile metal sheets, IDDRG Proceedings. 6 (2006) 1–9.

[96] A.L.F. A. Piccininni, G. Palumbo, Numerical Simulation of the Stamping Process of an AA5754 Railway Vehicle Component using a Locally Annealed Blank, Conference Proceeding NUMIFORM 2019. (n.d.).

[97] SIMULIA, Abaqus/CAE 6.14 User's Manual, Dassault Systémes Inc. Provid. RI, USA. (2014) 1–1146.

[98] M. Basharat, M. Ding, H. Cai, Y. Li, J. Fang, Design and Analysis of Multilayer Solenoid Coil for Faraday Modulator, n.d.

[99] P. Guglielmi, A. Cusanno, I. Bagudanch, G. Centeno, I. Ferrer, M.L. Garcia-Romeu, G. Palumbo, Experimental and numerical analysis of innovative processes for producing a resorbable cheekbone prosthesis, Journal of Manufacturing Processes. 70 (2021) 1–14. https://doi.org/10.1016/j.jmapro.2021.07.060.

[100] A. Piccininni, G. di Michele, G. Palumbo, D. Sorgente, L. Tricarico, Improving the hydromechanical deep-drawing process using aluminum tailored heat treated blanks,

Acta Metallurgica Sinica (English Letters). 28 (2015) 1482–1489. https://doi.org/10.1007/s40195-015-0347-0.

[101] G. Centeno, A.J. Martínez-Donaire, I. Bagudanch, D. Morales-Palma, M.L. Garcia-Romeu, C. Vallellano, Revisiting formability and failure of AISI304 sheets in SPIF: Experimental approach and numerical validation, Metals. 7 (2017). https://doi.org/10.3390/met7120531.

[102] J. Park, J. Kim, N. Park, Y. Kim, Study of Forming Limit for Rotational Incremental Sheet Forming of Magnesium Alloy Sheet, Metallurgical and Materials Transactions A. 41 (2010) 97–105. https://doi.org/10.1007/s11661-009-0043-7.

[103] G. Centeno, I. Bagudanch, A.J. Martínez-Donaire, M.L. García-Romeu, C. Vallellano, Critical analysis of necking and fracture limit strains and forming forces in single-point incremental forming, Materials and Design. 63 (2014) 20–29. https://doi.org/10.1016/j.matdes.2014.05.066.

[104] G. Palumbo, M. Brandizzi, Experimental investigations on the single point incremental forming of a titanium alloy component combining static heating with high tool rotation speed, Materials and Design. 40 (2012) 43–51. https://doi.org/10.1016/j.matdes.2012.03.031.

[105] I. Bagudanch, M. Vives-Mestres, M. Sabater, M.L. Garcia-Romeu, Polymer incremental sheet forming process: Temperature analysis using response surface methodology, Materials and Manufacturing Processes. 32 (2017) 44–53. https://doi.org/10.1080/10426914.2016.1176191.

[106] X. Liu, J.J. Jonas, L.X. Li, B.W. Zhu, Flow softening, twinning and dynamic recrystallization in AZ31 magnesium, Materials Science and Engineering A. 583 (2013) 242–253. https://doi.org/10.1016/j.msea.2013.06.074.

[107] S.M. Fatemi-Varzaneh, A. Zarei-Hanzaki, H. Beladi, Dynamic recrystallization in AZ31 magnesium alloy, Materials Science and Engineering A. 456 (2007) 52–57. https://doi.org/10.1016/j.msea.2006.11.095.

[108] T. Al-Samman, G. Gottstein, Dynamic recrystallization during high temperature deformation of magnesium, Materials Science and Engineering A. 490 (2008) 411–420. https://doi.org/10.1016/j.msea.2008.02.004.

[109] G. Ambrogio, G. Palumbo, E. Sgambitterra, P. Guglielmi, A. Piccininni, L. de Napoli, T. Villa, G. Fragomeni, Experimental investigation of the mechanical performances of titanium cranial prostheses manufactured by super plastic forming and single-point incremental forming, The International Journal of Advanced Manufacturing Technology 2018 98:5. 98 (2018) 1489–1503. https://doi.org/10.1007/S00170-018-2338-6.

[110] G. Gutscher, H.C. Wu, G. Ngaile, T. Altan, Determination of flow stress for sheet metal forming using the viscous pressure bulge (VPB) test, Journal of Materials Processing Technology. 146 (2004) 1–7. https://doi.org/10.1016/S0924-0136(03)00838-0.

[111] D.W.A. Rees, Rim and pole failures from elliptical bulging of oriented orthotropic sheet metal, Journal of Strain Analysis for Engineering Design. 35 (2000) 109–123. https://doi.org/10.1243/0309324001514062.

[112] B.A. Behrens, C. Bonk, N. Grbic, M. Vucetic, Numerical analysis of a deep drawing process with additional force transmission for an extension of the process limits, in: IOP Conference Series: Materials Science and Engineering, Institute of Physics Publishing, 2017. https://doi.org/10.1088/1757-899X/179/1/012006.

La borsa di dottorato è stata cofinanziata con risorse del
Programma Operativo Nazionale Ricerca e Innovazione 2014-2020 (CCI 2014IT16M2OP005),
Fondo Sociale Europeo, Azione I.1 “Dottorati Innovativi con caratterizzazione Industriale”